Electron Identification and Measurement of the Inclusive Semileptonic Branching Fraction of B Mesons at the *BABAR* Experiment

D I S S E R T A T I O N

zur Erlangung des akademischen Grades

Doctor rerum naturalium
(Dr. rer. nat.)

vorgelegt

der Fakultät Mathematik und Naturwissenschaften
der Technischen Universität Dresden

von

Diplom-Physiker Thorsten Brandt
geboren am 24. August 1970 in Minden

Gutachter: Prof. Dr. K. R. Schubert

Prof. Dr. B. Spaan

Dr. V. Lüth

Eingereicht am : 27.11.2001

Abstract

An algorithm for identification of electrons with the *BABAR* detector is developed. Based on pure samples of electrons and hadrons obtained from data, we determine the electron identification efficiency to be above 90% for momenta above 0.5 GeV/c in the laboratory frame, while the pion fake rate lies between 0.05% and 0.1%. Based on this algorithm, a measurement of the inclusive lepton momentum spectrum in B meson decays is performed. We analyze 4.13 fb^{-1} and 0.97 fb^{-1} of data recorded at and slightly below the $\Upsilon(4S)$ resonance with the *BABAR* detector at the PEP-II asymmetric B Factory. $B\overline{B}$ events are tagged by a high momentum electron. Using charge and angular correlations, leptons from a second semileptonic B decay are separated from secondary charm semileptonic decays. The inclusive branching ratio is measured to be $(10.85 \pm 0.22_{(stat)} \pm 0.34_{(sys)})\%$. Combined with the B lifetime we determine $|V_{cb}| = 0.0406 \pm 0.0009_{exp} \pm 0.0019_{theory}$.

Ein Algorithmus zur Identifizierung von Elektronen mit dem *BABAR* Detektor wird entwickelt. Basierend auf Spuren, deren Teilchenidentität aus rein kinematischen Überlegungen gefolgert werden kann, wird für Impulse zwichen 0.5 und 2.5 GeV/c die Selektionseffizienz für Elektronen zu 90% bestimmt. Im gleichen Impulsbereich liegt die Wahrscheinlichkeit, Pionen als Elektronen zu identifizieren, zwischen 0.05% und 0.1%. Auf diesem Algorithmus basiert die Messung des inklusiven Elektronen Impulsspektrums aus B-Meson Zerfällen anhand der Daten, die mit dem *BABAR* Detector am asymmetrischen Speicherring PEP-II ("B Factory") aufgezeichnet wurden. Das Volumen der analysierten Daten entspricht einer integrierten Luminosität von 4.13 fb^{-1} auf der $\Upsilon(4S)$ Resonanz und 0.97 fb^{-1} bei einer um 40 MeV verringerten Schwerpunktsenergie. $B\overline{B}$ Ereignisse werden anhand hochenergetischer Elektronen identifiziert. Elektronen von einem semileptonischen Zerfall des zweiten B-Mesons werden durch die relative Ladung und Impulsrichtung zum hochenergetischen Elektron vom Untergrund aus semileptonischen Charm Zerfällen isoliert. Das inklusive Verzweigungsverhältnis für den semileptonischen Zerfall des B-Mesons wird zu $(10.85 \pm 0.22_{(stat)} \pm 0.34_{(sys)})\%$ gemessen. Zusammen mit der Lebenszeit von B-Mesonen lässt sich daraus $|V_{cb}|$ bestimmen:
$|V_{cb}| = 0.0406 \pm 0.0009_{exp} \pm 0.0019_{theory}$.

Contents

Chapter 1

Introduction

1.1 Motivation

The goal of this analysis is to determine the inclusive semileptonic branching fraction of B mesons $\mathcal{B}(B \to Xl\nu)$ from data taken at the *BABAR* experiment. This analysis is based on the separation of electrons from hadrons, therefore the development of an algorithm for electron identification with a high selection efficiency and a low misidentification rate for hadrons is an important aspect of this work. Moreover, since *BABAR* is a very young experiment, this algorithm has to offer flexible selection criteria and must be implemented into the *BABAR* software framework in order to be useful for the whole collaboration.

From the experimental point of view, inclusive semileptonic decays are relatively easy to handle, since they can be isolated by identifying electrons (or muons), which can be performed with a high precision. Due to the high rates involved, the error on the final result is not dominated by statistical uncertainties either. Therefore, semileptonic decays provide an excellent laboratory for the study of electroweak and strong interactions. In particular, inclusive measurements, i.e. measurements that do not differentiate between final state hadrons accompanying the charged lepton and neutrino, provide a straightforward, yet not model independent way to measure the coupling to the charged weak current in terms of the CKM matrix elements V_{cb} and V_{ub}.

The results from previous measurements of $\mathcal{B}(B \to Xl\nu)$ are significantly below the theoretical calculations. Simple spectator calculations assuming the b quark decaying as free particle predict a value of 16.5%, and QCD corrections lower it to 12.5%, which is still above the current measurements. Recent theoretical developments suggest an increased rate in the process $b \to c\bar{c}s$, leading to a predicted semileptonic branching fraction between 11% and 12%. Therefore, precision measurements of $\mathcal{B}(B \to Xl\nu)$ can help to illucidate the role of QCD bound state effects in B meson decays.

A compilation of measurements of inclusive semileptonic branching ratios is presented in Table 1.1. While almost all results obtained on the Z resonance are above 11%, branching fractions determined in experiments running on the $\Upsilon(4S)$ resonance lie below 10.5%. Therefore further precision measurements on the $\Upsilon(4S)$ resonance are desirable in order to find out whether this difference is significant.

Experiment	Year	$\mathcal{B}(B_{u,d} \to Xl\nu)[\%]$	$\mathcal{B}(B \to Xl\nu)[\%]$ (on Z resonance)
CUSB [1]	1991	$10.0 \pm 0.4 \pm 0.3$	
ARGUS [2]	1993	$9.7 \pm 0.5 \pm 0.4$	
CLEO2 [3]	1996	$10.49 \pm 0.17 \pm 0.43$	
DELPHI [4]	1995	$11.56 \pm 0.41 \pm 0.23$	$11.06 \pm 0.39 \pm 0.22$
L3 [5]	1996	$11.34 \pm 0.13 \pm 0.49$	$10.85 \pm 0.12 \pm 0.47$
L3 [6]	2000	$10.61 \pm 0.14 \pm 0.31$	$10.16 \pm 0.13 \pm 0.30$
OPAL [7]	2000	$11.32 \pm 0.10^{+0.29}_{-0.25}$	$10.83 \pm 0.1^{+2.8}_{-2.4}$
ALEPH [8]	2001	$11.18 \pm 0.1 \pm 0.36$	$10.70 \pm 0.1 \pm 0.34$

Table 1.1: Measurements of the inclusive semileptonic branching fraction. Since the results obtained by the LEP experiments are averaged over B^0, B^+, B_s^0 and b - baryons, we used their lifetimes and production ratios to compute $\mathcal{B}(B_{u,d} \to Xl\nu)$.

1.2 Outline of this Dissertation

Apart from this introduction, the dissertation contains 7 further chapters:

- Chapter 2 is about the theoretical background. Starting with a very general overview, we introduce the electroweak interaction and the CKM matrix. Next, we concentrate on the mixing of neutral B mesons, since we have to account for this effect in our analysis. Since the treatment of $B^0\overline{B}^0$ oscillations differs between experiments running on the $\Upsilon(4S)$ resonance and those producing B mesons by Z^0 fragmentation, a subsection elaborates on B physics at the $\Upsilon(4S)$ resonance. The third section deals with the inclusive branching fraction, concluding with a description of how $\mathcal{B}(B \to Xe\nu)$ can be used to determine $|V_{cb}|$. Finally, several theoretical models predicting the shapes of inclusive electron spectra from B decays are introduced.

- Chapter 3 is an overview over the *BABAR* experiment. It introduces the PEP-II storage ring and the *BABAR* detector. In the description of the individual subsystems we will emphasize elements and properties important for the subsequent chapter about electron identification.

- Chapter 4 contains the description of the electron identification algorithm which is used in the later analysis. It starts with a general description of the algorithm, which is based on the combination of likelihoods. For each subsystem participating in electron identification, a separate section describes in detail how its response is translated into likelihoods.

- Chapter 5 gives an overview over the analysis.It uses lepton tags to determine the flavor of the B meson, which is the most important information for separating primary electrons ($B \to Xe\nu$) from secondary electrons ($B \to X_c \to Ye\nu$). The first part describes the general strategy, while the second part focuses on the details of this analysis.

- Chapter 6 starts with a description of all track and event selection cuts used in this analysis, along with a determination of their efficiencies and their systematic uncertainties. Then we follow the outline given in the previous chapter. Starting with the raw spectrum of identified electron tracks, the individual backgrounds are isolated and subtracted. The analysis of systematic uncertainties is done in parallel. At the end of Chapter 6 we present the inclusive electron spectrum from semileptonic B decays in the momentum range between 0.5 and 2.5 GeV/c in the $\Upsilon(4S)$ rest frame, corrected for momentum resolution and external bremsstrahlung.

- Chapter 7 uses the integrated spectra to compute the total branching fraction. This also includes the extrapolation of the measured spectrum to p=0. Finally, we compute $|V_{cb}|$ from $\mathcal{B}(B \to X l \nu)$.

- Chapter 8 gives a summary of the results obtained by this work.

Chapter 2

Theoretical Background

2.1 Particles and Interactions

2.1.1 General Overview

The most comprehensive theoretical framework for descriptions of phenomena observed in particle physics is the *Standard Model*. It represents our knowledge about fundamental particles and interactions: While all visible matter in our universe is made of quarks and leptons, both being fermions, the fundamental forces through which they interact are mediated by bosons, i.e. particles with a spin of an integer number. There are four kinds of interactions: strong, electromagnetic, weak and gravitational. Unification of electromagnetic and weak interactions to the electroweak interaction is an essential part of the Standard Model, and requires the existence of at least one "Higgs"-boson, which has not been proven yet. Discovery of the Higgs boson is the goal of two experiments planned at the Large Hadron Collider (LHC), which is currently built at CERN ("Conseil Européen pour la Recherche Nucléaire"), the European center for particle physics. Another important question is whether CP-asymmetries observed in some decays involving weak interactions can be described correctly by the Standard Model. To answer this question, the *BABAR* experiment has been built at the Stanford Linear Accelerator Center (SLAC). First results confirm the predicted existence of asymmetries in the decay of B mesons, although further precision measurements are necessary in order to test the predictions quantitatively.

There are six kinds or flavors of quarks. Their charge is either $-\frac{1}{3}e$ or $+\frac{2}{3}e$, and thus they can be arranged into three generations of doublets:

$$\begin{pmatrix} u \\ d \end{pmatrix} \begin{matrix} \text{up} \\ \text{down} \end{matrix} \qquad \begin{pmatrix} c \\ s \end{pmatrix} \begin{matrix} \text{charm} \\ \text{strange} \end{matrix} \qquad \begin{pmatrix} t \\ b \end{pmatrix} \begin{matrix} \text{top} \\ \text{bottom} \end{matrix} \qquad \begin{matrix} q = \frac{2}{3}e \\ q = -\frac{1}{3}e \end{matrix}$$

Quarks from the first generation combine to protons (uud) and neutrons (udd) and therefore make up ordinary stable matter, while higher generations of quarks decay into the lower ones. These quark doublets are paralleled by three generations of leptons:

$$\begin{pmatrix} e \\ \nu_e \end{pmatrix} \begin{matrix} \text{electron} \\ e-\text{neutrino} \end{matrix} \qquad \begin{pmatrix} \mu \\ \nu_\mu \end{pmatrix} \begin{matrix} \text{muon} \\ \mu-\text{neutrino} \end{matrix} \qquad \begin{pmatrix} \tau \\ \nu_\tau \end{pmatrix} \begin{matrix} \text{tau} \\ \tau-\text{neutrino} \end{matrix} \qquad \begin{matrix} q = -e \\ q = 0 \end{matrix}$$

According to the current Standard Model, neutrinos are massless, and transitions between leptons of different generations are forbidden. However, recent measurements

indicate oscillations of μ neutrinos, implying non-zero neutrino masses. Further experiments in this area and theoretical works on revisions of the Standard Model to describe such oscillations are another major field of todays particle physics.

2.1.2 The Strong Interaction

In contrast to leptons, quarks participate in the strong interaction. The underlying theory (QCD) introduces a new degree of freedom for quarks, the "color charge". Each of the six quarks comes in three different colors, which are denoted as "red","blue" and "green". This convention is motivated by color theory in optics: only if the "color-states" of two or three quarks would add up to "white" in optical color theory, the formation of a bound state is possible. The Lagrangian describing the strong force is derived assuming local SU(3) symmetry w.r.t. the color states. This requires the existence of eight additional gauge bosons mediating the strong force. Since SU(3) is a non-Abelian group, the Lagrangian also contains terms allowing interactions of the gluons among themselves, with three- or four-boson vertices. This results in a very large number of Feynman diagrams even for very simple processes where strong interactions are involved. An additional problem is due to the fact that the coupling strength at energy scales as present in bound states (like B mesons) is very large, disallowing calculations based on perturbation theory. Therefore, theoretical predictions of properties of meson and baryon decays always show sizable uncertainties.

2.1.3 The Electroweak Interaction and the CKM Matrix

Gauge bosons of the electroweak interaction couple to both, quarks and leptons. The construction of the Lagrangian starts with requiring local SU(2) $\times$ U(1) symmetries, where U(1) refers to a phase rotation of the fields, and SU(2) represents a flavor rotation between left-handed quarks or leptons within the same generation. This leads to 4 gauge bosons: Z^0, W^+, W^- and the photon. However, SU(2) symmetry requires massless quarks and leptons, which obviously is not the case. Therefore additional terms have to be added to the Lagrangian. These represent couplings of the fermions to a Higgs boson, which effectively gives them the required masses and thus causes a spontaneous symmetry breaking. As for the strong interaction, the non-Abelian character of the SU(2) group allows the bosons to interact with each other.

Interactions between fermions and electroweak gauge bosons can be divided into two categories:

- neutral currents, where a fermion and its anti-fermion couple to a Z^0 or γ, and
- charged currents, where fermions of different flavors couple to a W-boson.

For the description of meson decays on the tree level, only the latter category is relevant. Flavor changing charged quark transitions are described by the Lagrangian

$$\mathcal{L}_{int} = -\frac{g}{\sqrt{2}}(\mathcal{J}^{\mu}W_{\mu}^{+} + \mathcal{J}^{\mu\dagger}W_{\mu}^{-}) \,, \tag{2.1}$$

where $\mathcal{J}^\mu$ is a V-A charged weak current operator coupling to the W boson:

$$\mathcal{J}^\mu = (\bar{\nu_e}, \bar{\nu_\mu}, \bar{\nu_\tau})\gamma^\mu(1-\gamma^5)\begin{pmatrix} e^- \\ \mu^- \\ \tau^- \end{pmatrix} + (\bar{u}, \bar{c}, \bar{t})\gamma^\mu(1-\gamma^5)\begin{pmatrix} V_{ud} & V_{us} & V_{ub} \\ V_{cd} & V_{cs} & V_{cb} \\ V_{td} & V_{ts} & V_{tb} \end{pmatrix}\begin{pmatrix} d \\ s \\ b \end{pmatrix} \quad . \quad (2.2)$$

The first term allows transitions between leptons and their neutrinos. The matrix $\mathbf{V}$ in the second term is a consequence of quark flavor eigenstates not being identical to the weak interaction eigenstates. Therefore, transitions between two quarks q_1, q_2 are possible even between different generations, with their amplitudes being proportional to $|V_{q_1q_2}|$.$\mathbf{V}$ is the "Cabibbo-Kobayashi-Maskawa" (CKM) matrix, and a precise determination of its elements is the goal of the *BABAR* experiment. In this thesis, the magnitude of $|V_{cb}|$ will be determined through measuring the decay rates of $b \to cW^-, W^- \to e^-\bar{\nu}_e$.

The CKM-Matrix has to be unitary, and by removing unphysical quark phases, it can be described by four independent, real parameters, with one of them representing a complex phase $e^{i\delta}$. The only way to allow charge-parity violation, which already has been observed in the decay of K-mesons, is $\delta \neq 0$ or $\delta \neq \pi$. This would imply CP-violating asymmetries in the decay of B mesons. Therefore, measurements of such asymmetries performed at the *BABAR* experiment can answer the question whether CP-violations can be successfully explained by the Standard Model.

Experiments show that the off-diagonal elements V_{us}, V_{cb}, V_{cd} and V_{ts} are an order of magnitude smaller than the diagonal ones, and that the amplitudes for transitions between the first and third generation are even smaller. This leads to a parameterization suggested by Wolfenstein:

$$\mathbf{V} \approx \begin{pmatrix} 1-\lambda^2/2 & \lambda & A\lambda^3(\rho - i\eta) \\ -\lambda & 1-\lambda^2/2 & A\lambda^2 \\ A\lambda^3(1-\rho-i\eta) & -A\lambda^2 & 1 \end{pmatrix} .$$

It is found that $\lambda \approx 0.22$ and $A \approx 0.82$. In the complex plane, the numbers 0, 1 and $\rho + i\eta$ form a "unitarity" triangle. With β being the angle at (1,0), $\sin 2\beta$ is identical to the amplitude of the time dependent, CP violating asymmetry between $B \to J/\psi\, K_S^0$ and $\overline{B} \to J/\psi\, K_S^0$. After one year of data taking, this value has been determined to $\sin 2\beta = 0.59 \pm 0.14_{(stat)} \pm 0.05_{(sys)}$ by the *BABAR* collaboration [9], while the result given by the BELLE experiment is $\sin 2\beta = 0.99 \pm 0.14_{(stat)} \pm 0.06_{(sys)}$ [10].

2.2 Properties of B Mesons

2.2.1 Mixing of B Mesons

The oscillation of neutral B mesons between the states B^0 and $\overline{B}^0$ is called "mixing", and can be described (in leading order) by the exchange of W-bosons as depicted by the box diagrams in Fig. 2.1.
Mixing occurs because the eigenstates $|B_1\rangle, |B_2\rangle$ of the weak interaction Hamiltonian are not identical to the flavor eigenstates $|B^0\rangle$ and $|\overline{B}^0\rangle$. They can be expressed as linear combinations

$$|B_1\rangle = p|B^0\rangle + q|\overline{B}^0\rangle \quad \text{and}$$

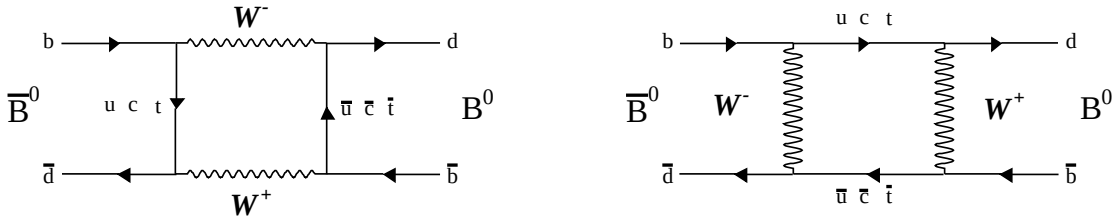

Figure 2.1: Box diagrams for $B\ \overline{B}$ mixing

$$|B_2\rangle = p|B^0\rangle - q|\overline{B}^0\rangle \ ,$$

where $|p|^2 + |q|^2 = 1$. The time evolution of these states can be expressed in terms of the masses $m_{1,2}$ and decay widths $\Gamma_{1,2}$:

$$|B_1\rangle(t) = |B_1\rangle(0)\ e^{-(im_1+\Gamma_1/2)\ t}$$

$$|B_2\rangle(t) = |B_2\rangle(0)\ e^{-(im_2+\Gamma_2/2)\ t} \ .$$

From these equations the time developments $\Psi_{B^0}(t)$ and $\Psi_{\overline{B}^0}(t)$ of initially pure B^0 and $\overline{B}^0$ states can be computed:

$$|\Psi_{B^0}\rangle(t) = \frac{e^{-(im_1+\Gamma_1/2)\ t} + e^{-(im_2+\Gamma_2/2)\ t}}{2}|B^0\rangle + \frac{q}{p}\frac{e^{-(im_1+\Gamma_1/2)\ t} - e^{-(im_2+\Gamma_2/2)\ t}}{2}|\overline{B}^0\rangle$$

$$|\Psi_{\overline{B}^0}\rangle(t) = \frac{e^{-(im_1+\Gamma_1/2)\ t} + e^{-(im_2+\Gamma_2/2)\ t}}{2}|\overline{B}^0\rangle + \frac{p}{q}\frac{e^{-(im_1+\Gamma_1/2)\ t} - e^{-(im_2+\Gamma_2/2)\ t}}{2}|B^0\rangle \ .$$

The probability of a B^0 meson decaying after the time t as $\overline{B}^0$ is then given by $|\langle B^0|\Psi_{B^0}(t)\rangle|^2$:

$$P_{B^0\to\overline{B}^0}(t) = \frac{1}{4}\left|\frac{q}{p}\right|^2 \left[e^{-\Gamma_1\ t} + e^{-\Gamma_2\ t} - 2e^{-(\Gamma_1+\Gamma_2)/2\ t}\cos(\Delta M\ t)\right]$$

$$P_{\overline{B}^0\to B^0}(t) = \frac{1}{4}\left|\frac{p}{q}\right|^2 \left[e^{-\Gamma_1\ t} + e^{-\Gamma_2\ t} - 2e^{-(\Gamma_1+\Gamma_2)/2\ t}\cos(\Delta M\ t)\right] \ ,$$

where $\Delta M = M_1 - M_2$. From these equations its becomes clear that $|p/q| \neq 1$ is a possible source of CP - violation, which is called *CP violation in mixing.*

Assuming $|p/q| = 1$, we can determine the mixing parameter χ_0, which is defined as the time integrated probability of a neutral B meson to decay as its anti-particle:

$$\chi_0 = \frac{\int_0^\infty P_{B^0\to\overline{B}^0}(t)\ dt}{\int_0^\infty P_{B^0\to\overline{B}^0}(t)dt + \int_0^\infty P_{B^0\to B^0}(t)dt} = \frac{(\Delta M)^2 + (\Delta\Gamma/2)^2}{2\Gamma^2 + 2(\Delta M)^2} \qquad (2.3)$$

where $\Delta\Gamma = \Gamma_1 - \Gamma_2$.

2.2.2 Production of B mesons in e^+ e^- Annihilation

The purest sample of B mesons can be obtained by e^+ e^- annihilations. At a center-of-mass energy of 10.58 GeV, the $\Upsilon(4S)$ resonance is produced. With a beam-energy spread achieved at current e^+ e^- colliders, the ratio between the cross section of $\Upsilon(4S)$ production and $q\overline{q}$ fragmentation is ≈ 0.25. The $\Upsilon(4S)$ decays into a pair of B mesons at a rate of almost 100%, with a ratio between B^0 $\overline{B}^0$ and B^+ B^- pairs of $f_0/f_+ \approx 1$. Since the $\Upsilon(4S)$ is an eigenstate of the parity operator P with an eigenvalue of -1, and the decay $\Upsilon(4S) \to B\overline{B}$ is mediated by the parity conserving strong interaction, the final state Ψ must have $P\Psi = -\Psi$, too. The only possible solution for a pair of neutral B mesons is

$$\Psi(0) = \frac{1}{\sqrt{2}} \left[B^0(\vec{r})\overline{B}^0(\vec{-r}) - B^0(\vec{-r})\overline{B}^0(\vec{r}) \right] \ .$$

With the equations from the previous chapter, the time evolution of this state is

$$\Psi(t) = \frac{1}{\sqrt{2}} \left[B^0(\vec{r})\overline{B}^0(\vec{-r}) - B^0(\vec{-r})\overline{B}^0(\vec{r}) \right] e^{-2iMt-\Gamma t} \ ,$$

corresponding to a coherent oscillation. After one of the B meson decays at $t = t_0$, the probability of the other B decaying as its anti-particle at $t = t_1$ is $P_{B^0 \to \overline{B}^0}(t_1 - t_0)$ and $P_{\overline{B}^0 \to B^0}(t_1 - t_0)$, respectively. This has two consequences unique for B-physics on the $\Upsilon(4S)$ resonance:

- The relative decay time has to be determined for studies involving CP-violation (for example the determination of $|p/q|$) or measurements of ΔM. Since the B mesons are produced almost at rest in the $\Upsilon(4S)$ frame, this difference cannot be measured in symmetric e^+ e^- colliders. Asymmetric machines are needed in order to infer this time difference from the spatial separation of the decay vertices.
- If the flavor of one B meson is known, for example by detection of a high energetic electron from a semileptonic decay, the time integrated probability of the other decaying as the anti-particle is given by $1 - f_0\chi_0$.

2.3 Inclusive Semileptonic Branching Fraction of B Mesons

2.3.1 Theoretical Predictions

The semileptonic branching fraction is defined as

$$\mathcal{B}_{SL} = \frac{\Gamma(B \to X_c l\nu) + \Gamma(B \to X_u l\nu)}{\Gamma(B \to anything)} \tag{2.4}$$

where l is either an electron or muon, and X_c and X_u denote any meson containing a c or u quark, respectively. The simplest model to calculate $\mathcal{B}_{SL}$ neglects any interactions between the b and light quark, and therefore is called *Spectator Model*. It predicts the same decay widths for all hadrons containing a b quark. Based on the Lagrangian given in Eq. 2.1, the matrix element for the transition $b \to W^* c, W^* \to e\nu$ (where W^* denotes a virtual W boson) factorizes into a leptonic and a hadronic component

$$\mathcal{M}(B \to X_c l\nu) = i\frac{G_F}{\sqrt{2}} V_{cb} [\bar{\psi}_c \gamma^\mu (1-\gamma_5)\psi_b][\bar{\psi}_l \gamma_\mu (1-\gamma_5)\psi_\nu] \ , \tag{2.5}$$

where G_F is the Fermi constant

$$G_F/\sqrt{2} = \frac{g^2}{8m_W^2} \ ,$$

and the ψ denote the individual Dirac spinors. Integration of $|\mathcal{M}|^2$ yields the decay width $\Gamma(B \to X_c l\nu)$. Including $b \to u$ transitions delivers the total semileptonic decay width

$$\Gamma_{SL} = \frac{G_F^2 \ m_b^5}{192 \ \pi^3} \left[|V_{cb}|^2 z_0(m_c/m_b) + |V_{ub}|^2 z_0(m_u/m_b) \right] \ , \tag{2.6}$$

with

$$z_0(x) = 1 - 8x^2 + 8x^6 - x^8 - 24x^4 \ln x \ .$$

Neglecting rare processes such as penguin decays or $b \to u$ transitions and assuming equal decay widths for e and μ semileptonic decays, the denominator of Eq. 2.4 can be decomposed into

$$\Gamma(B \to anything) \approx 2\Gamma(b \to ce\nu) + \Gamma(b \to c\tau\nu) + \Gamma(b \to c\bar{u}d + c\bar{u}s) + \Gamma(b \to c\bar{c}s + c\bar{c}d) \ .$$

In the spectator model, the decay width $\Gamma(b \to q_1, q_2, q_3)$ for a process $b \to W^* q_1, W^* \to q_2 q_3$ with three quarks q_i in the final state is

$$\Gamma(b \to q_1, q_2, q_3) = \frac{G_F^2 \ m_b^5}{192 \ \pi^3} |V_{bq_1}|^2 |V_{q_2 q_3}|^2 I\left(\frac{m_{q_1}}{m_b}, \frac{m_{q_1}}{m_b}, \frac{m_{q_1}}{m_b}\right) \ , \tag{2.7}$$

where the phase space factor $I(x, y, z)$ can be found in Ref. [11]. Inserting quark masses in Eq. 2.6 and Eq. 2.7 yields a value of $\mathcal{B}_{SL} = 16\%$ [12], which is in disagreement to the measured values between 10% and 11%. An improved calculation of $\mathcal{B}_{SL}$ needs to consider

- QCD corrections to the hadronic rate, and
- the determination of the appropriate quark masses.

For example, calculations performed by Altarelli and Petrarca [13] yield

$$\mathcal{B}_{SL} = (12.2 \pm 0.45 \pm 0.8)\% \quad \text{for} \quad m_b = 4.6 \ , m_c = 1.2 \ , m_s = 0.1 \ , m_u = m_d = 0 \quad \text{and}$$

$$\mathcal{B}_{SL} = (14.4 \pm 0.45 \pm 0.8)\% \quad \text{for} \quad m_b = 5.0 \ , m_c = 1.7 \ , m_s = 0.3 \ , m_u = m_d = 0.16 \ ,$$

where all masses are in GeV/c^2. The errors are associated to uncertainties in the renormalization scale (first term) and the strong coupling constant α_s (second term). A more recent analysis of perturbative QCD corrections performed by Bagan, Ball, Braun and Gosdzinsky [14] predicts an increased rate in the $b \to c\bar{c}s$ channel, leading to

$$\mathcal{B}_{SL} = (11.8 \pm 0.8 \pm 0.5 \pm 0.2 \pm 0.2^{+0.9}_{-1.3})\%$$

where the errors are due to uncertainties in m_b, α_s, the kinetic energy of the b quark inside the hadron, $\Gamma(b \to c\bar{c}s)$ and renormalization scale.

In summary, all theoretical predictions lie above the experimental values, with the main problems arising due to unknown quark masses (especially for the b quark) and QCD corrections, which are very difficult to perform and introduce additional large uncertainties.

2.3.2 Extraction of $|V_{cb}|$

Since $\Gamma(B \to X_c l\nu)$ is proportional to $|V_{cb}|^2$, and $\Gamma(B \to anything) = \hbar\ \tau_B^{-1}$, measurements of the B meson lifetime and of $\mathcal{B}_{SL}$ can be used to determine $|V_{cb}|$. In the Spectator Model, we have

$$\mathcal{B}(B \to X_c\ l\ \nu) = |V_{cb}|^2 \frac{G_F^2\ m_b^5}{192\ \pi^3 \hbar}\ z_0(x)\ \tau_B \qquad (x = m_c/m_b)\ .$$

With (for example) $m_b = 4.4\,\mathrm{GeV}/c^2, m_c = 1.5\,\mathrm{GeV}/c^2$, this can be rewritten as

$$|V_{cb}| = \xi_{th} \sqrt{\frac{\mathcal{B}(B \to X_c l\nu)}{0.105} \frac{1.6\,\mathrm{ps}}{\tau_B}} \qquad , \qquad \xi_{th} = 0.044\ .$$

For a precise determination of ξ_{th}, strong interactions between the heavy and the light quark cannot be neglected. In Ref. [15], Shifman *et al.* perform an operator product expansion of $\Gamma(B \to X_c l\nu)$ in terms of inverse heavy quark masses and in α_s. The first term in this $1/m_b$ expansion corresponds to the free quark decay from above, and there are no corrections of $\mathcal{O}(1/m_b)$:

$$\Gamma(B \to X_c l\nu) = \frac{G_F^2\ m_b^5}{192\ \pi^3} |V_{cb}|^2$$
$$\times \left\{ \left[z_0(x) - \frac{2\alpha_s}{3\pi}(\pi^2 - \frac{25}{4}) z_0^{(1)}(x) \right] \left(1 - \frac{\mu_\pi^2 - \mu_G^2}{2m_b^2} \right) - z_1(x) \frac{\mu_G^2}{m_b^2} + \mathcal{O}(\alpha_s^2, \alpha_s/m_b^2, 1/m_b^3) \right\}\ , \tag{2.8}$$

with $z_1(x) = (1-x^2)^4$. The function $z_0^{(1)}$ represents one-gluon perturbative QCD corrections. Non-perturbative QCD effects are described by μ_π, which can be interpreted as the kinetic energy of the b-quark, and by μ_G, which can be related to the mass difference between B and B^*: $\mu_G^2 = 0.75(m_B^2 - m_{B^*}^2)$.

In the *BABAR* Physics Book [16], the calculations from Shifman *et al.*[17] and Ball *et al.*[14] are combined to

$$\xi_{th} = 0.0400\ \eta_{QED}\ (1 \pm 0.030 \pm 0.024 \pm 0.025 \pm 0.012)\ , \tag{2.9}$$

with $\eta_{QED} \approx 1.007$. The errors account for uncertainties in higher order perturbative corrections, the dependence on the mass difference $m_b - m_c$, the mass of the b quark, and unknown corrections of $\mathcal{O}(1/m_b^3)$, respectively.

2.4 Models for Inclusive Semileptonic Spectra

2.4.1 The ACCM Model

The model developed by Altarelli, Cabibbo, Corbo, Maiani and Martinelli [13] incorporates bound-state effects through a relative motion of the heavy quark w.r.t. the light quark within the B meson, resulting in a three dimensional momentum distribution

$$\Phi(|\vec{p}|) = \frac{4}{\sqrt{\pi} p_F^3} e^{-|\vec{p}^2|/p_F^2}$$

for the b-quark. While the spectator quark is assumed to have a fixed mass m_{sp}, the mass of the heavy quark is constrained by energy and momentum conservation to be

$$m_b^2 = m_B^2 + m_{sp}^2 - 2M_B\sqrt{m_{sp}^2 + p^2} \ .$$

Boosting the decay distribution of the b-quark into the rest frame of the B meson yields the lepton energy spectrum [12]:

$$\begin{aligned}\frac{d\Gamma(b \to ql\nu, x)}{dx} =& |V_{qb}|^2 \frac{G_F^2 m_b^5}{96\ \pi^3} \frac{x^2(x_m - x)^2}{(1-x)^3} \\ & \times [(1-x)(3-2x) + (1-x_m)(3-x)] \left[1 - \frac{2\alpha_s}{3\pi} G(x,\epsilon)\right] \ ,\end{aligned}$$

with $x = 2E_l/m_b$, $x_m = 1 - (m_q/m_b)^2$ (m_q = mass of daughter quark), and $G(x,\epsilon)$ representing QCD-corrections discussed in [18].

2.4.2 Form Factor Models

In general, the interactions between the light and heavy quarks within a meson cannot be neglected. The matrix element in Eq. 2.5, which assumes a free b quark, is therefore unsuitable. Generally, the amplitude for a semileptonic decay of a meson $M_{Q\bar{q}}$ into a meson $X_{q'\bar{q}}$ is described by

$$\mathcal{M}(M_{Q\bar{q}} \to X_{q'\bar{q}} l\nu) = -i\ \frac{G_F}{\sqrt{2}} \langle X_{q'\bar{q}} | \mathcal{J}_{had}^{\mu} | M_{Q\bar{q}} \rangle\ \ [\bar{\psi}_l \gamma_\mu (1-\gamma_5) \psi_\nu] \ ,$$

where $\mathcal{J}_{had}^{\mu}$ is the hadronic part of the charged weak current operator given in Eq. 2.2. While $\bar{\psi}_l \gamma_\mu (1-\gamma_5)\psi_\nu$ can still be calculated easily, the weak hadronic current $\langle X_{q'\bar{q}} | \mathcal{J}_{had}^{\mu} | M_{Q\bar{q}} \rangle$ cannot be computed in a simple manner due to complicated strong interactions. It is the goal of form factor models to find parameterizations for these hadronic currents.

2.4.3 The ISGW and ISGW2 Models

The model from Isgur, Scora, Grinstein and Wise [19] is based on a non-relativistic description of the B meson decay. The bound state is modeled by a potential containing a Coulomb and a linear component:

$$V(r) = -\frac{4\alpha_s}{3\ r} + b\ r + c \ ,$$

where $\alpha_s = 0.5$, $c = -0.84\,\mathrm{GeV}$ and $b = 0.18\,\mathrm{GeV}^2$. The solutions of the Schrödinger equation for this potential are based on harmonic-oscillator wave functions; for example

$$\Psi^{1S} = \frac{\beta_S^{3/2}}{\pi^{3/4}} e^{-\beta_S^2 r^2/2} \ ,$$

$$\Psi_{11}^{1P} = \frac{\beta_P^{5/2}}{\pi^{3/4}}\ r\ e^{-\beta_P^2 r^2/2} \ ,$$

$$\Psi^{2S} = \sqrt{2/3}\frac{\beta_S^{7/2}}{\pi^{3/4}}(r^2 - \frac{3}{2}\beta_S^{-2})e^{-\beta_S^2 r^2/2} \ .$$

With these solutions, the matrix elements can be computed. For decays with a D or D^* in the final state, these are

$$\langle D|\mathcal{J}^\mu_{had}|B\rangle = f_+(q^2)\ (p_B + p_D)_\mu + f_-(q^2)\ (p_B - p_D)_\mu \ , \text{ and} \tag{2.10}$$

$$\langle D^*|\mathcal{J}^\mu_{had}|B\rangle = f(q^2)\ \epsilon^*_\mu + a_+(q^2)(\epsilon^* p_B)(p_B + p_{D^*})_\mu + a_-(q^2)(\epsilon^* p_B)(p_B - p_{D^*})_\mu \ , \tag{2.11}$$

where f_+, f_-, f, a_+ and a_- are the form factors, which depend on q^2, the 4-momentum transfer between initial and final state meson. They are normalized at $q^2 = q^2_{max}$, and take the form

$$F(q^2) \propto F(q^2_{max})\ e^{-\frac{q^2 - q^2_{max}}{\kappa Q^2}} \ .$$

Isgur *et al.* considered several final states; apart from D and D^*, the form factors for decays into higher states (denoted as D^{**}), such as 1^3P_2, 1^3P_1, 1^3P_0, 1^1P_1, 2^1S_0 and 2^3S_1, are computed, too. This also leads to a prediction of the relative branching ratios:

$$\frac{\mathcal{B}(B \to Dl\nu)}{\mathcal{B}(B \to X_c l\nu)} = 0.27 \ , \ \frac{\mathcal{B}(B \to D^* l\nu)}{\mathcal{B}(B \to X_c l\nu)} = 0.62 \ , \ \frac{\mathcal{B}(B \to D^{**} l\nu)}{\mathcal{B}(B \to X_c l\nu)} = 0.11 \ .$$

In 1995, Isgur *et al.* presented a modified version of this model [20], which is called ISGW2 model. It has the following improvements:

- relativistic corrections,
- consideration of hyperfine interactions in the meson wave functions, and
- modified form factors which meet the requirements of heavy quark effective theory at non-zero values of $q^2_{max} - q^2$.

The latter item results in a different parameterization of the form factors by making the replacement

$$exp\left[-\frac{1}{6}r^2_{wf}(q^2_{max} - q^2)\right] \to \left[1 + \frac{1}{6N}r^2(q^2_{max} - q^2)\right]^{-N} \ ,$$

where $N = 2 + n + n'$ with n and n' being the harmonic oscillator quantum numbers of the initial and final state wave functions. For definitions of r and r_w see Ref. [20]. The predicted branching ratios are

$$\frac{\mathcal{B}(B \to Dl\nu)}{\mathcal{B}(B \to X_c l\nu)} = 0.29 \ , \ \frac{\mathcal{B}(B \to D^* l\nu)}{\mathcal{B}(B \to X_c l\nu)} = 0.61 \ , \ \frac{\mathcal{B}(B \to D^{**} l\nu)}{\mathcal{B}(B \to X_c l\nu)} = 0.10 \ .$$

2.4.4 HQET Derived Form Factors

Within the HQET framework, the matrix elements can be written as [21]

$$\langle D|\mathcal{J}^{\mu}_{had}|B\rangle = \left\{(p_B+p_D)_\mu - \frac{m_B^2-m_D^2}{q^2}q_\mu\right\} f_+(q^2) + \left\{\frac{m_B^2-m_D^2}{q^2}q_\mu\right\} f_0(q^2) \ ,$$

$$\begin{aligned}\langle D^*|\mathcal{J}^{\mu}_{had}|B\rangle = {} & \epsilon^*_\mu(m_B+m_{D^*})A_1(q^2) - (p_B+p_{D^*})_\mu(\epsilon^* p_B)\frac{A_2(q^2)}{m_B+m_{D^*}} \\ & - q_\mu(\epsilon^* p_B)\frac{2m_D}{q^2}(A_3(q^2)-iA_0(q^2)) + \epsilon_{\mu\nu\rho\sigma}\epsilon^{*\nu}p_B^\rho p_{D^*}^\sigma\frac{2V(q^2)}{m_B+m_{D^*}} \ , \end{aligned} \quad (2.12)$$

where ϵ^* is the polarization vector of the D^*, and f_0, f_+, A_1, A_2, V are the form factors. $A_3(q^2)$ is defined as

$$A_3(q^2) = \frac{m_{D^*}+m_B}{2m_{D^*}}A_1(q^2) - \frac{m_{D^*}-m_B}{2m_{D^*}}A_2(q^2) \ , \qquad A_0(0) = A_3(0) \ .$$

According to HQET, the form factors A_1, A_2 and V can be written as [22]

$$A_1(q^2) = \frac{m_B+m_{D^*}}{2\sqrt{m_B m_{D^*}}}\left[1-\frac{q^2}{(m_B+m_{D^*})^2}\right]h_{A_1}(w) \quad (2.13)$$

$$A_2(q^2) = \frac{m_B+m_{D^*}}{2\sqrt{m_B m_{D^*}}}R_2(w)h_{A_1}(w) \quad (2.14)$$

$$V(q^2) = \frac{m_B+m_{D^*}}{2\sqrt{m_B m_{D^*}}}R_1(w)h_{A_1}(w) \quad (2.15)$$

where w is the relativistic factor γ of the D^* in the B-meson rest frame. In the heavy quark symmetry limit ($m_b, m_c \to \infty$), the function $h_{A_1}(w)$ is identical to the Isgur-Wise function, and $R_1(w), R_2(w)$ are unity. Assuming that $R_1(w)$ and $R_2(w)$ can be described by constants R_1,R_2, and $h_{A_1}(w)$ has the form $h_{A_1}(w) = h_{A_1}(1)[1-\rho^2_{A_1}(w-1)]$, the CLEO collaboration has performed a fit to the measured lepton spectrum of the decay $B \to D^* l\nu$ in order to determine R_1, R_2 and ρ_{A_1} [22]. The results are

$$R_1 = 1.18 \pm 0.3 \pm 0.12 \quad , \quad R_2 = 0.71 \pm 0.22 \pm 0.07 \quad \text{and} \quad \rho^2_{A_1} = 0.91 \pm 0.15 \pm 0.06 \ .$$

In the *BABAR* Monte Carlo simulation package, the lepton spectra for the decay channel $B \to D^* l\nu$ are generated using this model, with the CLEO results as input parameters.

Chapter 3

The *BABAR* Experiment

3.1 Introduction

Primary goal of the *BABAR* experiment is the precise measurement of *CP* violating asymmetries in the decay of B mesons produced by the process

$$e^+e^- \to \Upsilon(4S) \to B\overline{B} \ .$$

Performing such studies on the $\Upsilon(4S)$ resonance relies on measurements of the relative decay time of the B mesons. Since these have a short lifetime and are produced almost at rest, an asymmetric e^+ e^- collider is required to infer this quantity from the decay lengths. The branching fractions for the relevant decay channels, which need to be *CP* eigenstates, are very small (for example $\mathcal{B}(B \to J/\psi K^0_S) \approx 10^{-4}$). Therefore, a very high luminosity has to be provided.

The PEP-II B Factory, located at the *Stanford Linear Accelerator Center*, has been designed to meet these requirements. It consists of two storage rings for electrons and positrons with beam energies of 9 GeV and 3.1 GeV, respectively (Fig. 3.1), which translates into a center-of-mass energy of 10.58 GeV. This energy corresponds to the mass of the $\Upsilon(4S)$ resonance, which is produced at a rate of $\approx 3\,\mathrm{s}^{-1}$, with a Lorentz boost of $\beta\gamma$ = 0.56 in the laboratory frame. This leads to an average separation of 240 μm between the two B decay vertices. PEP-II has been completed in July 1998, and due to continuous improvements of the beam quality and increasing currents, the design luminosity goal of $3 \times 10^{33}\,\mathrm{cm}^{-2}\mathrm{s}^{-1}$ has been reached. In October 2001, the average daily integrated luminosity was $\approx 250\,\mathrm{pb}^{-1}$, corresponding to ≈ 275000 B meson pairs.

The *BABAR* detector, a general-purpose magnetic spectrometer, started operation in May 1999. The two primary objectives are

- the precise determination of charged particle trajectories and photon momenta in order to reconstruct B meson decay vertices with a resolution better than 80 μm, and
- an excellent identification of electrons, muons and kaons to determine the flavor of at least one B meson and to distinguish as many decay channels as possible.

As depicted in Fig. 3.2, it consists of five main components: tracking information for charged particles is provided by the Silicon Vertex Tracker and Drift Chamber, which

operate within a magnetic field of 1.5 T generated by a superconducting solenoid. Photons (and neutral pions) are reconstructed by the Electromagnetic Calorimeter, which also serves as central subsystem for electron identification. Kaons and protons are separated from pions by a Cerenkov detector. An instrumentation of the iron yoke for the magnetic flux return with Resistive Plate Chambers is used for neutral hadron and muon detection.

In the following chapters, we elaborate on each of these subsystems in more detail, including descriptions of the basic reconstruction strategies relevant for electron identification. We use the *BABAR* coordinate system, which is defined in the following way:

- the +z axis is parallel to the magnetic field of the solenoid and in the direction of the e^--beam.
- the +y axis points vertically upward.
- the +x axis points horizontally, away from the center of the PEP-II ring.
- the origin, (0,0,0), is defined as the nominal interaction point.

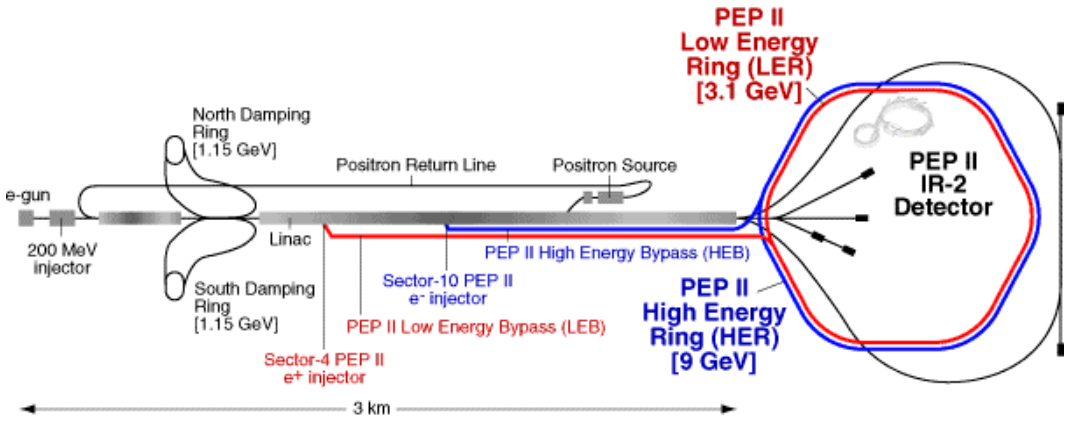

Figure 3.1: Acceleration and storage system at PEP-II . Prior to injection into the storage rings, electrons and positrons are accelerated by the Stanford Linear Collider (SLC).

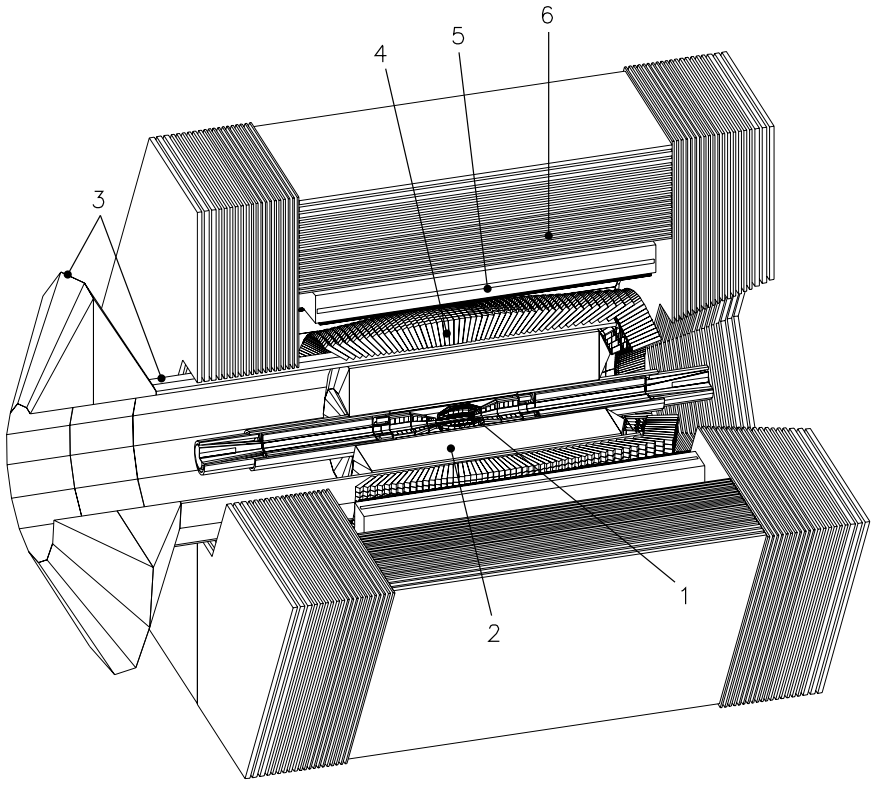

Figure 3.2: Layout of the *BABAR* detector: Silicon Vertex Detector(1), Drift Chamber(2), Cerenkov Detector(3), Electromagnetic Calorimeter (4), Magnet Coil(5) and Instrumented Flux Return(6). The electron beam enters the detector from the left.

3.2 The Silicon Vertex Tracker

The Silicon Vertex Tracker (SVT) has been designed to reconstruct the decay vertices of the two B mesons in order to measure the time interval between their decays. This is an essential information for the measurement of CP violation in B decays and analyses dealing with $B^0\overline{B}^0$ mixing. It consists of five concentric cylindrical layers with radii between 32 mm for the innermost and 144 mm for the outermost one. Each layer is divided azimuthally into detector modules, which are arranged in a way that neighboring ones overlap each other, ensuring a full azimuthal coverage. Each module has readout strips on both sides: while those on the inner sides are perpendicular to the beam axis to measure the z coordinate, the strips on the outer side are arranged parallel to the z axis to measure the azimuthal angle. The readout pitch in ϕ varies between 50 μm for the first and 100 μm for the last layer, and between 100 and 210 μm in z. The single point resolution achieved is in the order of 15 μm and 30-40 μm for layers 1–3 and 4–5 respectively. It has been shown that the position resolution for B decay vertices lies between 60 and 100 μm (depending on the decay mode) and therefore fulfills the design requirements [23]. Another task is the reconstruction of low energetic charged particles, especially pions from D^* decays, since a minimum transverse momentum of 100 MeV/c is necessary to reach the Drift Chamber. Further, by measuring the time interval during which the signal exceeds a certain threshold, the charge induced on the readout strips can be determined. This leads to a $\mathrm{d}E/\mathrm{d}x$ measurement which can be used for particle identification.

The SVT plays a central role in providing an accurate estimate of the interaction point for each event, which is called the *Primary Vertex* from now on. The underlying algorithm is described in Ref. [24].

3.3 The Drift Chamber

Reconstruction of particles with transverse momenta greater than 100 MeV/c is the main task of the Drift Chamber. Its shape is that of a 280 cm long cylinder, with an inner radius of 26.6 cm and an outer radius of 80.9 cm. Due to the boost along the z axis, the center is offset by 37 cm from the interaction point, leading to an asymmetric polar angular coverage of $17^\circ < \theta < 150^\circ$ in the laboratory frame. The sense wires are made of gold-plated Tungsten-rhenium with a diameter of 20 μm. Each of these is surrounded by 6 field wires consisting of aluminum (80–120 μm diameter), making up a hexagonal structure called *Drift Cell* with a typical dimension of $1.2 \times 1.8\,\mathrm{cm}^2$. The chamber contains 7104 cells, which are arranged in 40 cylindrical layers, with four layers being grouped into one superlayer. In order to reconstruct the 3 dimensional trajectory of a particle, the wires within different superlayers show different stereo angles: apart from axial (A), there are also superlayers with positive (U) and negative (V) stereo angles, with their absolute values increasing with the radius of each layer. The arrangement of the 10 superlayers follows the pattern AUVAUVAUVA. The gas chosen for operating the Drift Chamber is a mixture of Helium and Isobutane (80% : 20%), and the voltage for the sense wires has been set to 1960 V, ensuring a high tracking efficiency of 98% for transverse momenta above 200 MeV/c. Beginning in January 2001, this voltage has been lowered to 1930 V.

Another task is the determination of energy loss per unit distance $\mathrm{d}E/\mathrm{d}x$ from the charge collected within each cell, which is an important information for particle identification. The average resolution of the $\mathrm{d}E/\mathrm{d}x$ measurements is 7.5% [25].

3.4 Cerenkov Detector

The Detector of Internally Reflected Cerenkov light (DIRC) is designed for hadronic particle identification, in particular for pion/kaon separation up to 4 GeV/c. The basic idea is to detect Cerenkov light produced by charged particles moving faster than the speed of light within a radiator of refractive index n (i.e. $v > c/n$). The light is emitted under the Cerenkov angle Θ_c, which depends on the momentum p and particle mass m:

$$\cos\Theta_c = \frac{\sqrt{1+(m/p)^2}}{n} \; .$$

Therefore, combined with a measurement of the momentum (from the tracking system), Θ_c can be used identify particles. With $n = 1.473$, kaons start radiating at momenta above 460 MeV/c, making the DIRC a useful device for rejecting kaons and protons at low momenta.

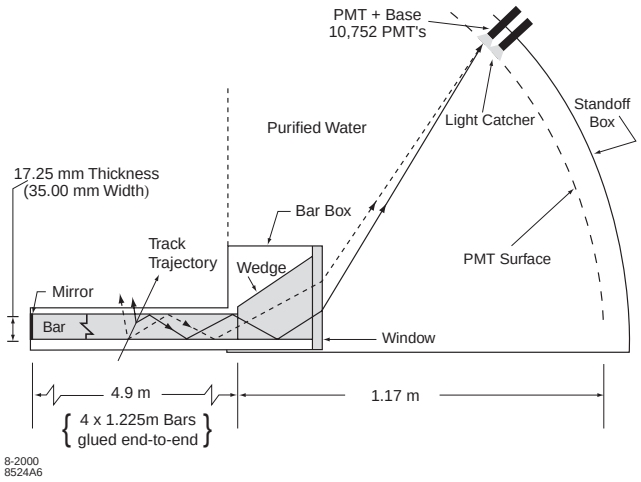

Figure 3.3: Schematic view of the DIRC fused silica radiator bar (grey), Standoff Box (white) and imaging region (dashed lines) [25].

The design of the DIRC (Fig. 3.3) introduces a novel type of ring imaging Cerenkov (RICH) detector based on total internal reflection of Cerenkov light. *BABAR* is the first experiment to use this technique for the primary hadronic particle identification system. The radiator, which consists of 144 straight fused silica ("quartz") bars with rectangular cross sections, is located between the Drift Chamber and the Electromagnetic Calorimeter. It is subdivided into 12 azimuthal regions, each being formed by a bar box containing 12 bars. The total amount of material at normal incidence corresponds to 19% of a radiation length. Due to gaps between the boxes, the azimuthal coverage is 93%. Because of total reflectance and mirrors placed at the front end of each bar box, light emitted by charged particles traveling through the radiator cannot leave the bars, until

after multiple reflections the rear end is reached. The photons exit into an expansion region ("Standoff Box") filled with 6000 liters of purified water and are detected by a close packed array of 10572 photomultiplier tubes (PMTs), mounted on the toroidal surface on the back. Each PMT has a diameter of 2.82 cm and is operated directly in water, with an average distance of 1.2 m to the end of the fused silica bars. Except for a number discrete ambiguities, the magnitude of the Cerenkov angle is preserved during this process. To resolve these ambiguities, measurements of the photon arrival times and pattern recognition algorithms are used.

The basic strategy for reconstructing the Cerenkov angle Θ_c by the time this analysis has been performed is the "DrcMaxLikelihood" - method [26]: for a given track, impact point and angle of incidence on the radiator are computed. Based on these parameters, the expected photon arrival time (including the time of flight between interaction point and radiator) can be determined for each PMT signal. Only those PMT signals whose measured photon arrival times and angular measurements are close to the expected ones (for any of the 5 stable particle hypotheses) are used. By these preselection criteria, a very good reduction of background photons is achieved. A fit based on the remaining PMT signals determines the most likely value of Θ_c, plus the number of signal and background photons contributing to this measurement. However, it should be noted that due to the nature of this method, the values of Θ_c obtained from "bad" measurements like those caused by differences between true and assumed track directions (due to multiple scattering in the outer DCH support tube), or too many remaining background photons associated to hadron tracks below the Cerenkov threshold, tend to be biased towards one of the expected values for stable particles. Starting in January 2001, a new method ("DircGlobalLikel") which reduces such biases has been introduced.

The achieved resolution of 2.4 mrad, as measured in di-muon events, leads to a 3 σ separation between kaons and pions at 4 GeV/c. Although the resolution decreases at lower momenta, it will be shown that the DIRC is very successful in electron/pion separation below 0.7 GeV/c (Sect. 4).

3.5 Electromagnetic Calorimeter

The *BABAR* Electromagnetic Calorimeter (EMC) is the principal device for electron/pion separation, photon and neutral pion reconstruction. The angular coverage corresponds to $-0.775 < \cos\theta < 0.962$ in the laboratory frame, and $-0.916 < \cos\theta^* < 0.895$ in the center-of-mass frame. It consists of 6580 crystals made out of CsI(Tl), which features a small Molière radius (R_m=3.8 cm) and a short radiation length ($X_0 = 1.85$ cm), allowing for precise angular measurements and fully contained showers with a relatively compact design. Together with a high photon yield, an excellent energy resolution is achieved [25]:

$$\frac{\sigma_E}{E} = \frac{(2.32 \pm 0.30)\%}{\sqrt[4]{E(GeV)}} \oplus (1.85 \pm 0.12)\% \ .$$

As shown in Fig. 3.4, the Calorimeter is composed of a cylindrical Barrel section ($26.9^\circ < \theta < 140.8^\circ$) and a forward conic Endcap ($15.8^\circ < \theta < 26.9^\circ$). With an inner radius of 91 cm and an outer radius of 136 cm, the Barrel is located within the magnet cryostat. It consists of 48 polar angle rows, each having 120 identical crystals in azimuthal angle. The arrangement is different in the Endcap, where 820 crystals are

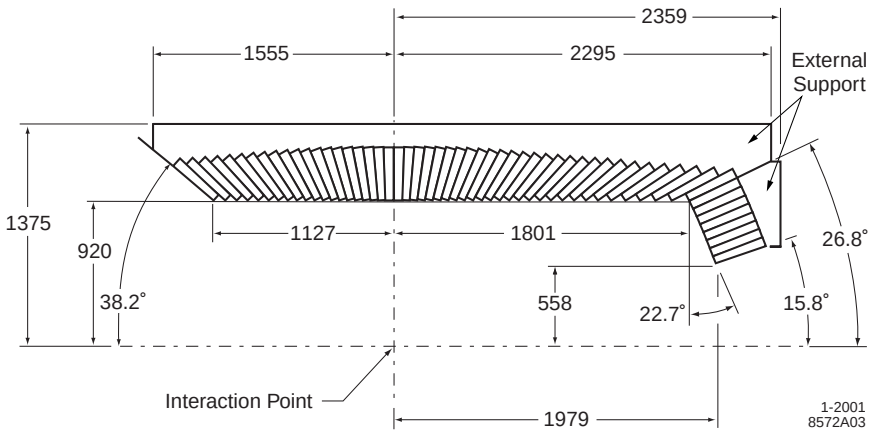

Figure 3.4: A longitudinal cross section of the EMC (only the top half is shown). All dimensions are given in mm.

divided into 8 polar angle rows with a segmentation in ϕ varying between 80 and 120 crystals.

To account for the boost, which leads to higher photon energies at smaller polar angles, the crystal lengths increase from 29.76 cm (16.1 X_0) in the backward region to 32.55 cm (17.6 X_0) in the Endcap. Mounted on the back of each crystal, two silicon PIN diodes covering an area of 4 cm^2 collect scintillation light. They are surrounded by a reflector plate to prevent the loss of photons missing the diodes. Preamplifiers are connected to each diode, with the whole system being encompassed by a metallic housing to provide shielding against RF noise. Two foils of Tyvek 1056D wrapped around each crystal diffusely reflect light exiting through the side faces. The crystals are held by modules made of carbon-fiber composite (CFC) with 300 μm-thick walls between the individual compartments. Altogether, the inactive material between to crystals leads to gaps of about 1.25 mm. To minimize the loss of photons entering the EMC at those gaps, the crystal axis show a non-projectivity in θ.

Since the energy deposited by a particle is scattered over many crystals, a clustering algorithm needs to be applied. Starting with a seed crystal whose energy measurement exceeds a certain threshold (5 MeV), all neighboring crystals with energy depositions exceeding a lower threshold (1 MeV) are associated to the seed. This procedure is repeated iteratively for each of these neighbors, leading to a set of adjacent crystals called *EmcCluster*, which represents the energy deposited by one or more particles. If the energy distribution within the *EmcCluster* shows more than one local maximum, it is split into as many *EmcBumps*, with each bump representing the energy deposited by a single particle. *EmcClusters* with one local maximum only are called *EmcBumps*, too. The position $\vec{r}_{Bump}$ of an *EmcBump* is calculated from the individual energy depositions E_i and crystal positions $\vec{r}_i$ according to the formula

$$\vec{r}_{Bump} = \sum_i \left[\vec{r}_i (4 + \ln \frac{E_i}{E_{Bump}}) \right] \ , \tag{3.1}$$

which leads to an angular resolution of

$$\sigma_\theta = \sigma_\phi = \left(\frac{3.87 \pm 0.07}{\sqrt{E(\,\mathrm{GeV})}} \pm 0.04 \right) \,\mathrm{mrad}$$

for photons [25]. Based on the Bump positions and impact points of the combined SVT and DCH tracks on the EMC, charged tracks and *EmcBumps* are combined to *Charged EmcCandidates*. Bumps with no associated track are called *Neutral EmcCandidates*.

3.6 Instrumented Flux Return

The Instrumented Flux Return (IFR) has been designed to identify muons and to detect neutral hadrons. It consists of a Barrel and two Endcaps (Fig. 3.5) made of iron, covering polar angles between 17° and 157°. The iron is segmented into 18 plates, with Resistive Plate Chambers (RPC) mounted in the 17 gaps of 3.2 cm width. The thickness of the individual plates increases in the outer layers, which has been motivated by Monte Carlo studies showing that small absorber thicknesses improve muon- and K_L^0 detection during the first absorption length only, therefore allowing wider absorbers and less readout layers at larger distances. The total thickness of the iron plates amounts to 65 cm (Barrel) and 60 cm (Endcaps). The Barrel contains four additional readout layers: two layers of cylindrical RPCs located between the EMC and magnet coil, which in turn is surrounded by an inner layer of planar RPCs, and one layer mounted on the outer iron plates.

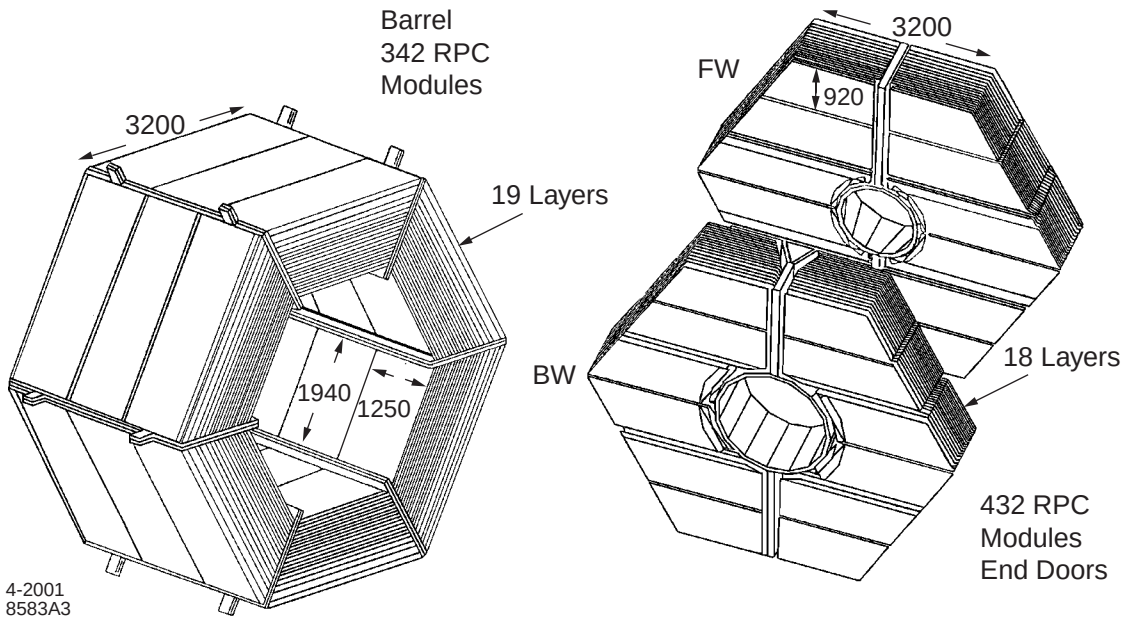

Figure 3.5: Barrel (left) and Endcap regions (right) of the IFR

Chapter 4

Electron Identification

4.1 Overview

To separate electrons from muons and hadrons, three subsystems are utilized: The Electromagnetic Calorimeter(EMC), the Drift Chamber(DCH), and the Cerenkov Detector (DIRC).

Based on pure data samples of electrons, pions, kaons and protons, whose selection criteria are described below, the discriminating variables involved in electron identification are discussed. This is done in two steps: first, a set of loose preselection cuts is developed. In the second step, probability density functions are constructed for each discriminating variable. Under the assumption of independent measurements from the individual subdetectors, they are combined to compute the likelihood $L(\xi)$ for each particle hypothesis $\xi \in \{e; \pi; K; p\}$:

$$L(\xi) = P(x_{EMC}, x_{DCH}, x_{DRC}; \xi) = P(x_{EMC}; \xi) P(x_{DCH}; \xi) P(x_{DCH}; \xi) \ , \tag{4.1}$$

where x_{EMC}, x_{DCH} and x_{DCH} represent vectors of discriminating variables from each subsystem. Weighting the individual likelihoods with *a priori* probabilities p_ξ, the likelihood fraction f_L is computed:

$$f_L = \frac{p_e L(e)}{p_e L(e) + p_\pi L(\pi) + p_K L(K) + p_p L(p)} \ . \tag{4.2}$$

Using $p_e : p_\pi : p_K : p_p = 1 : 5 : 1 : 0.1$, a track is selected as electron if it passes the preselection cuts and a given cut on f_L, which may vary between 0 and 1. For our analysis, we will choose $f_L > 0.95$.

Finally, electron identification efficiency and hadron fake rates are measured on data, applying the same selection strategy to obtain pure particle samples on a dataset covering the time period when the measurement of $\mathcal{B}(B \to Xe\nu)$ is performed.

4.2 Pure Particle Samples

4.2.1 Electrons

A pure sample of electron tracks is obtained from radiative Bhabha events. For events with exactly two oppositely charged tracks, we define $p^*_{1,2}$ as their momenta in the CMS,

and $p_{1,2}$ as the corresponding momenta in the laboratory frame. With the numbering selected such that $p_1^* > p_2^*$, the following properties are required:

- $p_1^* > 4$ GeV/c
- The DCH track with the higher momentum in the CM frame must be associated to an energy deposition E_1 in the electromagnetic calorimeter satisfying $E_1/p_1 > 0.5$.
- At least one neutral EmcCandidate with $E_{dep} > 0.5\,\mathrm{GeV}$.
- The highest energetic neutral EmcCandidate must have a separation of at least 20° from the track with the lower CMS momentum.
- $p_1\ c + p_2\ c + E_{neutral} > 11$ GeV, with $E_{neutral}$ being the sum of all energy depositions not associated to a DCH track.

The track with the lower momentum in the CM frame is added to the electron sample. According to Monte Carlo studies, the purity of this sample exceeds 99.9%.

4.2.2 Pions

The K_s^0 lifetime (0.89 x 10^{-10} s) is sufficiently long to produce a decay vertex which is well separated from the interaction region. Hence the process $K_s^0 \to \pi^+\pi^-$ is easy to identify, yielding a pure pion sample. To suppress combinatoric background and contributions from photon conversions or Λ decays, a specific set of cuts has been developed [27]. Performing this selection on a mixture of simulated generic $\Upsilon(4S)$ decays and continuum events, the purity of this sample is determined to be 99.5%, while the fraction of electrons is below 0.01%.

Invariant mass $m(\pi^+\pi^-)$ [GeV/c^2]	$0.488 < m(\pi^+\pi^-) < 0.508$
Distance between K_s^0 vertex $\vec{r}_{K_s^0}$ and primary vertex $\vec{r}_{pv}$	$\lvert\vec{r}_{K_s^0} - \vec{r}_{pv}\rvert > 1$ cm
Opening angle δ_1 between π^+ and π^-	$\delta_1 > 0.3$ rad
Angle δ_2 between reconstructed momentum $\vec{p}_{K_s^0}$ and flight direction	$\delta_2 := \angle(\vec{p}_{K_s^0}; \vec{r}_{K_s^0} - \vec{r}_{pv}) < 0.2$ rad
Helicity angle δ_3 between π^+ direction in the K_s^0 rest frame and the K_s^0 direction	$\lvert cos\ \delta_3\rvert + 1.4 * \delta_2[\mathrm{rad}] < 0.75$
Distances of closest approach $d_{1,2}$ of the pion tracks to the primary vertex	$d_1 + d_2 < 1.2$ cm

Table 4.1: Cuts for $K_s^0 \to \pi^+\pi^-$ selection.

To enlarge the pion sample at momenta above 1.8 GeV/c, we additionally use $\tau^+\tau^-$ pairs with 3-1 track topology. To isolate such events, the *BABAR* working group on *tau* decays developed a set of selection criteria based on topological variables only [28]. Since a sizable number of radiative Bhabha events containing a photon conversion also passes these requirements, we apply the following additional cuts to reduce this background contribution:

- The track on the one-prong side must be matched to an EmcCluster with $E_{dep} < 0.4\,\mathrm{GeV}$.

- The tracks on 3-prong side must have a common vertex with a probability of $P(\chi^2_{vtx}) > 0.01$.
- No neutral EmcCandidate with $E_{dep} > 0.2$ GeV or exactly two neutral EmcCandidates which can be reconstructed as π^0 ($0.1\ \text{GeV}/c^2 < m(\gamma\gamma) < 0.16\ \text{GeV}/c^2$).

Monte Carlo studies indicate that above 1.8 GeV/c the electron contamination of this sample is comparable to the $K^0_s \to \pi^+\pi^-$ sample.

4.2.3 Kaons

The process $D^* \to D^0\pi\,; D^0 \to K\pi$ can be identified using kinematical cuts only, and therefore serves as source of pions and kaons. The selection, originally developed by the *BABAR* PID group [27], has been refined for this analysis and is summarized in Table 4.2. The purity of this sample is 95%, with an electron contamination of ≈ 0.1 %.

Invariant mass of D^0 [GeV/c^2] Mass difference Δm between D^* and D^0[GeV/c^2]	$1.845 < m(D^0) < 1.88$ $0.14445 < \Delta m < 0.14645$
Opening angle $\delta_1^{K\pi}$ between kaon and pion	$\delta_1^{K\pi} < 2$ rad
Opening angle $\delta_1^{D_0\pi_s}$ between D^0 and slow pion	$\delta_1^{D_0\pi_s} < 0.4$ rad
Momentum p_{π_s} of soft pion	$p_{\pi_s} < 0.5$ GeV/c
Distances of closest approach d_K, d_π(pion from D^0) and d_{π_s} (soft pion) to primary vertex	$d_k + d_\pi < 0.05$ cm $d_{\pi_s} < 0.03$ cm
Helicity angle δ_3 between kaon in D^0 rest frame and D^0 direction	$cos\ \delta_3 >$ - 0.9

Table 4.2: Cuts for $D^* \to D^0\pi\,; D^0 \to K\pi$ selection.

4.2.4 Protons

We extract protons from the decay $\Lambda \to p\pi$. The identification of this process benefits from the relatively long lifetime of the Λ (2.63 x 10^{-10}s), resulting in a well separated decay vertex. Conversions and K^0_s decays contribute significantly to the background. Therefore we require a positive identification of the pion track (based on the dE/dx measurement in the Drift Chamber) and also apply a veto on the K^0_s mass. Table 4.3 summarizes all cuts, which yield a proton sample with a purity of 98% and an electron contamination of $\approx 0.05\%$.

4.3 EMC Based Electron Identification

4.3.1 Deposited Energy

Electrons entering the electromagnetic calorimeter produce an electromagnetic shower. Since the CsI crystals extend between 16.1 and 17.6 radiation lengths X_0, almost the whole kinetic energy is deposited. Therefore the distribution of E_{dep}/p is very narrow and in an ideal calorimeter would be centered at unity. In practice, the distribution is centered at 0.95 and shows a non-Gaussian tail at lower values of E_{dep}/p which is due to

Invariant mass [GeV/c^2]	$1.113 < m(p\pi) < 1.119$
Distance between Λ vertex $\vec{r}_\Lambda$ and primary vertex $\vec{r}_{pv}$	$\lvert\vec{r}_\Lambda - \vec{r}_{pv}\rvert > 1$ cm
Opening angle δ_1 between p and π	$\delta_1 > 0.1$ rad
Angle δ_2 between reconstructed momentum $\vec{p}_\Lambda$ and flight direction	$\delta_2 := \angle(\vec{p}_\Lambda; \vec{r}_{Lambda} - \vec{r}_{pv})$ $\delta_2 < 0.05$ rad
dE/dx based confidence level $CL(\pi)$ of pion track	$CL(\pi) > 0.1$
Number of SVT hits N_{svt} of the pion track	$N_{svt} > 0$
Cut on invariant mass assuming pion mass for proton	$m(\pi\pi) < 0.48$ GeV/c^2 or $m(\pi\pi) > 0.51$ GeV/c^2

Table 4.3: Cuts for $\Lambda \to p\pi$ selection.

- material in front of the calorimeter (0.25 - 0.4 X_0 mainly from DCH and DIRC) and between individual crystals;
- leakage through the sides caused by the staggered crystal arrangement; and
- reconstruction inefficiencies.

As opposed to electrons, muons deposit their energy within a few crystals through ionization only, resulting in a measurement of E_{dep} between 150 and 250 MeV. Hence they can be separated from electrons by a very loose cut on E_{dep}/p. For electrons, we require

$$E_{dep}/p > 0.5 \ .$$

Since a typical electromagnetic shower induced by electrons with momenta above 300 MeV/c leads to energy depositions in more than 10 crystals, we choose

$$N_{cry} \geq 4$$

as additional preselection criterion on the number of crystals associated to a shower. We also place an upper limit on E_{dep}/p in order to reduce the fake rate of anti-protons, which may annihilate in the EMC:

$$E_{dep}/p < 1.5 \ .$$

Since the detailed shape of the E_{dep}/p depends on the momentum and polar angle, we divide the sample of pure electrons into bins of p and $\hat{\theta}$, the polar angle of the point where the track intersects the EMC. We use 100 MeV/c bins in p for $0.3 < p < 1.2$ GeV/c, 200 MeV/c bins for p>1.2 GeV/c, and 12 bins in $\cos\hat{\theta}$:

$$\cos\hat{\theta}^i \in \{-0.74; -0.56; -0.4; -0.2; 0; 0.2; 0.4; 0.56; 0.68; 0.78; 0.85; 0.89; 0.95\} \ .$$

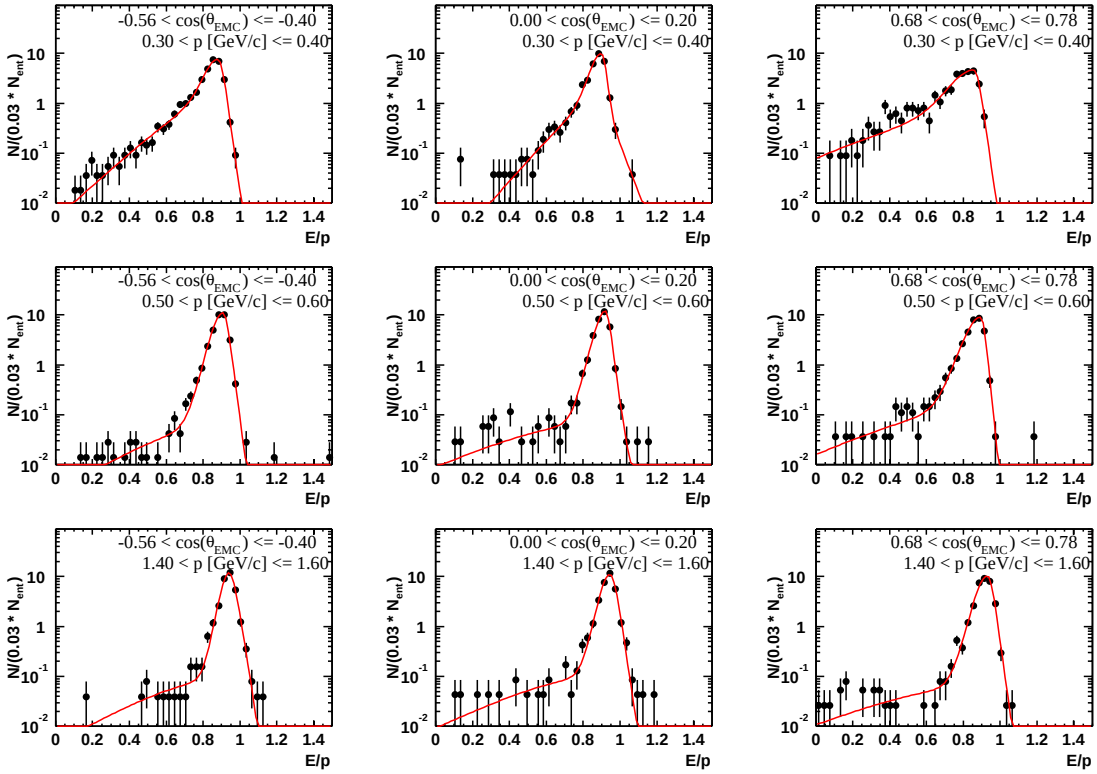

Figure 4.1: E/p distributions for electrons in different momentum and $\hat{\theta}$ bins.

To derive the probability density function within momentum bin #i and $\cos\hat{\theta}$ bin #j, a function of the form

$$g^{ij}(x;e) = \begin{cases} \frac{A^{ij}r_1^{ij}}{\sigma_1^{ij}} f\left(\frac{x-x_0^{ij}}{\sigma_1^{ij}}\right) + \frac{A^{ij}(1-r_1^{ij})}{\sigma_2^{ij}} f\left(\frac{x-x_0^{ij}}{\sigma_2^{ij}}\right) & for\ x < x_0^{ij} \\ \frac{B^{ij}r_2^{ij}}{\sigma_3^{ij}} f\left(\frac{x-x_0^{ij}}{\sigma_3^{ij}}\right) + \frac{B^{ij}(1-r_2^{ij})}{\sigma_4^{ij}} f\left(\frac{x-x_0^{ij}}{\sigma_4^{ij}}\right) & for\ x \geq x_0^{ij} \end{cases} \tag{4.3}$$

with

$$f(x) = \frac{e^{-x}}{(1+e^{-x})^2} \tag{4.4}$$

is fitted to E_{dep}/p histograms accumulated for each bin (Fig. 4.1). The fit parameters are x_0,r_1,r_2, σ_1,σ_2,σ_3 and σ_4, with (A,B) being computed such that $g^{ij}(x;e)$ is continuous at x_0 and normalized to unity. The function f has a Gaussian-like shape near 0, while it falls like $e^{-|x|}$ at large x and therefore is suitable to model the non-Gaussian tails of the distributions.

To compute the probability of the electron hypothesis for a given track, we determine the two momentum/$\cos\hat{\theta}$ bins $i_1, i_2/j_1, j_2$ whose centers are closest to the measured momentum / polar angle. The probability is then a bilinear interpolation in p and $\cos\hat{\theta}$ between the values of the g^{ij} in these bins:

$$P^{i}_{eop}(x;\hat{\theta},e) = g^{ij_1}(x;e) + \frac{g^{ij_2}(x;e) - g^{ij_1}(x;e)}{\cos\hat{\theta}_{j_2} - \cos\hat{\theta}_{j_1}}(\cos\hat{\theta} - \cos\hat{\theta}_{j_1}) \tag{4.5}$$

$$P_{eop}(x;p,\hat{\theta},e) = P^{i_1}_{eop}(x;\hat{\theta},e) + \frac{P^{i_2}_{eop}(x;\hat{\theta},e) - P^{i_1}_{eop}(x;\hat{\theta},e)}{p_{i_2} - p_{i_1}}(p - p_{i_1}) \tag{4.6}$$

Since $g^{ij}(x;e)$ is normalized to unity for each (i,j), it follows that $P_{eop}(x;p,\hat{\theta},e)$ is also normalized to unity for each value of p and $\hat{\theta}$.

Apart from ionization, pions, kaons and protons can also induce hadronic showers, leaving a larger fraction of their energy in the calorimeter. Therefore the distribution of E_{dep}/p is modeled by a sum of two Gaussians representing minimum ionizing and interacting particles:

$$g^{ij}(x;h) = \frac{r^{ij}}{\sqrt{2\pi}\,\sigma_1^{ij}}\; e^{-\frac{1}{2}\left(\frac{x-x_1^{ij}}{\sigma_1^{ij}}\right)^2} + \frac{1-r^{ij}}{\sqrt{2\pi}\,\sigma_2^{ij}}\; e^{-\frac{1}{2}\left(\frac{x-x_2^{ij}}{\sigma_2^{ij}}\right)^2} \quad . \tag{4.7}$$

$$h \in \{\pi; K; p\}$$

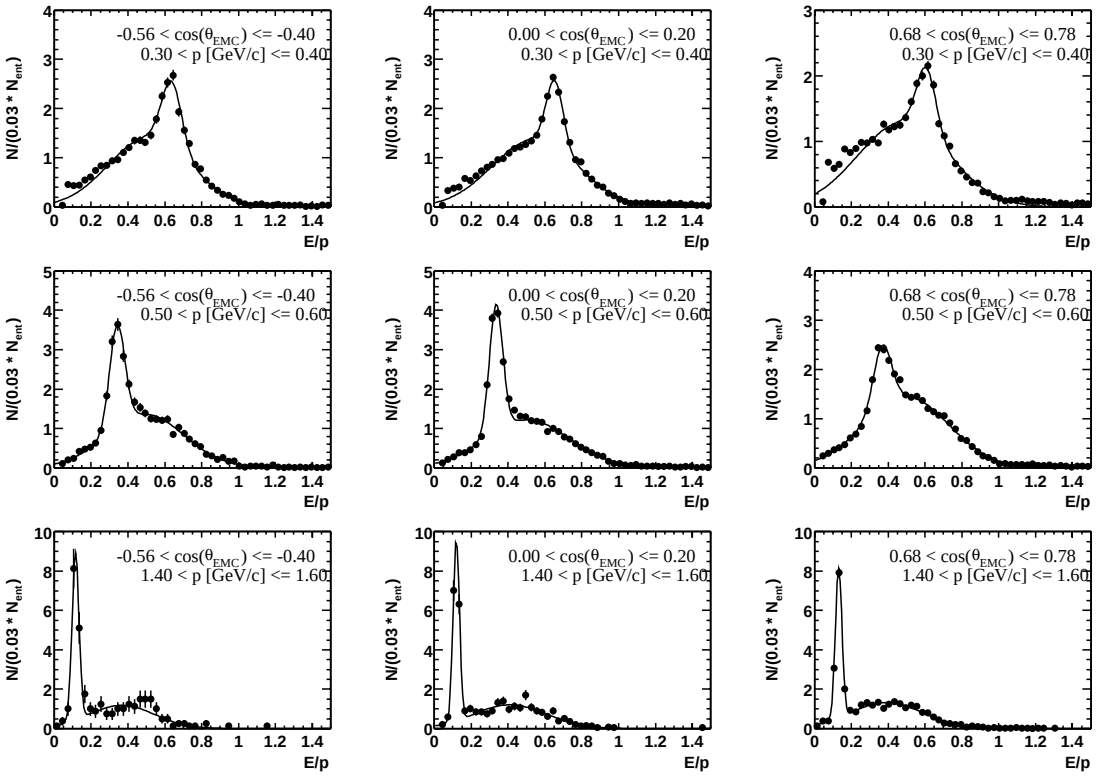

Figure 4.2: E_{dep}/p distributions for pions in different momentum and $\hat{\theta}$ bins.

As for electrons, we use a pure sample of pions to create E_{dep}/p histograms in bins of p and $\cos\hat{\theta}$ (using the same binning), and determine the parameters r, x_1, x_2, σ_1 and σ_2 by a fit (Fig. 4.2). For kaons and protons, we only use a 1 dimensional binning in p due to the smaller size of the kaon and proton samples. In the same way as $P_{eop}(x; p, \hat{\theta}, e)$, the probability density function $P_{eop}(x; p, \hat{\theta}, h)$ is defined as interpolation between the fitted $g^{ij}(x; h)$, ensuring a constant normalization to unity for each momentum and polar angle.

4.3.2 Lateral Shower Shape

To enhance the separation between electrons and interacting hadrons, the lateral energy distribution is analyzed. The different properties of electromagnetic and hadronic showers show up in the following variable:

$$LAT = \frac{\sum_{i=3}^{N} E_i r_i^2}{\sum_{i=3}^{N} E_i r_i^2 + E_1 r_0^2 + E_2 r_0^2} \ , \tag{4.8}$$

with

- N = number of crystals associated to the shower.
- E_i = energy deposited in i-th crystal, with a numbering such that $E_1 > E_2 > E_3 > .. > E_N$.
- r_i = lateral distance between center of shower (see Eq. 3.1) and i-th crystal.
- $r_0 = 5\,\mathrm{cm}$, which is approximately the average distance between two crystals.

For CsI, the Molière radius R_m is 3.8 cm. Therefore, the largest fraction of an electromagnetic shower is contained in 2-3 crystals, and since the two highest energies are omitted in the numerator of Eq. 4.8, LAT becomes small. The probability density function describing the LAT distribution of electrons is derived in the same way as for E_{dep}/p, except that a sum of two Gaussians as given in Eq. 4.7 is fitted to the distributions (Fig. 4.3).

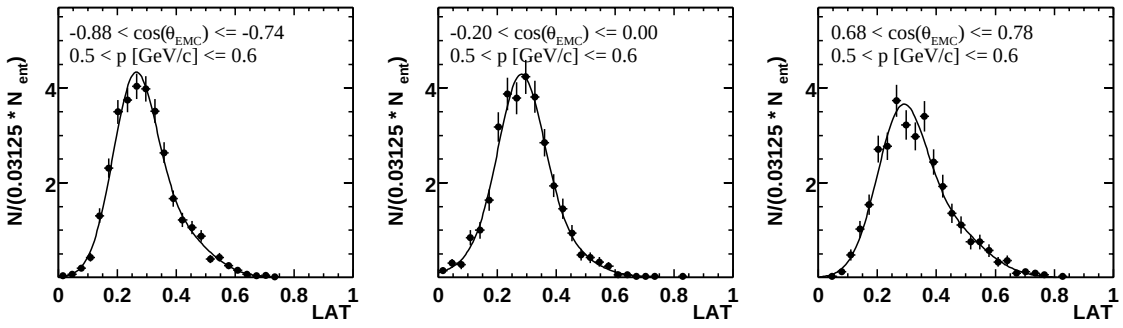

Figure 4.3: Distribution of LAT for electrons.

On the other hand, the lateral energy distribution of hadronic showers is less concentrated, with bigger energy depositions at greater distances. The higher the fraction of kinetic energy deposited in the EMC, the more pronounced is this effect (Fig. 4.4). Therefore, independent probability density functions for E_{dep}/p and LAT cannot be assumed in case of hadrons. With $x = E_{dep}/p$, $y = LAT$, and $h \in \{\pi, K, p\}$, we use the Ansatz:

$$P_{eop,LAT}(x, y; p, \hat{\theta}, h) = P_{eop}(x; p, \hat{\theta}, h) * P_{LAT}(x, y; p, h) \ . \tag{4.9}$$

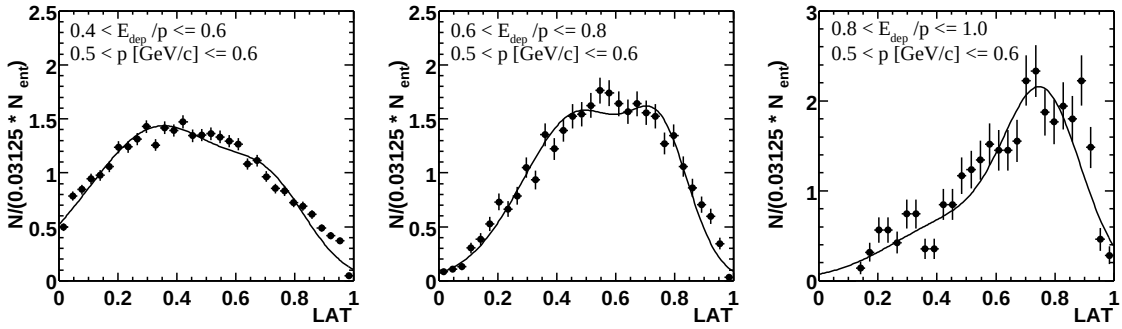

Figure 4.4: Distribution of LAT for pions.

$P_{eop,LAT}$ can be considered as a two dimensional probability density function of x and y if

$$\int P_{eop,LAT}(x, y; p, \hat{\theta})\ dx\ dy = 1 \ \forall\ p, \hat{\theta} \ , \tag{4.10}$$

for which sufficient conditions are

$$\int P_{eop}(x; p, \hat{\theta}, h)\ dx = 1 \ \forall\ p, \hat{\theta} \tag{4.11}$$

and

$$\int P_{LAT}(x, y; p, h)\ dy = 1 \ \forall\ x, p \ .$$

Eq. 4.11 is already fulfilled. Dividing the pure pion sample into bins of p and E_{dep}/p , we fit functions as given by Eq. 4.7 to the normalized LAT distributions in each bin. For a given momentum p, $P_{LAT}(x, y; p, h)$ is then computed as a linear interpolation in p of the fit results. For pions, we use 7 bins in E_{dep}/p , with limits at 0, 0.2, 0.4, 0.6, 0.8, 1.0, 1.2 and 3.0. For kaons and protons, only 2 bins ([0,0.4] and [0.4,3]) are used.

4.3.3 Longitudinal Shower Shape

To distinguish electrons from interacting hadrons, an additional information is provided by the difference $\Delta\Phi$ between the polar angles where the track intersects the EMC and

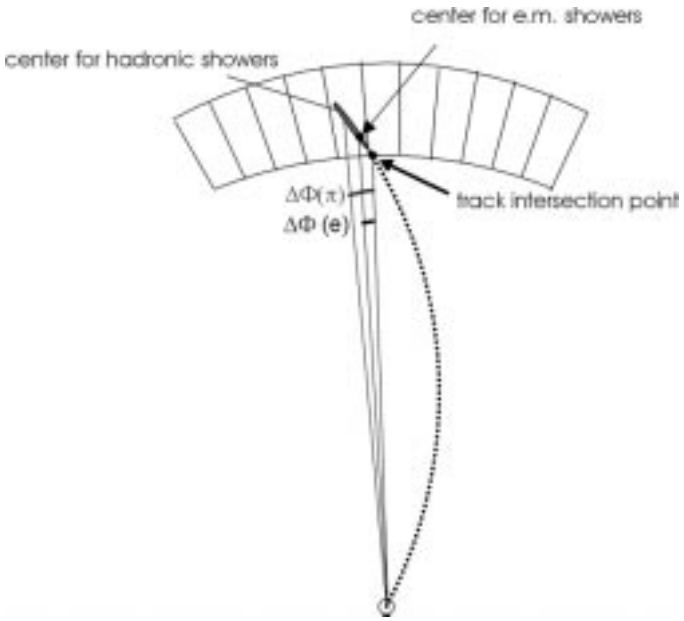

Figure 4.5: Electromagnetic showers reach their maximum close to the impact point on the EMC, while the centers of hadronic show a wider distribution in $\Delta\Phi$.

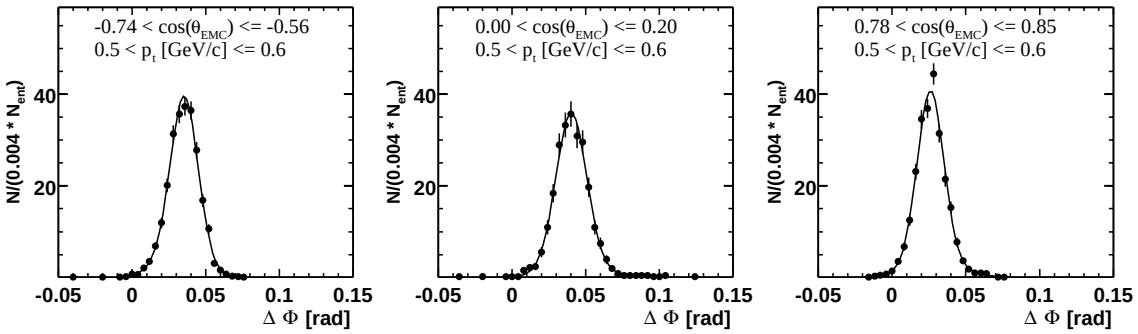

Figure 4.6: $\Delta\Phi$ distribution for electrons.

the shower center as defined in Eq. 3.1. Due to the curvature of the track in the xy plane, this angle carries information about the longitudinal energy distribution (Fig. 4.5).

Because electromagnetic showers reach their maximum earlier than hadronic ones, their center is close to the impact point of the track on the EMC (Fig. 4.6). The probability density function of $\Delta\Phi$ for electrons is constructed in the same way as for LAT , except that the data is divided into bins of p_t instead of p. For hadrons, the situation is analogous to the previous section: the stronger the interaction of a hadron in the EMC, the better the separation from electrons using $\Delta\Phi$ (Fig. 4.7). Therefore, we use the same approach for a probability density function:

$P_{\Delta\Phi}(\Delta\Phi, E_{dep}/p; p_t, h)$ with

$$\int P_{\Delta\Phi}(z, E_{dep}/p; p_t, h)dz = 1 \; \forall \; p_t, E_{dep}/p \tag{4.12}$$

is computed from interpolating the fitted $\Delta\Phi$ distributions of adjacent p_t bins.

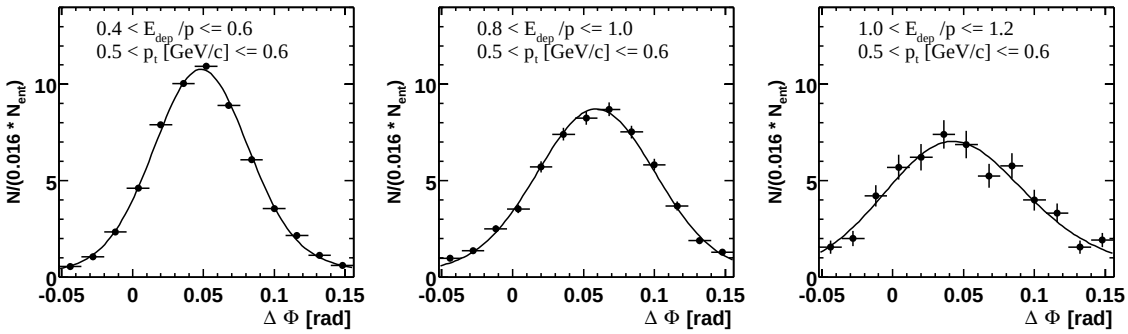

Figure 4.7: $\Delta\Phi$ distribution for pions.

4.3.4 Summary

With the preselection cuts

$$1.5 > E_{dep}/p > 0.5$$
$$N_{cry} \geq 5$$

electrons are separated from muons. For all other particle hypotheses e/π/K/p, the three dimensional distribution of E_{dep}/p, LAT and $\Delta\Phi$ is described by a probability density function which has momentum p and polar angle $\hat{\theta}$ as parameters. For electrons, the measurements are assumed to be independent, resulting in a factorizing function:

$$P_{EMC}(E_{dep}/p, LAT, \Delta\Phi; p, \hat{\theta}, e) = P_{eop}(E_{dep}/p; p, \hat{\theta}, e) \; P_{LAT}(LAT; p, \hat{\theta}, e) \; P_{\Delta\Phi}(\Delta\Phi; p, \hat{\theta}, e) \tag{4.13}$$

For hadrons, the correlations between the shower shape variables and E_{dep}/p are taken into account, while their $\hat{\theta}$ dependency is neglected:

$$\begin{aligned} P_{EMC}(E_{dep}/p, LAT, \Delta\Phi; p, \hat{\theta}, h) =& P_{eop}(E_{dep}/p \; ; p, \hat{\theta}, h) \\ & \times P_{LAT}(LAT, E_{dep}/p \; ; p, h) \; P_{\Delta\Phi}(\Delta\Phi, E_{dep}/p \; ; p, h) \end{aligned} \tag{4.14}$$

4.4 DIRC Based Electron Identification

At low energies, the electron - hadron separation is enhanced by taking the response of the DIRC into consideration. For momenta below 1.5 GeV/c, we therefore develop probability density functions for the measured Cerenkov angle Θ_c. Above 1.5 GeV/c, we do not use this subsystem for electron identification.

4.4.1 Number of Detected Photons

The Cerenkov threshold for a particle of mass m traveling through material with a refractive index n is given by

$$p_{thres} = \frac{m}{\sqrt{n^2 - 1}} \ . \tag{4.15}$$

Since $n = 1.4725$ [26], electrons in the relevant energy region (p > 300 MeV/c) passing through the DIRC always emit Cerenkov light. To avoid tracks not producing a sufficient number of photons due to a too short path length within the quartz bars or not passing the DIRC at all, a minimum number of *expected* photons $N_{\gamma,e}$ is required for each track:

$$N_{\gamma,e} > 6 \ . \tag{4.16}$$

$N_{\gamma,e}$ is determined as a function of geometric and kinematic track variables using the full DIRC simulation [29]. For tracks not passing this cut, the response of the DIRC is ignored since it does not provide sufficient information. Otherwise, we require a minimum number of *detected* photons

$$N_{\gamma} > 6 \ , \tag{4.17}$$

in order to reject the kaons and protons below the Cerenkov threshold (456 MeV/c and 868 MeV/c, respectively). This cut also ensures a reliable Cerenkov angle measurement [30].

4.4.2 Cerenkov Angle Distribution for Pions

As shown in Fig. 4.8, the resolution of the measured Cerenkov angle Θ_c is sufficient to provide additional information for the separation of electrons from pions at low momenta. Since pions produced at the interaction point can decay to muons, and due to δ - ray production within the quartz bars, the distribution of Θ_c has to be described by a sum of three Gaussians:

$$P_{DRC}(\Theta_c|\pi) = \frac{1 - r_1 - r_2}{\sqrt{2\pi}\sigma} \, e^{-\frac{1}{2}\left(\frac{\Theta_c - \Theta_{c,\pi}}{\sigma}\right)^2} + \frac{r_1}{\sqrt{2\pi}\sigma} \, e^{-\frac{1}{2}\left(\frac{\Theta_c - \Theta_{c,e}}{\sigma}\right)^2} + \frac{r_2}{\sqrt{2\pi}\sigma} \, e^{-\frac{1}{2}\left(\frac{\Theta_c - \Theta_{c,\mu}}{\sigma}\right)^2} \ , \tag{4.18}$$

where $\Theta_{c,\xi}$ is the expected Cerenkov angle for particle hypothesis ξ. Fitting this function to Θ_c distributions obtained from a pure pion sample within bins of momentum p and polar angle θ, the variation of the parameters σ, r_1 and r_2 is studied. Figure 4.9 shows the momentum dependence of the resolution σ: the lower the momentum,

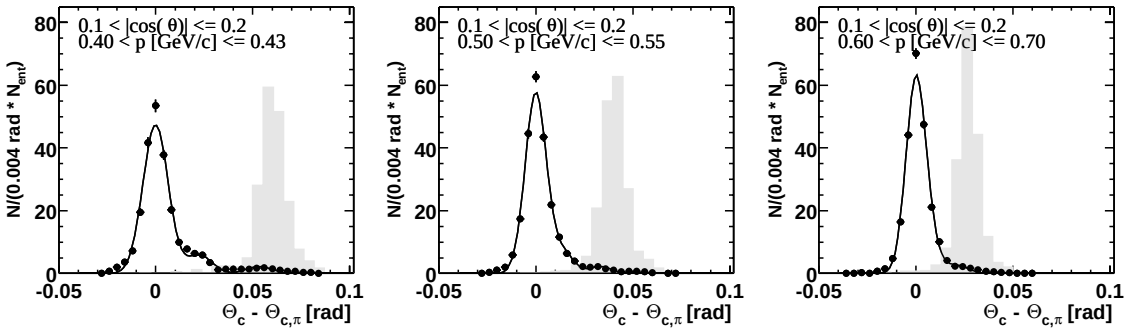

Figure 4.8: Θ_c distribution for pions; the grey histograms show the distribution for electrons

the stronger the curvature of the track within the quartz bars. Since the measurement of the Cerenkov angle assumes a constant direction of the trajectory (as given at the entry point into the DIRC), this curvature causes a decreasing resolution with decreasing transversal momentum. Therefore we decompose the resolution in a p_t-independent and a p_t - dependent part

$$\sigma(p,\theta) = \sqrt{\sigma_0^2(\theta) + \frac{\sigma_1^2(\theta)}{(p\ sin\theta)^2}} \tag{4.19}$$

where σ_0 and σ_1 are determined by fitting this function to the σ vs. p curves obtained in the previous step. Since the number of detected photons, which depends on the path length within the DIRC and therefore on $|\cos\theta|$ (or the dip-angle) also influences the resolution (the more photons, the more precise the measurement), we have to determine σ_0 and σ_1 within bins of $|\cos\theta|$. Finally, this dependence is parameterized by fitting a third-order polynomial to the $\sigma_{1,2}$ vs. $|\cos\theta|$ graphs:

$$\sigma_0(\theta) = p_0^0 + p_1^0|\cos\theta| + p_2^0|\cos\theta|^2 + p_3^0|\cos\theta|^3 \ ,$$

and

$$\sigma_1(\theta) = p_0^1 + p_1^1|\cos\theta| + p_2^1|\cos\theta|^2 + p_3^1|\cos\theta|^3 \ .$$

When traveling through the quartz bars, pions can produce secondary electrons ("δ-electrons") by ionization. These electrons also emit Cerenkov light, and the final measurement of Θ_c may result in a measurement compatible with the electron hypothesis rather than the pion hypothesis. The parameter r_1 in Eq. 4.18 represents the fraction of such tracks, and Fig. 4.10 shows its momentum dependence, which has a minimum near 0.5 GeV/c. Since the underlying process is ionization, we describe this dependence by a "Bethe-Bloch like" function:

$$r_1(p,\theta) = c_0(\theta)\ \beta^{-c_1(\theta)}\ (\beta\gamma)^{c_2} \tag{4.20}$$

Since the ionization probability also depends on the path length through the DIRC, the parameters c_0,c_1 and c_2 must be determined in different bins of $|\cos\theta|$. Performing the corresponding fits to the p vs. r_1 curves shows that c_2 can be approximated by a constant value of 2.5, while $c_0(\theta)$ and $c_1(\theta)$ can be described by a third order polynomial.

The fraction of pions decaying into muons before entering the DIRC and therefore causing a measurement near $\Theta_{c,\mu}$ is represented in Eq. 4.18 by r_2. The momentum dependence is modeled using the decay law

$$r_2(p,\theta) = 1 - e^{-\frac{L(\theta)}{c\tau\ \beta\gamma}} \tag{4.21}$$

where a 3rd order polynomial is used to parameterize the $|\cos\theta|$ - dependence of the flight length L between primary vertex and impact point onto the DIRC.

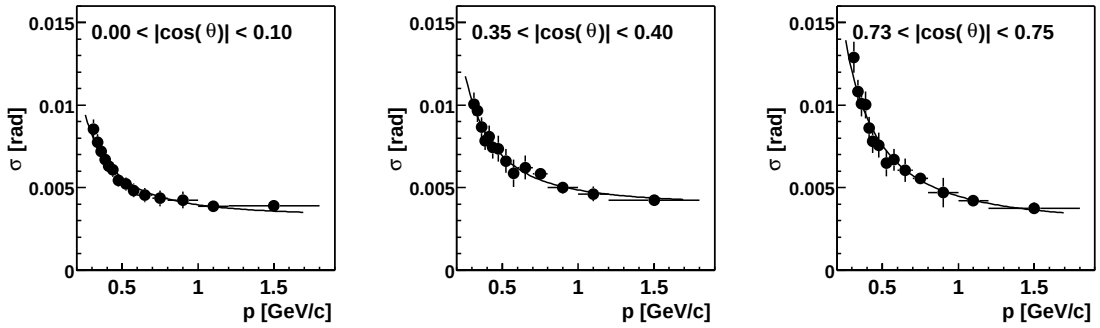

Figure 4.9: Resolution of Θ_c measurement vs. momentum for different polar angles

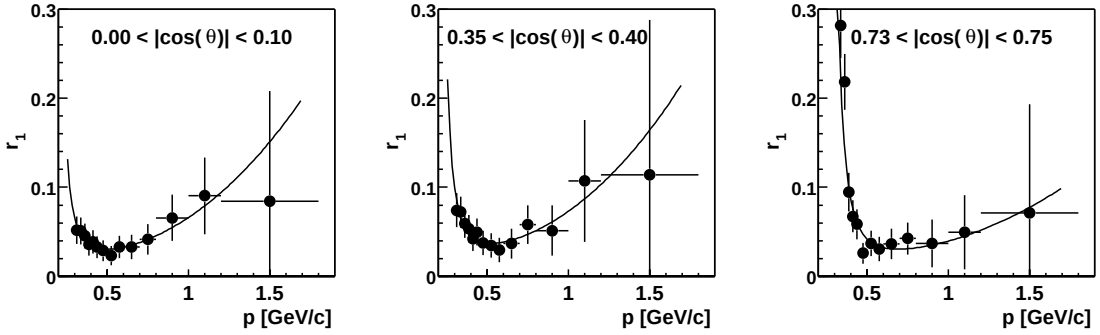

Figure 4.10: Fraction of pions with electron compatible Θ_c measurements due to δ - ray production

4.4.3 Cerenkov Angle Distribution for Electrons

The Θ_c distributions for electrons (Fig. 4.11) show non Gaussian tails at lower values. This can be explained by bremsstrahlung: if the electron interacts within or close to the

quartz bars, its flight direction is different from the expectation derived by interpolating the DCH measurement. This results in an incorrect angular measurement of the individual photons, and since Θ_c is obtained from a biased fit based on the single photon angles (Sect. 3.4), the result is more likely to be near the expectation for pions than above $\Theta_{C,e}$. We model the probability density function as a sum of two Gaussians:

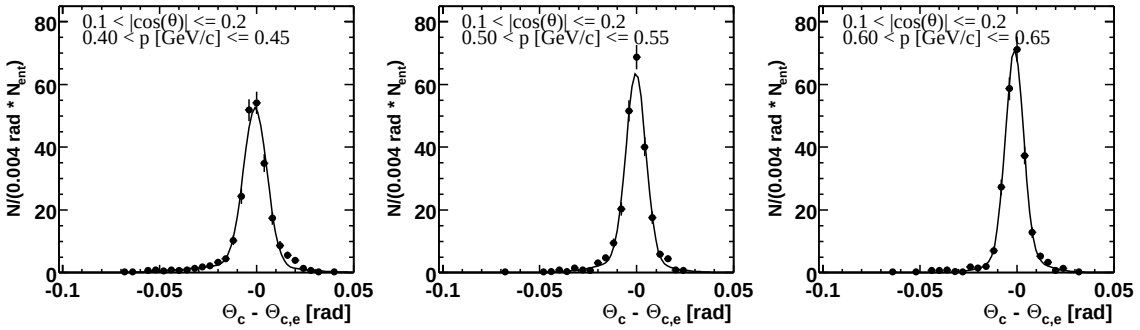

Figure 4.11: Θ_c distribution for electrons

$$P_{DRC}(\Theta_c|e) = \frac{1-r}{\sqrt{2\pi}\sigma_n} e^{-\frac{1}{2}\left(\frac{\Theta_c - \Theta_{c,e}}{\sigma_n}\right)^2} + \frac{r}{\sqrt{2\pi}\sigma_w} e^{-\frac{1}{2}\left(\frac{\Theta_c - \Theta_{c,e} - \epsilon}{\sigma_w}\right)^2} \tag{4.22}$$

The variation of the parameters σ_n,σ_w,ϵ and r is studied in the same way as for pions. To parameterize σ_n, we use the same approach as in the previous section, obtaining compatible fit results. For the second Gaussian, the functions

$$\sigma_w(p,\theta) = \frac{k_0(\theta)}{p - k_1(\theta)} \quad \text{and} \quad \epsilon(p,\theta) = \frac{k_2(\theta)}{p - k_3(\theta)} \tag{4.23}$$

with k_i being 3rd order polynomials in $|\cos\theta|$ can be used to describe the results from fitting Eq. 4.22 to the observed distributions (Fig. 4.13). It turns out that r can be fixed to a constant value of 0.85.

4.4.4 Cerenkov Angle Distribution for Kaons and Protons

For kaons and protons above threshold, the Θ_c distribution is described by a Gaussian centered at the expected value. The resolution $\sigma(p,\theta)$ is parameterized in the same way as for pions. Tracks below the Cerenkov threshold also may have associated more than 6 photons due to

- scintillation,
- mis-associations from other tracks, or
- background radiation from PEP-II storage ring.

For this reason, each track satisfying the preselection cut $N_\gamma > 6$ below kaon/proton threshold is assigned a non-zero kaon/proton likelihood, assuming a flat probability density function for Θ_c.

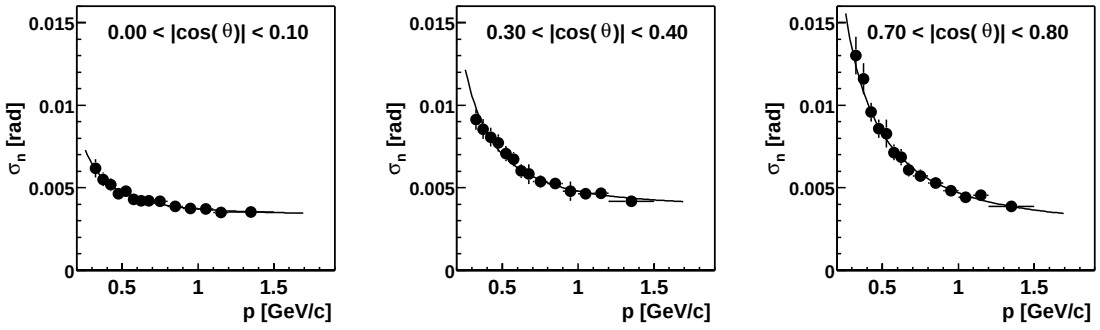

Figure 4.12: Θ_c resolution for electrons.

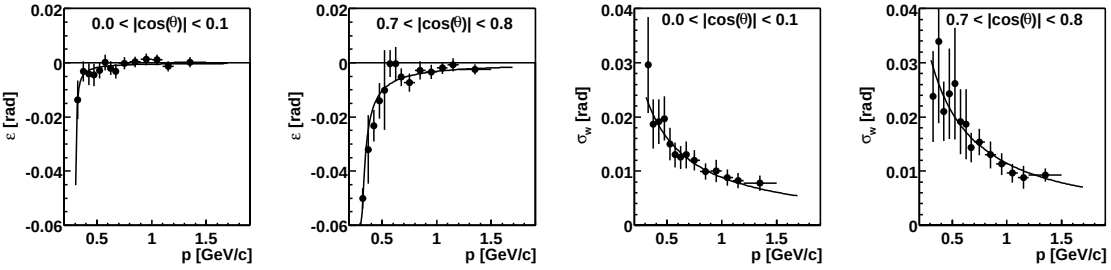

Figure 4.13: Fit results for ϵ and σ_w as defined in Eq. 4.22

4.5 DCH Based Electron Identification

Charged particles going through the Drift Chamber gas lose a small amount of their energy to ionize the gas atoms. The energy loss per unit distance, which will be called dE/dx from now on, depends on the particle mass and therefore allows the separation of electrons from muons and hadrons over a wide momentum range.

For each DCH cell hit by a track, the $(dE/dx)_{hit}$ is computed as a function of the measured charge deposition Q, geometrical path length dx and gas gain c_{Gas}:

$$\left(\frac{dE}{dx}\right)_{hit} = f_{corr}\,\frac{Q}{dx\;c_{Gas}}\;,$$

where the factor f_{corr} represents an additional correction due to charge saturation effects. For the whole DCH track, dE/dx is computed as 80% truncated mean of the individual measurements. Figure 4.14 shows the momentum dependency of this quantity for the five particle types. Based on these plots, we motivate the criterion

$$500\;a.u. < dE/dx < 1000\;a.u. \tag{4.24}$$

for preselecting electrons.

To compute the likelihood of a measurement $(dE/dx)_{meas}$ for a particle hypothesis ξ, the dE/dx distributions are assumed to be of gaussian shape centered at the expected

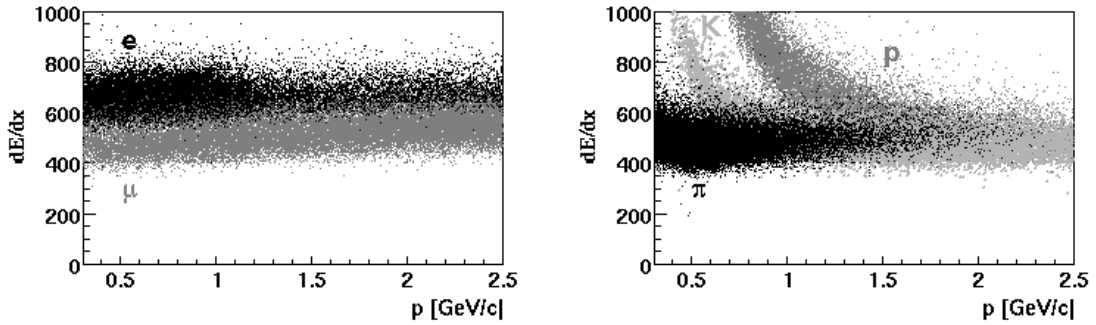

Figure 4.14: dE/dx vs. momentum for leptons (left) and hadrons (right)

value $(dE/dx)_{exp}$, which given by a 5 parameter representation of the Bethe-Bloch function:

$$(dE/dx)_{exp} = \frac{a_0}{\beta^{p_4}} \times [a_1 - \beta^{a_4} - ln(a_2 + \beta\gamma^{-a_3})] \; , \tag{4.25}$$

$$P_{DCH}(dE/dx; p, \lambda, N_{hits}, \xi) = \frac{1}{\sqrt{2\pi}\; \sigma(p, \lambda, N_{hits})} e^{-\frac{1}{2}\left(\frac{dE/dx - (dE/dx)_{exp}}{\sigma(p,\lambda,N_{hits})}\right)^2} \; . \tag{4.26}$$

The resolution σ depends on the number of hits N_{hits} contributing to the measurement and the dip angle λ, since a larger number of hits and longer path length allow a more precise determination of dE. This relationship is modeled by a 6 parameter function:

$$\sigma(p, \lambda, N_{hits}) = dE/dx \; b_0 \; \left(\frac{N_{hits}}{40}\right)^{b_1} \; \left(\frac{1}{\cos\lambda}\right)^{b_2} \; (1.0 + \frac{b_3}{p_t} + \frac{b_4}{p_t^2} + \frac{b_5}{p_t^3}) \tag{4.27}$$

4.6 Electron Identification Efficiency

For our analysis, the electron identification efficiency is measured as a function of CMS momentum and polar angle. The data are binned using the standard binning used for the later analysis of $\mathcal{B}(B \to Xl\nu)$ (see Sect. 5.2), which in the laboratory frame corresponds to five equal-size $\cos\theta$ bins in the EMC barrel between -0.72 and 0.84, and one bin for the forward EMC Endcap. The electron sample used for this measurement is acquired as described in Sect. 4.2.1. The electron identification efficiency as function of laboratory momentum for three different cuts on the likelihood fraction f_L is shown in Fig. 4.15. We observe a maximum around $p = 0.7$ GeV/c. This can be explained by the fact that at this momentum region, the response of the DIRC still contains useful information, while at the same time, the enhancement of electron-pion separation by analysis of the lateral distribution of energy deposited in the EMC is most significant. For lower momenta, the separation power of E_{dep}/p decreases, while for momenta above

1.0 GeV/c, the contribution of the DIRC to f_L gets negligible. Looking at the $\cos\theta$ dependence, we find that although the DIRC covers the EMC Barrel region only, the efficiency does not decrease in the EMC Endcap. This is due to the fact that the crystals in the Barrel Region are staggered, resulting for momenta below 0.7 GeV/c in a lower resolution of the E_{dep} measurement, which is compensated by the DIRC. A measurement of the electron identification efficiency for two different voltages of the DCH sense wires shows no significant variations(4.16). Also, as shown in Fig 4.17, the efficiency is almost identical for e^+ and e^-. For the charge asymmetry, we have

$$\frac{\epsilon(e^+) - \epsilon(e^-)}{\epsilon(e^+) + \epsilon(e^-)} \approx 1\%.$$

For a precise determination of the electron identification probability, the impact of different event topologies as given in radiative Bhabha events and $\Upsilon(4S)$ decays has to be studied. Since multihadron events show a higher multiplicity, showers in the EMC are more likely to overlap, resulting in slightly different distributions of $E_{dep}/p, LAT$ and $\Delta\Phi$. A higher occupancy of the DIRC also increases the probability of mismatched track-photon pairs, leading to Θ_c and N_γ distributions that are different for the two event categories. We also have to consider that our selection criteria for radiative Bhabha events favor tracks already matched to neutral EmcCandidates, resulting in an incorrect contribution of the track-cluster matching efficiency. The net effect of these differences is estimated by a Monte Carlo study. We define the quantities

- $\tilde{\epsilon}_{bha}$, the electron efficiency in simulated radiative Bhabha events passing the selection described in Sect. 4.2.1, and
- $\tilde{\epsilon}_{b\bar{b}}$, the electron efficiency determined in simulated $\Upsilon(4S)$ decays.

The efficiency ϵ_{bha} measured in radiative Bhabha events extracted from data is corrected for the relative change observed in the Monte Carlo simulations. The relative systematic error of this correction is assumed to be 50% of the correction (Fig. 4.18).

$$\epsilon_e = \epsilon_{bha}\,\frac{\tilde{\epsilon}_{b\bar{b}}}{\tilde{\epsilon}_{bha}}\ , \qquad \left(\frac{\Delta\epsilon_e}{\epsilon_e}\right)_{sys} = \frac{1}{2}(1 - \frac{\tilde{\epsilon}_{b\bar{b}}}{\tilde{\epsilon}_{bha}})\ . \tag{4.28}$$

4.7 Hadron Mis-Identification Probability

The probability that a hadron is misidentified as electron is derived from measurements with the control data samples described in Sect. 4.2. For pions and protons, we use the same momentum and angular bins as for electrons. Since the kaon control sample is rather small, we use larger bins, $\Delta p^* = 200\,\mathrm{MeV}/c$ for $p^* > 0.7$ GeV/c and $\Delta p^* = 500\,\mathrm{MeV}/c$ for $p^* > 1.5$ GeV/c, and four equal-size bins in $\cos\theta^*$.

Fig. 4.19 shows the pion fake rates for three cuts on f_L. We observe that the misidentification probability reaches its minimum between 0.6 and 1.0 GeV/c, which can be explained in the same way as the maximum of the electron identification efficiency. The absence of the DIRC in the EMC Endcap results in an increased fake rate. Since for $f_L = 0.6$, the fake rate is too high for our analysis of $\mathcal{B}(B \to Xe\nu)$, and for $f_L = 0.99$,

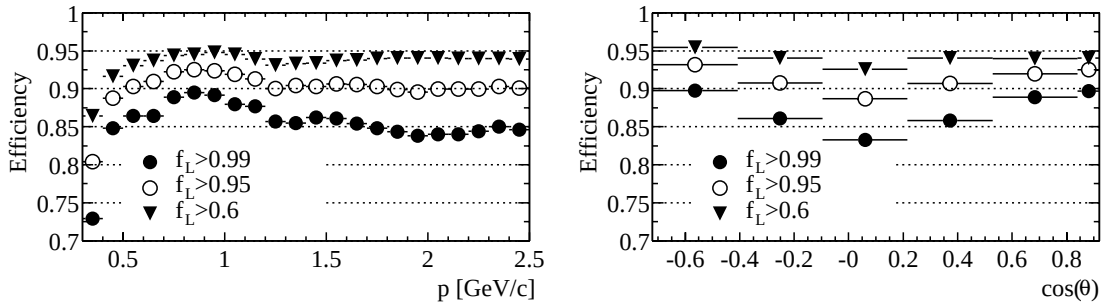

Figure 4.15: Electron identification efficiency for different cuts on likelihood fraction. We observe a maximum between 0.5 and 1.5 GeV/c.

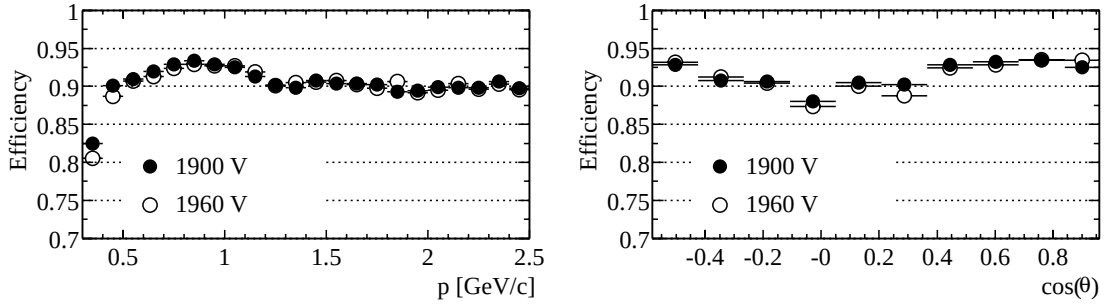

Figure 4.16: Electron identification efficiency for different voltages of the DCH sense wires.

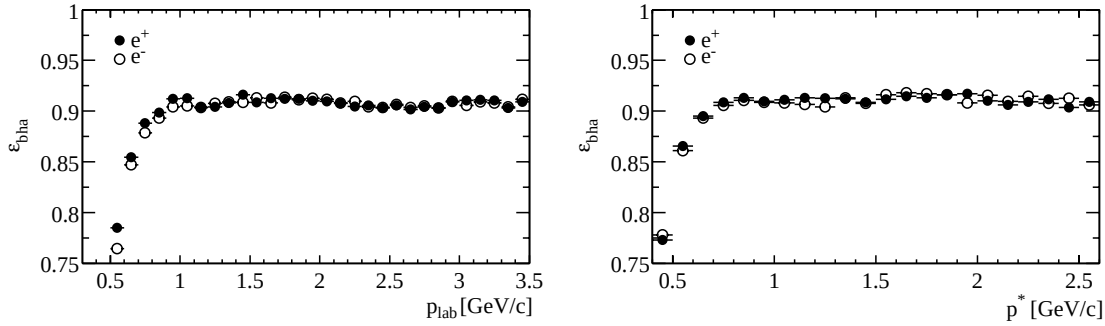

Figure 4.17: Charge dependence of electron identification efficiency in radiative Bhabha events extracted from data.

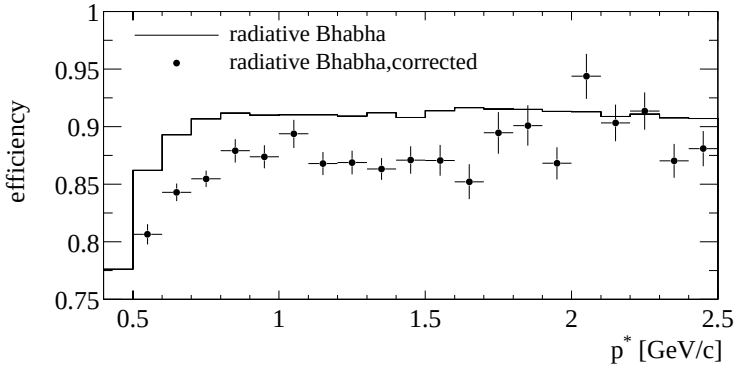

Figure 4.18: Electron identification efficiency before (line) and after (points) correction for event topology.

the electron identification efficiency is too low, we choose $f_L = 0.95$. Fig. 4.20 shows that by changing the voltage of the DCH sense wires, the pion fake rate is reduced.
Since combinatorial background results in contaminations of the samples, a background subtraction based on the sidebands in effective mass distributions is performed (see Table 4.4), assuming that the background distributions can be described by a linear function. As an estimate for the systematic error on the fake rate we use half the difference between the results obtained with and without sideband subtraction. Figure 4.21 shows the resulting hadron fake rates averaged over the polar angle.

Process	Signal Region	Sideband Region
$K_s^0 \to \pi^+\pi^-$	$0.488 < m_{K_s^0} < 0.508$	$0.46 < m_{K_s^0} < 0.48$ $0.52 < m_{K_s^0} < 0.54$
$D^* \to \pi D^0,\ D^0 \to K\pi$	$0.14445 < \Delta m < 0.14645$ $1.845 < m_{D^0} < 1.88$	$1.785 < m_{D^0} < 1.82$ $1.9 < m_{D^0} < 1.935$
$\Lambda \to \pi p$	$1.113 < m_\Lambda < 1.119$	$1.104 < m_\Lambda < 1.110$ $1.122 < m_\Lambda < 1.128$

Table 4.4: Signal and sideband cuts for the selection of hadron control samples, all masses are indicated in GeV/c^2.

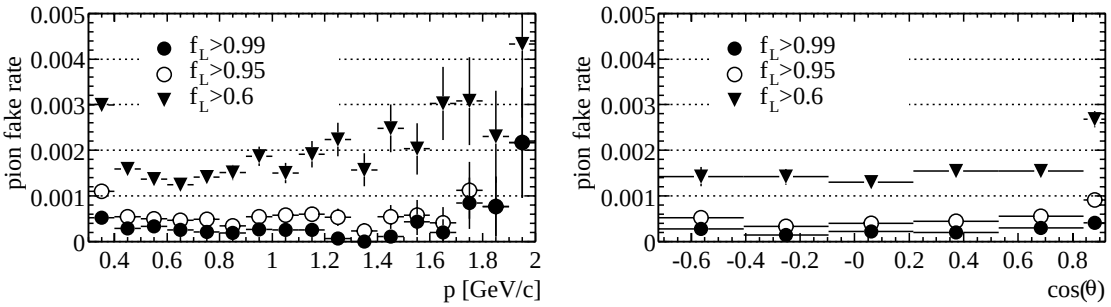

Figure 4.19: Pion mis-identification probability for different cuts on likelihood fraction.

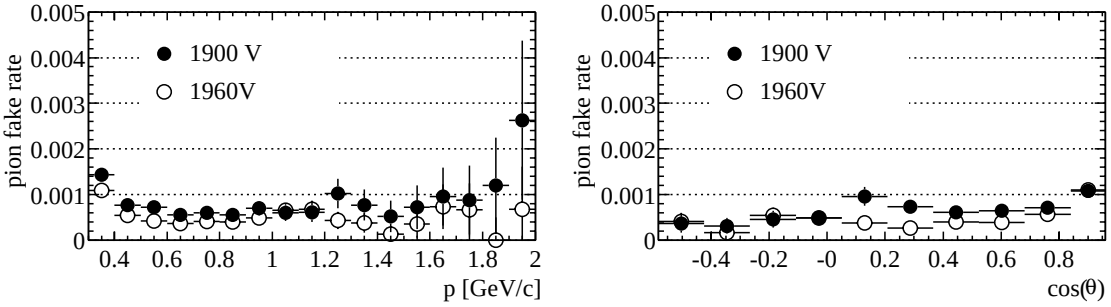

Figure 4.20: Pion mis-identification probability for different voltages of the DCH sense wires.

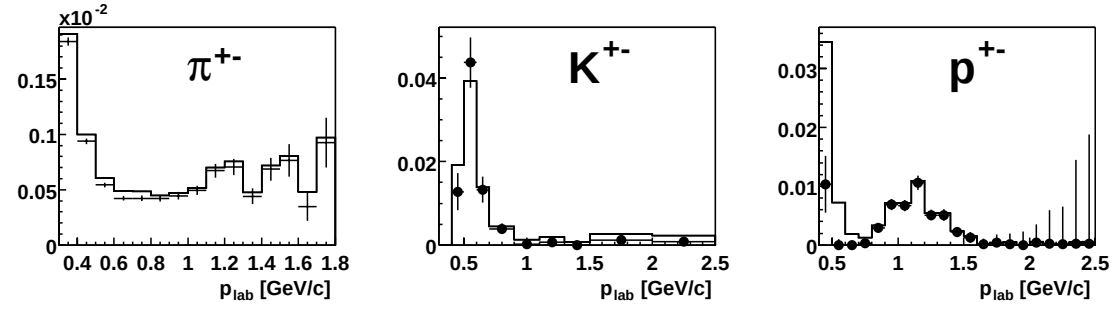

Figure 4.21: Hadron fake rates per track derived from control samples with (data points) and without (histograms) sideband subtraction.

Chapter 5

Principle of the Analysis

5.1 Idea

Since high momentum leptons originate predominantly from a semileptonic decay of one of the two B mesons produced in $\Upsilon(4S)$ decays, it is the idea of this analysis to use such a high momentum lepton (CMS momentum above 1.4 GeV/c) to tag a $B\overline{B}$ event. The B meson which is the origin of this lepton will be called *tagged* B from now on, while we refer to the other B meson as *signal* or *"other"* B. The observation of a second lepton in these tagged events can be traced to either a semileptonic decay of the other B meson or the semileptonic decay of a charm particle produced in the decay of either of the two B mesons. It is the goal of this analysis to use lepton tags to separate the spectra of

- primary (or prompt) electrons from semileptonic decays of B mesons (average of charged and neutral), $B \to X_c e^+ \nu$, and
- secondary (or cascade) electrons from semileptonic decays of charmed hadrons (average of charged and neutral) from the decay chain $B \to X_{\overline{c}} \to Y e^- \overline{\nu}$.

The combination of primary and secondary leptons which contribute to the yield of dilepton events is presented in Table 5.1. Here the first sign listed refers to the charge of the tag lepton, the second sign indicates the charge of the second lepton, in our case an electron. We refer to this second electron as the *signal electron*. The relative production of charged and neutral B mesons is indicated by the probabilities f_0 and f_+. χ_0 has been defined in Eq. 2.3 and refers to the rate of flavor mixing in neutral B mesons as described in Sect. 2.2.1.
The total electron spectrum can be decomposed into

1. primary electrons from the signal B meson (Fig. 5.1a) ,
2. secondary electrons from the tagged B meson (Fig. 5.1c) ,
3. secondary electrons from the signal B meson (Fig. 5.1b,d,e,f) , and
4. electrons from other background sources like misidentified hadrons, J/ψ decays, photon conversions or π^0/η^0 Dalitz decays.

Without $B^0\overline{B}^0$ mixing, electrons of the first two categories can be found in oppositely charged tag-signal pairs ("unlike-sign") only, while secondary electrons from the signal

Tagged B	Signal B	Probability	primary other B	secondary other B	secondary tagged B
B^+	B^-	$f_+/2$	t^+e^-	t^+e^+	t^+e^-
B^-	B^+	$f_+/2$	t^-e^+	t^-e^-	t^-e^+
B^0	$\overline{B}^0$	$f_0(1-\chi_0)/2$	t^+e^-	t^+e^+	t^+e^-
$\overline{B}^0$	B^0	$f_0(1-\chi_0)/2$	t^-e^+	t^-e^-	t^-e^+
B^0	B^0	$f_0\chi_0/2$	t^+e^+	t^+e^-	t^+e^-
$\overline{B}^0$	$\overline{B}^0$	$f_0\chi_0/2$	t^-e^-	t^-e^+	t^-e^+

Table 5.1: Charge correlation between the two leptons, the tagging lepton ("t") and the signal electron ("e"), in $\Upsilon(4S)$ decays.

B meson predominantly produce equally charged ("like-sign") pairs. Exceptions are processes involving $c\bar{c}s$ production or cascades containing $\tau \to e\ \nu_e\ \bar{\nu}_\tau$ decays. Ignoring these exceptions for now, and assuming that we already corrected for contributions from the fourth category, the signal electron spectra in tagged events can be expressed separately for like-sign and opposite-sign tag-signal pairs:

$$\frac{dN(t^\pm e^\mp)}{dp^*} = \varepsilon\ \epsilon_{evt}\ T_\ell \left[\frac{d\mathcal{B}_b}{dp^*}(1-f_0\chi_0) + \frac{d\mathcal{B}_c}{dp^*}f_0\chi_0 + (\frac{d\mathcal{B}_c}{dp^*})_{same}\right] \tag{5.1}$$

$$\frac{dN(t^\pm e^\pm)}{dp^*} = \varepsilon\ \epsilon_{evt}\ T_\ell \left[\frac{d\mathcal{B}_b}{dp^*}f_0\chi_0 + \frac{d\mathcal{B}_c}{dp^*}(1-f_0\chi_0)\right]. \tag{5.2}$$

Here we denote $\mathcal{B}_b = \mathcal{B}(B \to X_c e^+ \nu)$ and $\mathcal{B}_c = \mathcal{B}(B \to \overline{D} \to Y_s e^- \overline{\nu})$. The efficiency for detecting a second electron in a tagged event, $\varepsilon = \varepsilon(p^*, \theta^*)$, is a function of the CMS momentum, polar angle and the charge of the lepton as derived in Sect. 4.6. T_l is the number of found tags, which needs to be multiplied by the relative selection efficiency ϵ_{evt} of dilepton w.r.t. single lepton events. The probability of $B^0\overline{B}^0$ mixing has been derived from measurements of Δm_d at LEP and direct measurements at the $\Upsilon(4S)$ by CLEO and ARGUS. For this analysis, we use the world average [33]

$$\chi_0 = 0.174 \pm 0.009$$

The $\Upsilon(4S)$ decays roughly equally into charged and neutral B mesons pairs. CLEO has measured the ratio of the charged to neutral $\Upsilon(4S)$ decays using exclusive $B \to J/\psi\, K^{(*)}$ decays. Assuming isospin invariance and $\tau_{B^+}/\tau_{B^0} = 1.066 \pm 0.024$, they found $f_+/f_0 = 1.044 \pm 0.069^{+0.043}_{-0.045}$. This is consistent with equal production and we will assume $f_0 = f_+ = 0.5 \pm 0.02$. Thus, the fraction of mixed events in the tagged sample is rather small, $f_0\chi_0 = 8.7\%$.

The third term in Eq. 5.1 accounts for secondary decays of the tagged B meson. This is a sizable contribution, which can be kinematically isolated from other secondary decays. Figure 5.2 shows the MC prediction for the correlation between the opening angle α of the two oppositely charged leptons and the momentum of the signal electron, separately for events in which the signal lepton originates from the other or same B

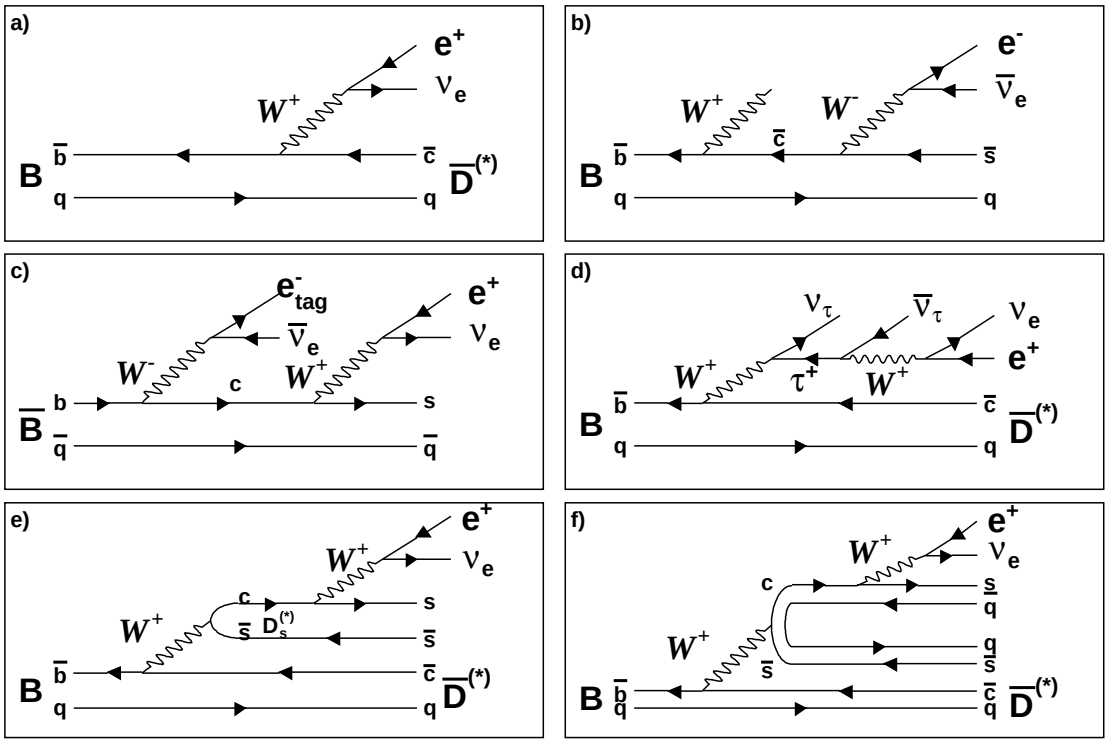

Figure 5.1: Feynman diagrams for physics processes contributing to the electron yield. In all pictures, the tagged B-meson is a $\overline{B}$, and the tag lepton is an e^- : a) Prompt electron from signal B, b) like-sign secondary electron from signal B, c) secondary electron from tagged B , d) unlike-sign electron from τ cascade of signal B, e) unlike-sign electron from D_s cascade of signal B, f) unlike-sign electron from $B \to D^{(*)}\overline{D}^{(*)}K$ cascade of signal B.

meson as the tag lepton. If the electron originates from the same B, it is from a cascade D decay, if it originates from the other B, it is mostly from a prompt B decay. Since in the rest frame of the $\Upsilon(4S)$ the B and $\overline{B}$ are produced nearly at rest, there is very little correlation between the decay products of different B mesons. On the other hand, secondary leptons originating from the same B meson as the tag lepton are correlated with the tag lepton, they tend to be emitted in opposite directions and have lower momenta. The strength of the back-to-back correlation depends on the momentum of the signal electron.

By applying a momentum dependent cut on the angle between tag and signal electron, this secondary decay contribution can be suppressed to a very low level, while retaining most of the primary (and secondary mixed) decays from the other B meson. After the removal of the remaining background from secondary decays of the tagged B meson, both of the equations above have two terms which differ by the a known relative fraction. Thus, one can derive the primary and secondary lepton spectra directly from the observed mixture in like-sign and unlike-sign pairs.

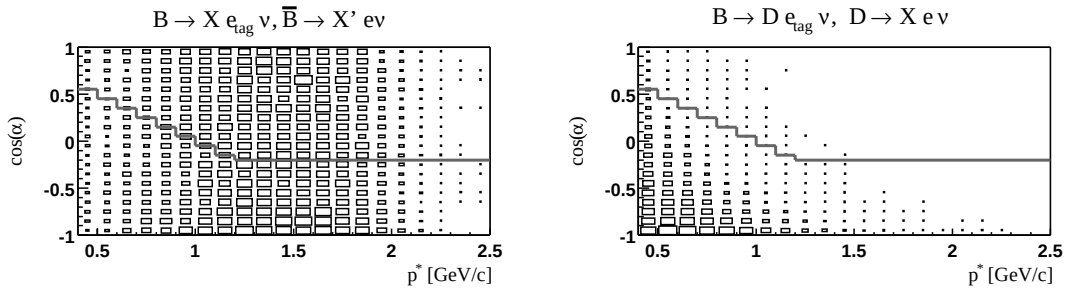

Figure 5.2: MC: momentum of the electron vs. the opening angle between the signal electron and the tag lepton in events with oppositely charged leptons a) for electrons (direct) from the other B, and b) for electrons from a cascade charm decay of the tagged B. The lines illustrate the cut used in this analysis to suppress these same side cascade electrons (see Sect. 6.1.4 for details).

5.2 Analysis Procedure

For each event, two sets of candidates (which are called *lists* in the *BABAR* framework) are created:

- the "tag" list of identified electrons with 1.4 GeV/c $< p^* <$ 2.3 GeV/c which have not been classified as being part of a photon conversion, Dalitz decay (see Sect. 6.3.1 for the detailed algorithms) or J/ψ decay; and
- the "signal" list of all identified electrons with $p^* > 0.5$ GeV/c.

The tag and signal electrons are accumulated in two-dimensional histograms as a function of p^* and $\cos\theta^*$. For a given event, each candidate in the tag list is associated with each candidate from the signal list to form a *dilepton* pair (if a track appears in both lists, we make sure that it is not paired with itself). In particular, if an event contains more than one tag electron, multiple tag-signal pairs are formed.

Depending on the relative charge w.r.t the tag lepton, the signal leptons are separated into two 2-dimensional histograms, one for like-sign and the other for unlike-sign pairs, each with 100 MeV/c bins in p^* and six bins in $\cos\theta^*$:

$$\cos(\theta_i^*) \in \{-0.72,\ -0.4,\ -0.096,\ 0.216,\ 0.528,\ 0.84,\ 0.92\}\ .$$

This will be referred to as the *standard binning*. For the suppression of the unwanted secondary electrons, we only retain unlike-sign signal-tag pairs which pass a cut on the opening angle α to the tag lepton. As sketched in Fig. 5.2, this cut is constant within each momentum bin in order simplify the computation of its efficiency, which in this case can be determined from geometrical considerations only. The set of signal candidates from oppositely charged pairs passing the opening angle cut will be called "unlike-sign sample" from now on.

At this stage, a tracking efficiency correction is applied by weighting each signal electron by the inverse efficiency taken from tables provided by the *BABAR* tracking efficiency task force [31], which contain the tracking efficiencies as a function of p_{lab},

θ, ϕ, and charged particle multiplicity. After accumulating all events in the sample, we extract the spectra of tag-electrons, like-sign and unlike-sign electrons. These histograms are the basis for further studies and background corrections.

The dominant background in the tag spectrum are high momentum electrons from semileptonic D decays, which we will refer to as *secondary tags*. Another sizable contribution arises from $J/\psi \rightarrow e^+e^-$ decays, most of which are removed by a cut on the effective mass of the lepton pair. This J/ψ veto also removes a sizable number of true tag leptons, a loss which we need to correct for (Sect. 6.2).

The dominant backgrounds for the signal spectra occur at the lower end of the spectrum, electrons from photon conversions and Dalitz pairs as well as hadrons that are misidentified as electrons. These background spectra are estimated in terms of p^* and $\cos\theta^*$, separately for like-sign and unlike-sign samples, and then subtracted from the two-dimensional signal histograms. Although most secondary electrons originating from the tagged B meson are removed by the opening angle cut, the remaining tracks form the dominant background in the unlike-sign sample. Assuming that all other backgrounds show an almost flat distribution in $\cos\alpha$, we base our estimation of this contribution on the non-flatness of the $\cos\alpha$ distribution obtained by accumulating all opposite-sign pairs, regardless of their opening angle. This is done below 1.2 GeV/c and in bins of 100 MeV/c, while at higher momenta this background is only small and is determined with the help of the Monte Carlo simulation.

Next, the spectra are corrected for the electron identification efficiency using efficiency tables produced in the *standard binning*. From these corrected signal spectra we then subtract the contributions from various other physics processes. These background spectra are obtained by performing the standard event and lepton selection on simulated $\Upsilon(4S)$ samples, using a map matching the generated particles to the reconstructed objects (like tracks and EmcClusters) to identify electrons.

After all corrections have been performed, the spectra of primary and secondary electrons are derived from the corrected like-sign and unlike-sign spectra. The ratio of the integral of the spectrum of primary electrons and the total (background corrected) number of tag electrons measures the visible semileptonic branching fraction.

Chapter 6

Determination of the Electron Spectrum

6.1 Event and Track Selection Cuts

6.1.1 Data Sample

This analysis is based on data recorded in the second half of the year 2000, corresponding to 4.13 fb^{-1} collected at the $\Upsilon(4S)$ resonance and 0.965 fb^{-1} recorded at an CMS energy approximately 40 MeV below the resonance ("off resonance"). Table 6.1 gives an overview over the data samples selected for this analysis. The software release used for event reconstruction is identical in all data sets, which also share a common voltage of the Drift Chamber sense wires (1960 V). Of all data taken in the year 2000, the block used for this analysis is the largest which such stable conditions.

Dataset	Run Range	$\mathcal{L}(\text{pb}^{-1})$
2000-b2-s3-r8D-on5	15237 - 15713	1723
2000-b2-s3-r8D-on6	15826 - 16517	2411
2000-b2-s3-r8D-off5	15720 - 15825	550
2000-b2-s3-r8D-off6	16523 - 16570	415
Total on resonance		4134
Total off resonance		965

Table 6.1: Summary of the data used in this analysis.

The off resonance data are used to estimate the shape and amount of the contribution from non-resonant processes at the $\Upsilon(4S)$ resonance. The relative normalization of the two data sets is

$$\xi_{\mathcal{L}} = \frac{s_{off}}{s_{on}} \frac{\int \mathcal{L}_{on} dt}{\int \mathcal{L}_{off} dt} = 4.25 \pm 0.007 \pm 0.021,$$

where s and $\mathcal{L}$ are the CMS energy squared and the luminosity of the data sets. The statistical uncertainty is given by the number of detected $\mu^+\mu^-$ pairs used for the determination of $\mathcal{L}$, the systematic error is estimated to be 0.5%, limited by variations in the detector conditions over time. To account for the difference in the beam ener-

gies, the measured lepton momenta in the off resonance data are scaled by a factor of $10.58/10.54 = 1.0038$.

For Monte Carlo studies, we use approximately 5 million generic $B^0\overline{B^0}$ and B^+B^- events which have been produced using the full detector simulation BBSIM. The simulated detector and background conditions (for example the voltage of the DCH sense wires) correspond to the actual conditions given during the time period covered by this analysis.

6.1.2 Track Selection Cuts

To pass the *GoodTracksLoose* selection defined at *BABAR*, a track has to fulfill the following requirements:

- $N_{DCH} \geq 12$, where N_{DCH} is the number of Drift Chamber Cells which registered a signal ("DCH hits") associated to the track;
- $d_{xy} < 1.5\,\mathrm{cm}$, where d_{xy} is the distance of closest approach to the primary vertex in the xy plane; and
- $d_z < 3\,\mathrm{cm}$, where d_z refers to the distance of closest approach to the primary vertex in the z direction.

The first criterion ensures a reliable momentum measurement (12 hits $\approx$ 3 space points), while the cuts on the impact parameters discriminate against tracks not originating from beam-beam interactions. For this analysis, we tighten the cut on the transverse distance to $d_{xy} < 0.25\,\mathrm{cm}$. This change is motivated by Monte Carlo studies which predict a reduction of the photon conversion background by 40%, while the loss of signal electrons is small ($\approx 1\%$). Since the contribution of this background to the total spectrum increases sharply at lower momenta, we restrict this analysis to electron momenta $p^* > 0.5\,\mathrm{GeV}/c$. Since the electron identification relies on the shower measurement in the EMC, we also restrict the solid angle as listed in Table 6.2.

Track quality	$N_{DCH} \geq 12$ in drift chamber
Impact parameter	$d_{xy} < 0.25\,\mathrm{cm}$, $d_z < 3\,\mathrm{cm}$
Momentum	$p^* > 0.5\,\mathrm{GeV}/c$
Polar angle	$-0.72 < \cos\theta < 0.92$
Likelihood fraction (see Eq. 4.2)	$f_L > 0.95$

Table 6.2: Electron track selection cuts.

The probability of finding a track satisfying the *GoodTracksLoose* criteria has been determined by the *BABAR* tracking efficiency task force [31]. This efficiency is based on the fraction of SVT tracks that are matched to tracks in the DCH. This number is then corrected for mismatches between found DCH and SVT tracks, SVT ghost tracks and the fact that the DCH and SVT tracking algorithms are not completely independent of each other. The result of this analysis is the track finding efficiency for tracks satisfying the *GoodTracksLoose* criterion as a function of momentum, the angles θ and ϕ, and charged multiplicity. The dependence on the charged multiplicity is due to a less efficient pattern recognition in high occupancy events. As stated in the introduction, the correction for

this efficiency is applied immediately after the track is identified as electron by giving it the appropriate weight. The stated systematic uncertainty is 0.7%.

Since the electron track selection for this analysis requires a smaller d_{xy}, a lower tracking efficiency for signal candidates is expected, primarily due to bremsstrahlung in the first layers of the SVT, resulting in an increased curvature and therefore a larger value of d_{xy} when being extrapolated back to the origin. The study of this additional loss is based on kinematically selected $\tau^+\tau^-$ pairs with 3-1 track topology provided by the *BABAR* working group on τ decays [28]. To enhance the purity of this sample, we require that the tracks on the 3-prong side originate from a single vertex and that none of them are electrons (by demanding $E_{dep}/p < 0.7$). Applying the electron identification cuts described in Sect. 4.1 on the 1-prong side delivers a pure sample of electron tracks originating very close to the primary vertex. Of these tracks, the fraction that passes the $d_{xy} < 0.25\,\mathrm{cm}$ requirement is used as an estimate of the efficiency loss caused by the tighter cut on d_{xy} and serves as a correction to the standard tracking efficiencies.

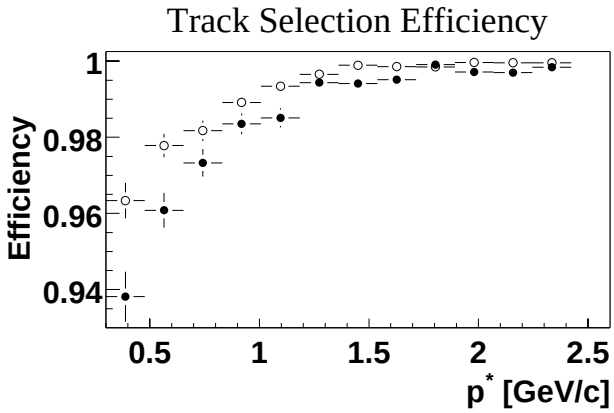

Figure 6.1: Fraction of good tracks (according to the *GoodTracksLoose* criterion) satisfying $d_{xy} < 0.25\,\mathrm{cm}$, derived from data (solid circles) and MC (open circles).

Figure 6.1 shows these relative efficiencies derived from a study of data and a full detector simulation based on generic $\tau^+\tau^-$ events. The difference can be attributed to an overestimate of the resolution in the Monte Carlo simulation and additional background electrons not originating near the beam interaction point (beam-gas interactions and conversions). As a correction for this loss, we use the average of the MC prediction and the data measurement, taking half the difference as an additional systematic error. As we will see in Section 7.1, this relative efficiency (i.e. the probability of a "*GoodTrackLoose*" passing $d_{xy} < 0.25\,\mathrm{cm}$) is $\epsilon_{doca} = (99.2 \pm 0.3_{(sys)})$ % when applied to our final spectrum between 0.5 and 2.5 GeV/c .

6.1.3 Event Selection Cuts

The dominant source of non-$B\overline{B}$ events containing a high momentum electron are

- non-resonant hadron production, $q\overline{q}$, primarily semileptonic decays in $c\overline{c}$ events;

- QED processes like lepton pair production, e^+e^-, $\tau^+\tau^-$, and $\gamma\gamma$, dominated by multi-prong Bhabha events;
- interactions of beam particles in the residual gas, the beam pipe or beam line components.

Most of these backgrounds are events with low charged multiplicity, $q\overline{q}$ and QED pair production result in events with jet-like topology. We use the following cuts to suppress these backgrounds:

1. $R_2 < 0.6$, where $R_2 = H_2/H_0$ is the ratio of the Fox-Wolfram moments calculated from all charged tracks (including those found by the SVT only) in the event;
2. $N_{gtl} \geq 4$ and $N_{tot} \geq 5$, where N_{gtl} corresponds to the number of found tracks satisfying the *GoodTrackLoose* criterion. The total multiplicity is defined as $N_{tot} = N_{gtl} + N_{neut}/2$, where N_{neut} refers to the number of neutral EmcCandidates with a deposited energy of $E_{neut} > 80\,\mathrm{MeV}$. A pair of tracks that is identified as converted photon (see Sect. 6.3.1) is counted as a neutral particle (and reduces N_{gtl} by two).
3. At least one electron with a CMS momentum between 1.4 and 2.3 GeV/c.

The addition of the total multiplicity cut reduces the background from radiative Bhabha events by a factor of 20, while it decreases the event selection efficiency by 2.2 %.

Events with a single high momentum lepton from a semileptonic B decay differ from dilepton events with two semileptonic B decays: they have on average a higher multiplicity (see Figure 6.2a) and the angular distribution of the particles is more isotropic, resulting in a slightly different R_2 distribution (see Figure 6.2b). These discrepancies lead to different selection efficiencies for single and dilepton events, which have to be taken into account in the determination of the branching ratio. Table 6.3 shows the selection efficiencies derived from Monte Carlo simulation. As noted in Eq. 5.1, the number of detected tag-signal pairs has to be divided by the ratio

$$\epsilon_{evt} = \epsilon_{dilep}/\epsilon_{single}.$$

The relative systematic error of this correction is estimated to be 25%, i.e.

$$\epsilon_{evt} = (98.00 \pm 0.15_{(stat)} \pm 0.5_{(sys)})\% \ .$$

Cut	$\epsilon_{single}(\%)$	$\epsilon_{dilep}(\%)$
$R2 < 0.6$	98.59 ($\pm$ 0.019)	97.90 ($\pm$ 0.085)
$N_{gtl} \geq 4$	96.61 ($\pm$ 0.029)	95.60 ($\pm$ 0.122)
$N_{tot} \geq 5$	99.92 ($\pm$ 0.004)	99.35($\pm$ 0.048)
combined	95.39 ($\pm$ 0.033)	93.49 ($\pm$ 0.147)

Table 6.3: Event selection efficiencies for events with at least one tag electron (ϵ_{single}) and additional signal electron (ϵ_{dilep}) ; the errors are statistical only.

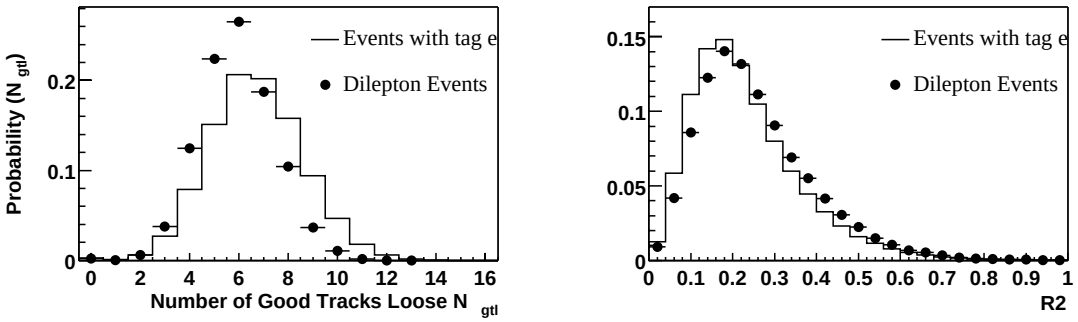

Figure 6.2: MC distributions of a) number of *GoodTracksLoose* and b) R_2 in single-tag and dilepton events. These distributions are normalized to the total number of entries.

6.1.4 Signal Electron Selection

For each selected tag candidate, we search the event for other identified electrons with a CMS momentum above 0.5 GeV/c. As explained in Chapter 5, opposite-sign signal candidates contain secondary electrons from cascade decays of the tagged B, which can be removed by an appropriate cut on the angle α between tag and signal candidate. With p_e^* being the CMS momentum of the signal electron, we choose

$$\cos\alpha > -0.2 \quad \text{and} \quad \cos\alpha + \hat{\mathrm{p}}_\mathrm{e}^* \,/\, (\,\mathrm{GeV/c}) \; > 1.0 \;, \tag{6.1}$$

where $\hat{p}_e^*$ is the center of the p^*-bin assigned to p_e^* . Only signal candidates satisfying this cut on the opening angle are meant when referring to the unlike-sign sample in the following sections.

Assuming a flat distribution of $\cos\alpha$ for direct electrons at all momenta, the loss in efficiency due to the requirement described in Eq. 6.1 can be calculated as reduction in geometrical acceptance. With α_{max} being the maximal value of α allowed by Eq. 6.1, we have

$$\varepsilon_{oa} = (1-\cos\alpha_{max})/2 = \begin{cases} \hat{p}_e^*/2 & \text{for } p_e^* < 1.2\,\mathrm{GeV}/c \\ 0.6 & \text{for } p_e^* \geq 1.2\,\mathrm{GeV}/c \end{cases} \quad . \tag{6.2}$$

Figure 6.3 shows the comparison between the acceptance calculated according to Eq. 6.2 and the efficiency derived from Monte Carlo simulation. The two estimates agree within their statistical errors.

Figure 6.4 illustrates the impact of the opening angle cut on three different background contributions. The requirement $\cos\alpha > -0.2$ removes practically all tag-signal pairs from $J/\psi \to e^+e^-$ decays.

6.1.5 Tag Electron Selection

In order to be considered as tag, a track must be identified as an electron and its CMS momentum must be between 1.4 GeV/c and 2.3 GeV/c. Tracks which are part of a photon conversion or Dalitz pair, based on the algorithm described in Section 6.3.1, are rejected.

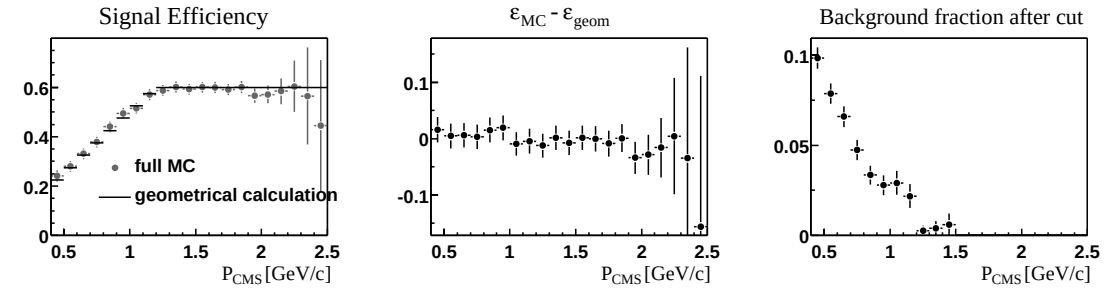

Figure 6.3: MC: cut on the opening angle for unlike-sign pairs as a function of the CMS momentum of the second lepton: a) efficiency estimate derived from full simulation and the calculated geometrical acceptance; b) difference between the calculated and the MC derived efficiency; c) the fraction of cascade background leptons passing the opening angle cut.

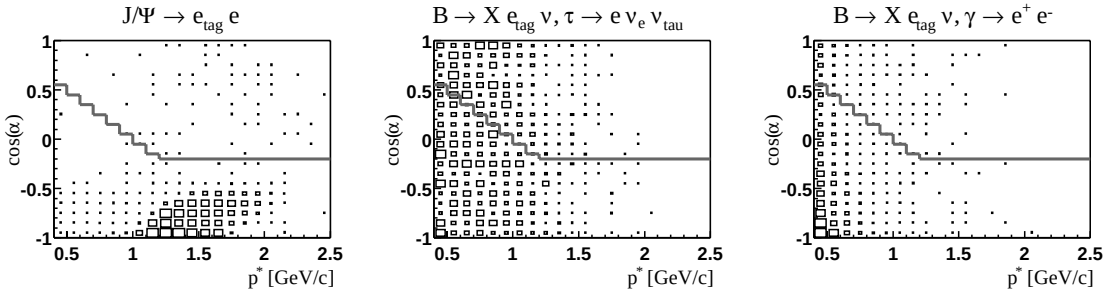

Figure 6.4: MC: the opening angle between the tag lepton and a signal electron as a function of the CMS momentum for electrons from a) $J/\psi \to e^+_{tag} e^-$, b) $\tau \to e^- \nu_e \nu_\tau$, and c) $\gamma \to e^+ e^-$.

We also apply a veto against $J/\psi \to e^+e^-$ decays by pairing each tag electron candidate with all other oppositely charged tracks satisfying the standard *tight* electron selection criteria [38]. If any pair satisfies the condition

$$2.9\,\mathrm{GeV}/c^2 < m(e^+e^-) < 3.15\,\mathrm{GeV}/c^2 \qquad \text{and} \qquad \cos\alpha < -0.2 \tag{6.3}$$

the candidate is rejected as tag. The upper limit on $\cos\alpha$ ensures that no true tag-signal pair satisfying Eq. 6.1 and accidently forming and invariant mass between $2.9\,\mathrm{GeV}/c^2$ and $3.15\,\mathrm{GeV}/c^2$ is rejected.

6.2 Spectrum and Number of Tag Leptons

With the selection criteria explained in Sect. 6.1.5, the spectrum of tag electrons is extracted from on and off resonance data. In case of multiple tracks satisfying these requirements, each contributes to the total number of tag electrons. Figure 6.5 shows

the spectra before and after continuum subtraction. To check the relative normalization of on and off data, we examine the tag electron spectrum between 2.8 GeV/c and 3.5 GeV/c, *i.e.* beyond the kinematic endpoint for B decays. We observe an excess of 88 $\pm$ 199 electrons, a yield that is consistent with zero.

In the standard CMS momentum interval of $1.4\,\mathrm{GeV}/c < p_e^* < 2.3\,\mathrm{GeV}/c$, the number of tracks identified as tag lepton is 313718 $\pm$ 863 , with a systematic uncertainty of $\pm$ 410 (assuming a systematic error of 0.5% in $\xi_{\mathcal{L}}$). Performing the analysis on MC simulated events yields 315764 $\pm$ 534 tag electrons, normalized to the same number of B mesons, which is a remarkably good agreement.

We estimate the background in the sample of tag leptons from Monte Carlo simulations. For conversions and Dalitz decays we assume a relative systematic uncertainty of 25%, while the systematic errors on all other background contributions are the same as for the signal electrons (Table 6.14 in Sect. 6.3.5).

Finally, we have to correct for the number of primary tag electrons which have been removed by the J/ψ veto cut

$$2.9\,\mathrm{GeV}/c^2 < \; m(e^+e^-) \; < 3.15\,\mathrm{GeV}/c^2 \qquad \text{and} \qquad \cos\alpha < -0.2\ .$$

Due to the restriction on $\cos\alpha$, this selection does not remove tag-signal pairs from the unlike-sign sample, only pairs which do not pass the cascade suppression cut and therefore contribute to the number of tag electrons only are affected. To estimate the number of these pairs, we fit the invariant mass distribution to a sum of the "Crystal Ball" function and a first order polynomial. We obtain an estimate of the non-resonant background by integrating the contribution of the first order polynomial between $2.9\,\mathrm{GeV}/c^2$ and $3.15\,\mathrm{GeV}/c^2$. MC studies show that in this mass region 90% of the leptons contributing to this background originate from prompt B decays, i.e. are true tags. Figure 6.6 shows the invariant mass distributions for pairs involving true tag leptons and for for pairs from J/ψ decays. The background is well described by a 1st order polynomial. The invariant mass distribution from J/ψ decays is well reproduced by the "Crystal Ball" function

$$f(x) = \begin{cases} p_0\ e^{-\frac{1}{2}\left(\frac{x-x0}{\sigma}\right)^2} & \text{for} \quad x > x_0 - p_1\sigma \\ p_0\ e^{-\frac{1}{2}p_1^2}\left(\frac{p_2\,\sigma}{p_1}\right)^{p_2} \frac{1}{(x_0 - x - \sigma p_1 + \sigma\ p_2/p_1)^{p_2}} & \text{for} \quad x < x_0 - p_1\sigma \end{cases}\ , \tag{6.4}$$

with x_0, σ, p_0, p_1 and p_2 as fit parameters. Figure 6.7 shows the fit to the data. The number of non-J/ψ background pairs derived from this fit is 2706 $\pm$ 170. Assuming that $(90\ \pm 5_{(sys)})$% of these pairs contain a true tag lepton, this results in an overall correction of $2435 \pm 212_{(sys)}$ tracks to the tag lepton sample. Table 6.4 summarizes all background corrections leading to the final number of $304051 \pm 807_{(stat)} \pm 1960_{(sys)}$ tags.

6.3 Background and Efficiency Correction

6.3.1 Photon Conversions and Dalitz Decays

Electrons from photon conversions, π^0 and η^0 Dalitz decays contribute significantly to the lower part of the momentum spectrum. e^+e^- pairs are identified by requiring two oppositely charged tracks which originate from a common vertex and have an invariant

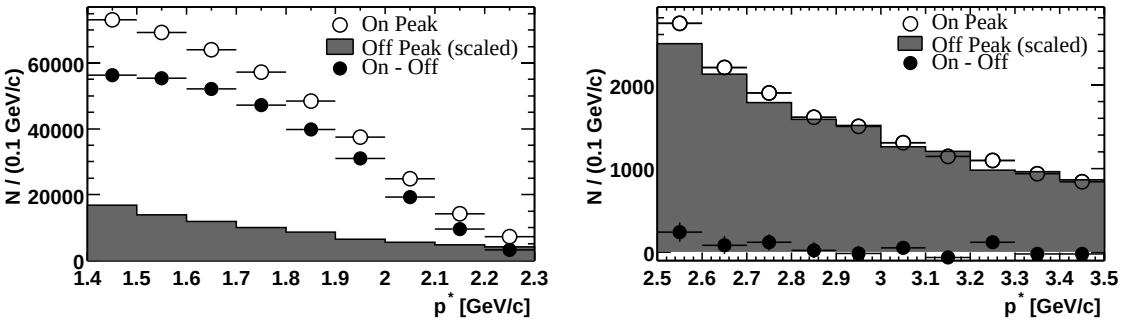

Figure 6.5: The CMS momentum spectrum for tag electrons, derived from on and off resonance data, for two momentum intervals.

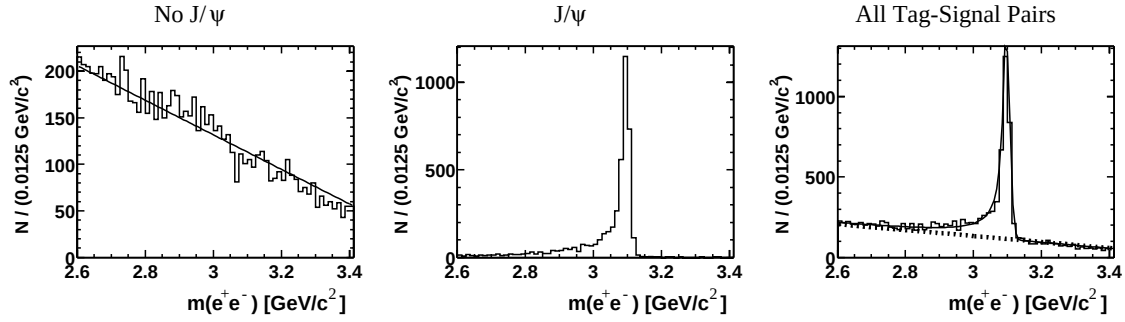

Figure 6.6: MC: invariant mass distributions for lepton pairs; left: non J/ψ pairs ; center: J/ψ decays ; right: the sum of resonant and non-resonant contributions.

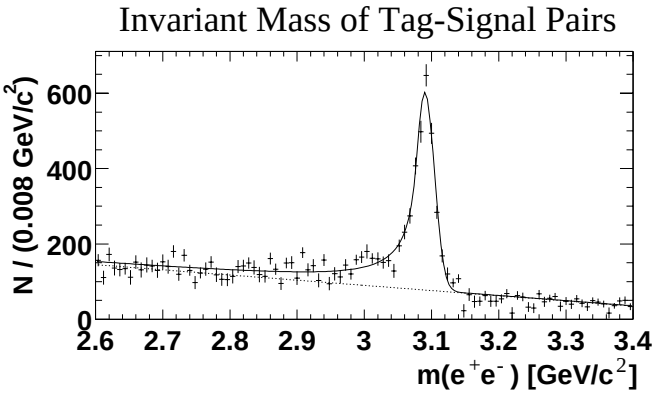

Figure 6.7: Fit to invariant mass distribution of opposite sign dilepton pairs.

mass below a certain threshold. The vertexing procedure is illustrated in Figure 6.8. Table 6.5 summarizes the criteria applied to identify electron pairs from photon conversions

	N	$(\Delta N/N)_{sys}$
Tags in ON resonance data	395791	
$\xi_{\mathcal{L}}\times$ Tags in OFF resonance data	82073	0.005
Total Number of tags	313718 $(\pm\ 863)_{stat}\ (\pm\ 410)_{sys}$	0.001
Secondary tags	7425	0.25
Unvetoed e from J/*psi*	1925	0.06
Vetoed True Tags	(-) 2435	0.09
Faked Hadrons	1455	0.25
Unvetoed e from γ or π^0	653	0.25
e from cascade τ	446	0.1
e from D_s	148	0.45
Other	50	1.0
Corrected Number of tags	304051 $(\pm\ 870)_{stat}\ (\pm\ 1960)_{sys}$	0.01

Table 6.4: Background to tag leptons

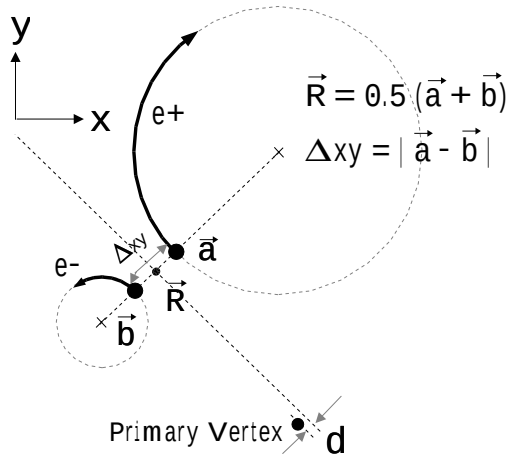

Figure 6.8: Illustration of the conversion pair finder algorithm.

and Dalitz decays.

The points of closest approach in the xy plane of the two helices are determined ($\vec{a}$ and $\vec{b}$). The distances between these two points in the xy-projection, Δ_{xy}, and in z-direction, Δ_z, are used to decide whether the two tracks come from a common vertex. The center point between $\vec{a}$ and $\vec{b}$ is taken as the conversion point. The distance in the xy plane of the conversion point from the origin at (0,0,0) is used to distinguish photon conversions from Dalitz pairs.

To remove additional combinatorial background, the distance d between the projected pair momentum vector and the primary vertex must not exceed 2.5 cm. The cut on the invariant mass is looser for Dalitz electrons. On the other hand, since Dalitz

pairs originate close to the primary vertex, the combinatorial background is higher. We therefore impose a tighter cut on Δ_{xy} and require the second track to pass a loose cut on dE/dx. For photon conversions an additional cut on the angle between pair momentum and the flight direction derived from the conversion point reduces combinatorial background by an additional factor of two.

Quantity	$\gamma \to e^+e^-$	$\pi^0/\eta^0 \to \gamma\, e^+e^-$
Δ_{xy}	$< 0.3\,\mathrm{cm}$	$< 0.2\,\mathrm{cm}$
Mass M_{ee}	$< 100\,\mathrm{MeV}/c^2$	$< 200\,\mathrm{MeV}/c^2$
R_{xy}	$> 1.6\,\mathrm{cm}$	$< 1.6\,\mathrm{cm}$
$\angle(\vec{p}_\gamma, \vec{R})$	$< \pi/2$	
dE/dx (2nd track)		≥ 525 *a.u.*
Hits in DCH (2nd track)	≥ 12	
p_t (2nd Track)	$\geq 0.1\,\mathrm{GeV}/c$	
Δ_z	$< 1\,\mathrm{cm}$	
d	$< 2.5\,\mathrm{cm}$	

Table 6.5: Criteria for identifying electrons from photon conversions and π^0/η^0 Dalitz pairs.

Using the standard $B\overline{B}$ MC sample, the efficiencies for identifying electrons from pair background and the impurity of the candidates selected by these cuts are determined as a function of momentum and polar angle. As can be seen in Figure 6.10, the efficiency for finding electrons from photon conversions varies between 30% and 40%. Further studies show that the main reason for this low efficiency are asymmetric $\gamma \to e^+e^-$ conversions, for which the momentum of the second lepton is too low to be reconstructed. As can be seen in Figure 6.9, 60% of all photon conversions cannot be detected for this reason. Since there are very few photons with energies above 2 GeV, all conversion electrons with high momenta must originate from asymmetric conversions, causing the decrease in efficiency above 1.6 GeV/c. For Dalitz decays, the spectrum of the second track is softer than for photon conversions, resulting in a lower overall efficiency.

The total number of background electrons originating from photon conversions or Dalitz pairs, N^{true}, is derived from the number of identified pair tracks found in the data, N^{found}. The efficiency ϵ and purity ρ are determined from MC simulations and combined to correction factors f_c (photon conversions) and f_d (Dalitz decays), which connect N^{true} and N^{found}:

$$\begin{aligned} \text{Photon conversions: } f_c &= \frac{\rho_c}{\epsilon_c} = \frac{N_c^{true}}{N_c^{found}}, \\ \text{Dalitz: } f_d &= \frac{\rho_d}{\epsilon_d} = \frac{N_d^{true}}{N_d^{found}}. \end{aligned} \tag{6.5}$$

To examine the systematic uncertainty for this background estimate, we rewrite the finder efficiency ϵ_c in terms of three factors

$$\epsilon_c = \epsilon_c^{pair}\epsilon_c^{trk}\epsilon_c^{vtx} \tag{6.6}$$

where

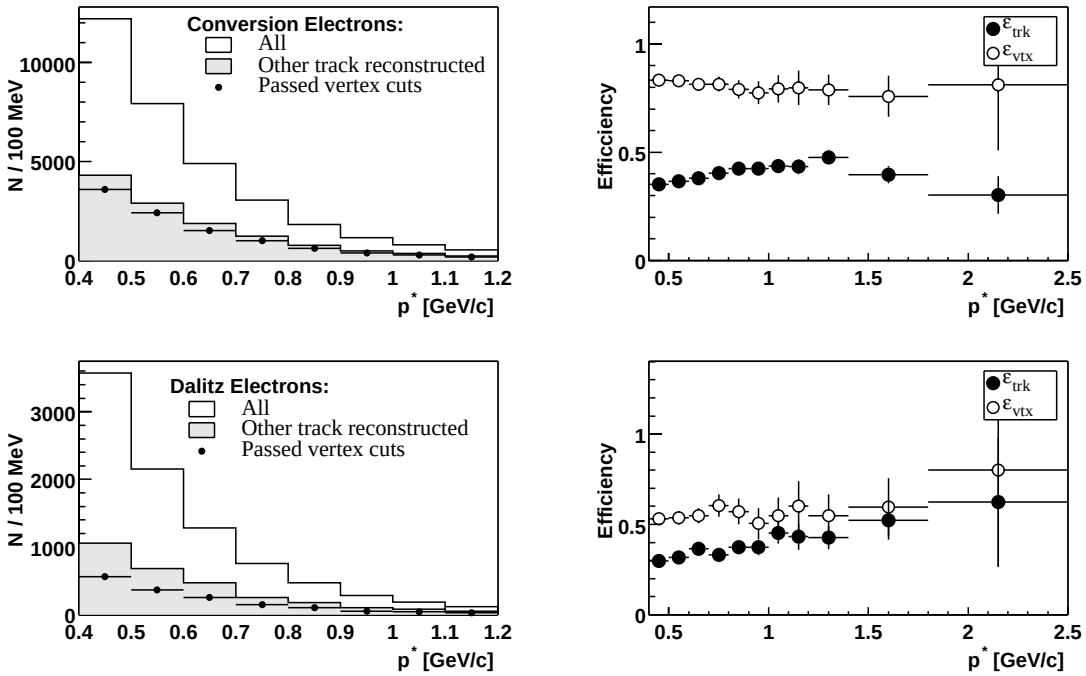

Figure 6.9: MC studies of pair finder efficiencies for photon conversions (top) and Dalitz decays (bottom).

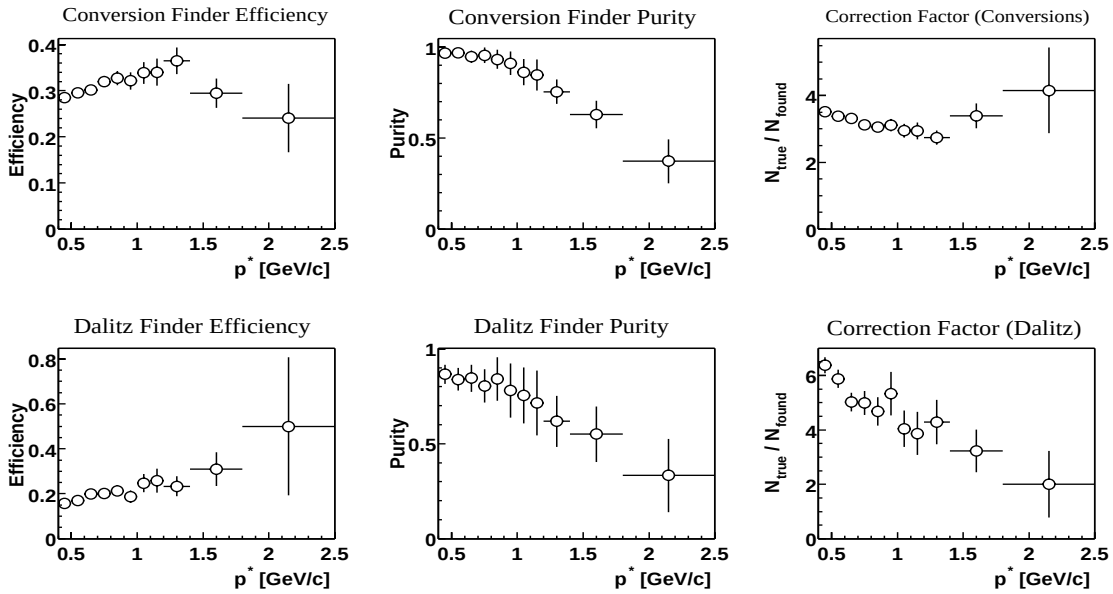

Figure 6.10: Efficiency, purity and correction factors for photon conversion and Dalitz pair finder.

- ϵ_c^{pair} is the probability for the other track to exceed $p_t > 0.1$ GeV/c, which is required to assure a high and well understood tracking efficiency. ϵ_c^{pair} depends on the underlying photon spectrum. To check how well this spectrum is reproduced in the Monte Carlo simulation, we compare the p_t distributions of found photon conversions in MC and data. Another check is the comparison of the energy spectrum of found converted photons in data and MC. As can be seen in Figure 6.11, the agreement is good. From this we derive an estimate of $\left(\Delta\epsilon_c^{pair}/\epsilon_c^{pair}\right)_{sys} = 10\%$.

- ϵ_c^{trk} is the probability for the second track to be reconstructed. ϵ_c^{trk} depends on the tracking efficiency, which at low momenta is known to 1% for tracks meeting the *GoodTracksLoose* requirements. We accept larger impact parameters for the second track than specified in *GoodTracksLoose*, and therefore estimate $\left(\Delta\epsilon_c^{trk}/\epsilon_c^{trk}\right)_{sys} = 1.5\%$.

- ϵ_c^{vtx} is the probability that once both tracks are reconstructed, they also pass the vertexing criteria listed in Table 6.5. We determine the uncertainty in this procedure by comparing the distributions of Δ_{xy}, Δ_z, and invariant mass M_{ee} for data and MC. While leaving the cuts on two of these variables fixed, the cut on the third is loosened, and the change in the yield is observed. From this study we arrive at a relative systematic uncertainty of $\left(\Delta\epsilon_c^{vtx}/\epsilon_c^{vtx}\right)_{sys} = 8\%$.

In summary, by adding the relative uncertainties in the individual efficiency factors in quadrature, we arrive at a total uncertainty. Specifically, for conversion background we obtain

$$\left(\frac{\Delta\epsilon_c}{\epsilon_c}\right)_{sys} = 13\%. \tag{6.7}$$

For Dalitz decays, ϵ_d^{vtx} is lower compared to photon conversions (Figure 6.10), which results in a higher relative error, $\left(\Delta\epsilon_d^{vtx}/\epsilon_d^{vtx}\right)_{sys} = 16\%$. Furthermore, since we require a loose electron identification for the second track, we have $\left(\Delta\epsilon_d^{trk}/\epsilon_d^{trk}\right)_{sys} = 2\%$. Combined with $\left(\Delta\epsilon_d^{pair}/\epsilon_d^{pair}\right)_{sys} = 10\%$, the systematic error on the Dalitz electron efficiency is

$$\left(\frac{\Delta\epsilon_d}{\epsilon_d}\right)_{sys} = 19\%. \tag{6.8}$$

We also have to consider relative systematic errors in the impurities $1-\rho_c$ and $1-\rho_d$, which we estimate to be 25 %. With $1-\rho_c = 0.02$ and $1-\rho_d = 0.1$, we arrive at

$$\left(\frac{\Delta\rho_c}{\rho_c}\right)_{sys} = 0.5\% \tag{6.9}$$

$$\left(\frac{\Delta\rho_d}{\rho_d}\right)_{sys} = 2.7\% \tag{6.10}$$

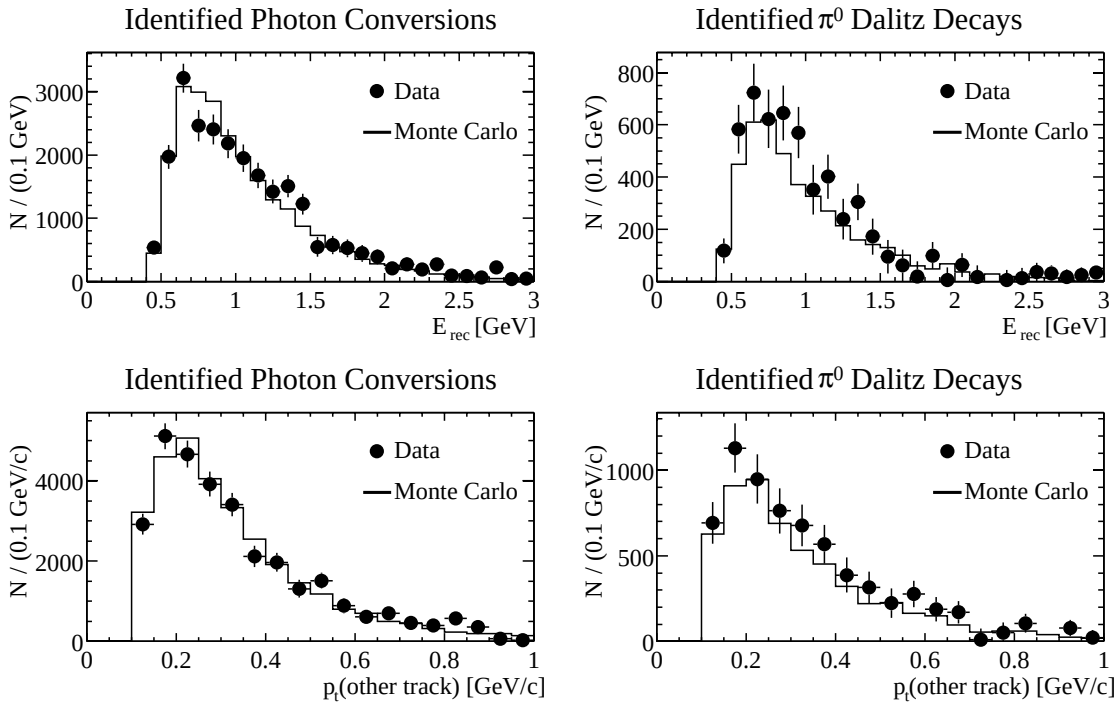

Figure 6.11: Data / MC comparison of pair background: distributions of photon energy (top) and p_t of the second track (bottom) found in photon conversion pairs (left) and Dalitz decays (right).

which turns out to be small compared to the uncertainties in the efficiencies, which dominate the systematic uncertainties in f_c and f_d.

With these correction factors, the true number of conversion electrons N_c and Dalitz electrons N_d is derived from the spectra of detected pairs for each momentum and polar angle bin:

$$N_c(p^*,\theta^*) = N_c^{found}(p^*,\theta^*) \times f_c(p^*,\theta^*) \qquad N_d(p^*,\theta^*) = N_d^{found}(p^*,\theta^*) \times f_d(p^*,\theta^*) \tag{6.11}$$

Figure 6.12 shows the observed and efficiency corrected CMS momentum spectra for background electrons from pair production, separately for like-sign and unlike-sign tag-electron pairs. The contribution seems to be larger for the like-sign sample, which is a consequence of the opening angle cut applied to the unlike-sign sample to suppress cascade decays. Since its efficiency decreases at low momenta, the spectra appear to be softer, though after proper correction for this efficiency, this is not the case.

The statistical error consists of the counting error in the raw number of electrons, and the error in the correction factors f_c and f_d due to a limited statistics of the MC sample. Tables 6.6 and 6.7 give a summary of the momentum integrated background ($p^* > 0.5\,\mathrm{GeV}/c$), separately for signal candidates in unlike-sign and like-sign pairs.

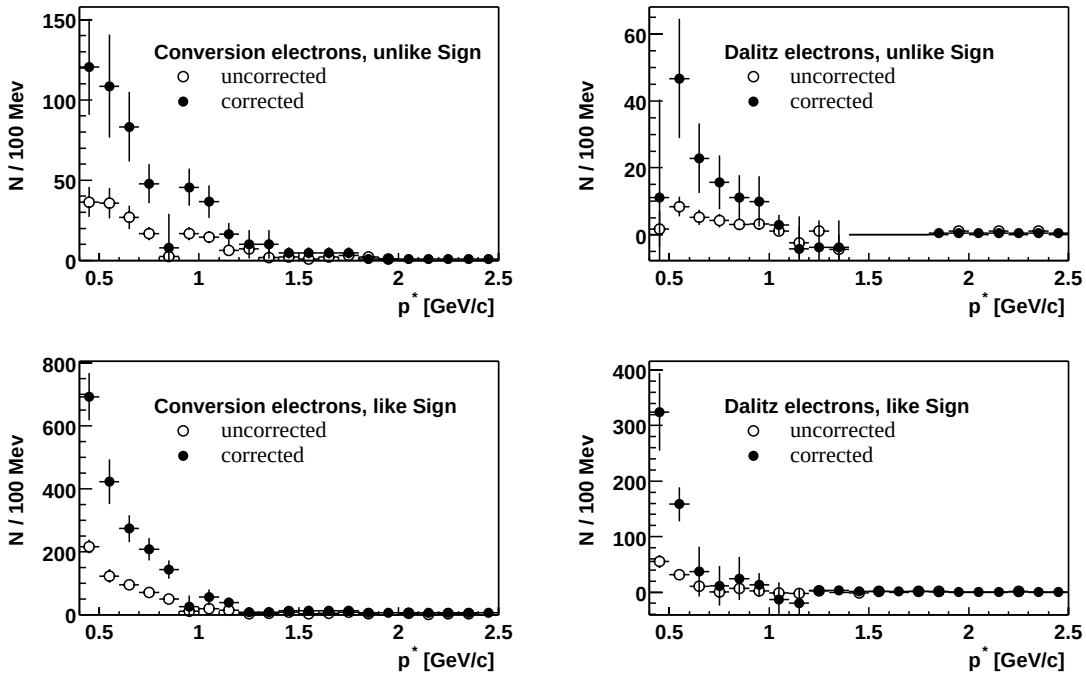

Figure 6.12: Observed and efficiency corrected spectra for electrons from $\gamma \to e^+e^-$ and $\pi^0/\eta \to \gamma e^+e^-$.

	e from $\gamma \to e^+e^-$	e from $\pi^0/\eta \to \gamma\, e^+e^-$
N_{On}	166.4 ($\pm$13.1)	30.2 ($\pm$5.7)
N_{Off}	6.3 ($\pm$2.7)	2.05 ($\pm$1.4)
$N_{raw} = N_{on} - \xi_{\mathcal{L}} * N_{Off}$	139.9 $(\pm 17.1)_{(stat)}$	21.4 $(\pm 8.4)_{stat}$
$N_{corr} = N_{raw} * f_{corr}$	392 $(\pm 51)_{stat}$ $(\pm 51)_{sys}$	98 $(\pm 28.5)_{stat}$ $(\pm 18.6)_{sys}$

Table 6.6: Summary of the pair background correction for the unlike-sign sample.

	e from $\gamma \to e^+e^-$	e from $\pi^0/\eta \to \gamma\, e^+e^-$
N_{On}	589.7 ($\pm$24.8)	110.2 ($\pm$10.7)
N_{Off}	37.6 ($\pm$6.2)	13.4 ($\pm$3.7)
$N_{raw} = N_{on} - \xi_{\mathcal{L}} * N_{Off}$	429.8 ($\pm$36.4)	52.89 ($\pm$19.1)
$N_{corr} = N_{raw} * f_{corr}$	1279 $(\pm 108)_{stat}$ $(\pm 166)_{sys}$	238 $(\pm 87)_{stat}$ $(\pm 45)_{sys}$

Table 6.7: Summary of the pair background correction for the like-sign sample.

6.3.2 Hadron Mis-Identification Background

The total correction for charged particles that are mis-identified as electrons is

$$N_{fake} = N_H\ \eta = (N_H^{ON} - \xi_{\mathcal{L}} N_H^{OFF})\ \sum_h f_h \eta_h, \tag{6.12}$$

Thus we need to determine

- N_H, the CMS spectrum of charged hadrons in tagged events that meet the same selection criteria as the signal candidate electrons, except for the electron identification; these spectra are taken from continuum subtracted lepton tagged event samples;
- f_h with $h = \pi, K, p$ and $\sum_h f_h = 1$, the fraction of hadrons of type h in a given sample. These fractions are taken from $B\overline{B}$ Monte Carlo simulations.

The probability η_h that a hadron of type h is misidentified as an electron has been derived in Sect. 4.7. All these quantities, N_H, h_f and η_h, are derived as functions of p^* and $\cos\theta^*$ using the *standard binning* (Sect. 5.2). The values of p^* and $\cos\theta^*$ are computed by boosting the tracks into the $\Upsilon(4S)$ rest frame assuming the electron mass.

Figure 6.13 shows the fractions f_h for two charge combinations, separately for hadrons which have the same and the opposite sign of the tag lepton. There are significant differences, especially at high momenta, where pions of opposite sign are favored.

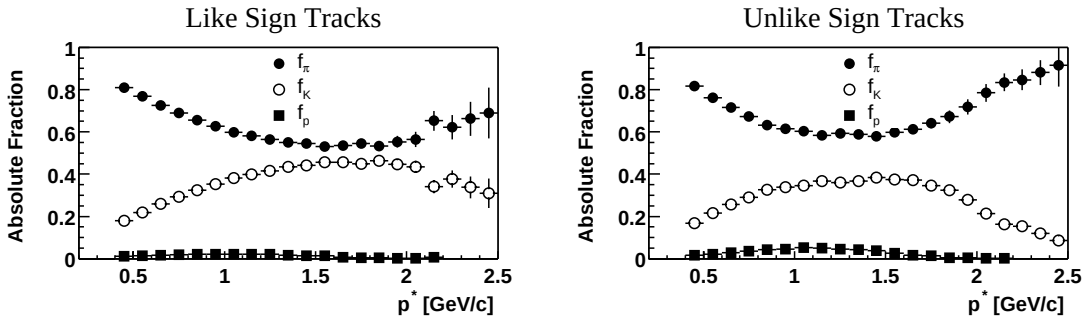

Figure 6.13: MC predictions for the fraction of pions, kaons, and protons as a function of the CMS momentum, a) for like-sign and b) for unlike-sign pairs of tag-leptons and hadrons.

Figure 6.14 shows the fake rates, separately for each hadron type and the total. At low momenta, the fake rate of $\approx 0.5\%$ is dominated by the kaon misidentification probability, and above 1 GeV/c, the average hadron fake rate is about 0.15% for positive and 0.1% for negative tracks. The increase of the kaon fake rate near 1.5 GeV/c is due to the fact that the DIRC information is not used for $p_{lab} > 1.5$ GeV/c.

The systematic errors on the fractions f_h are obtained by comparing the *BABAR* Monte Carlo with the ARGUS data [32], resulting in the following estimates:

$$\delta f_\pi / f_\pi = 3.5\% \quad \delta f_K / f_K = 15\% \quad \delta f_p / f_p = 20\%$$

The total number of hadron tracks is derived from the total number of measured tracks N and the number of identified electrons n_e,

$$N = N_H + N_e + N_\mu = N_H + (1 + r)N_e \tag{6.13}$$

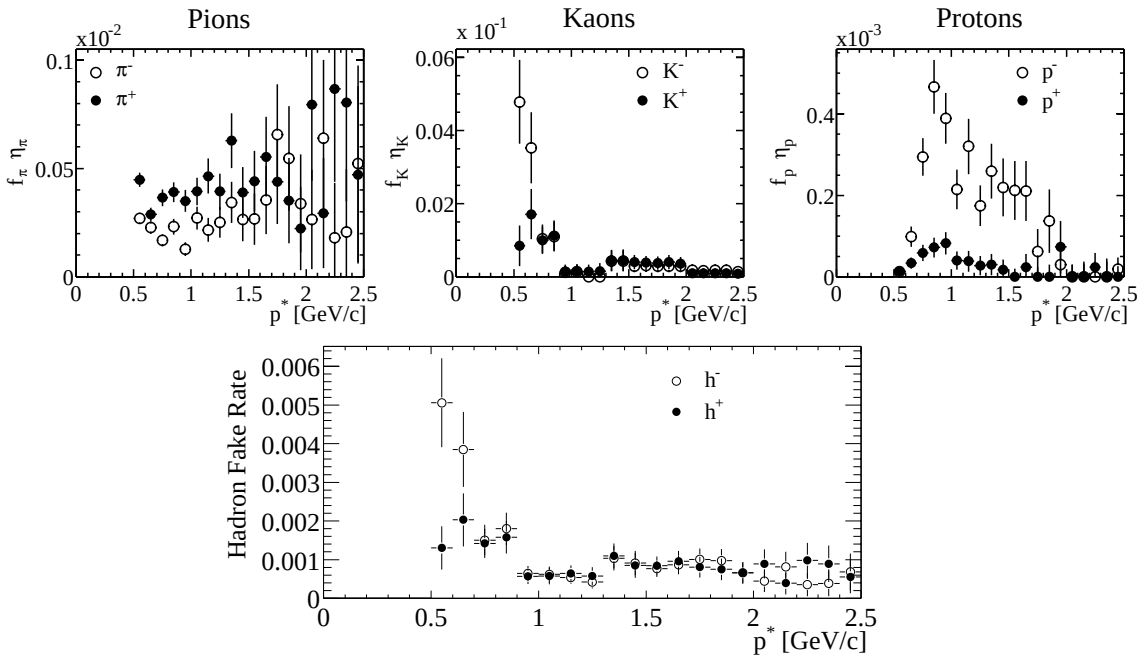

Figure 6.14: Hadron fake rates a-c) for individual hadrons, $f_h\eta_h^{\pm}$, and d) the total fake rate $\eta^{\pm} = \sum_h f_h\eta_h^{\pm}$ for unlike-sign hadron-tag-lepton pairs.

$$n_e = \epsilon N_e + \eta N_H \tag{6.14}$$

where N_H, N_e, N_μ refer to the true number of hadrons, electrons, and muons, and ϵ is the electron selection efficiency. Here we assume the probability that a muon fakes an electron is negligible.

To simplify the problem, we have introduced the ratio $r = N_\mu/N_e$. This ratio ranges from 0.9 at low to 1.3 at high momenta due to photon conversions, Dalitz decays and bremsstrahlung. Its momentum and θ dependent values are determined from MC simulation (see Figure 6.15).

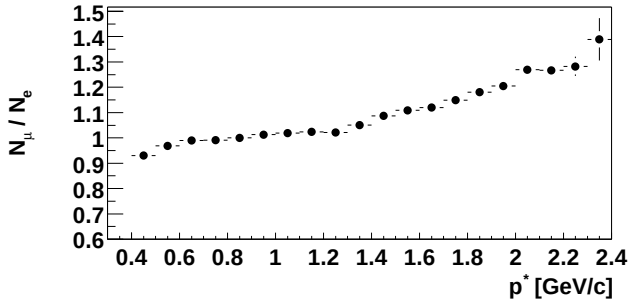

Figure 6.15: MC prediction of the ratio $r = N_\mu/N_e$ as a function of the lepton CMS momentum in generic $B\overline{B}$ events.

Based on Eq. 6.13 and 6.14 we derive the number of hadron tracks

$$N_H = \frac{N - (1+r)n_e/\epsilon}{1 - (1+r)\eta/\epsilon}. \tag{6.15}$$

Thus the spectra of misidentified hadron tracks (see Figure 6.16, and Figure 6.17) are obtained as

$$N_{h,fake} = N_H * f_h * \eta_h \qquad for \;\; h = \pi, K, p. \tag{6.16}$$

$N_{h,fake}$ is computed for each bin, yielding the faked hadron spectra in the *standard binning*.

Figure 6.16 shows the contributions from individual hadron species to the misidentification background for both like-sign and unlike-sign samples, separately for positive and negative charges. Their sum is shown in Figure 6.17. The background is dominated by misidentified Kaons, K^- exceed K^+.

The statistical error on the hadron background estimate is dominated by the statistical errors of the individual fake rates, which arise from the finite sizes of the pure particle control samples. The uncertainties in the total number of tracks N and relative hadron fractions f_h also contribute to the overall statistical error. The uncertainty in the electron efficiency ϵ and the ratio r turn out to be negligible.To estimate the systematic error on the misidentification rates η_h, we compare the numbers of misidentified hadrons using fakes rates determined with and without sideband subtraction in the control samples. We use half the difference as systematic uncertainty (Sect. 4.7). Table 6.10 shows the results.

Particle	N_{fake} SB sub.	N_{fake} no SB.sub.	$\left(\frac{\Delta\eta}{\eta}\right)_{sys}$	$\left(\frac{\Delta f}{f}\right)_{sys}$	$\left(\frac{\Delta N_{fake}}{N_{fake}}\right)_{sys}$
π	40.6	48.4	0.10	0.035	0.10
K	145.9	187.6	0.14	0.15	0.21
p	16.9	21.6	0.14	0.2	0.24

Table 6.8: Systematic study of fake rate for unlike-sign sample

Particle	N_{fake} SB sub.	N_{fake} no SB.sub.	$\left(\frac{\Delta\eta}{\eta}\right)_{sys}$	$\left(\frac{\Delta f}{f}\right)_{sys}$	$\left(\frac{\Delta N_{fake}}{N_{fake}}\right)_{sys}$
π	105.6	127.4	0.10	0.035	0.11
K	487.4	598.2	0.11	0.15	0.19
p	21.8	29.6	0.18	0.2	0.27

Table 6.9: Systematic study of fake rate for like-sign sample

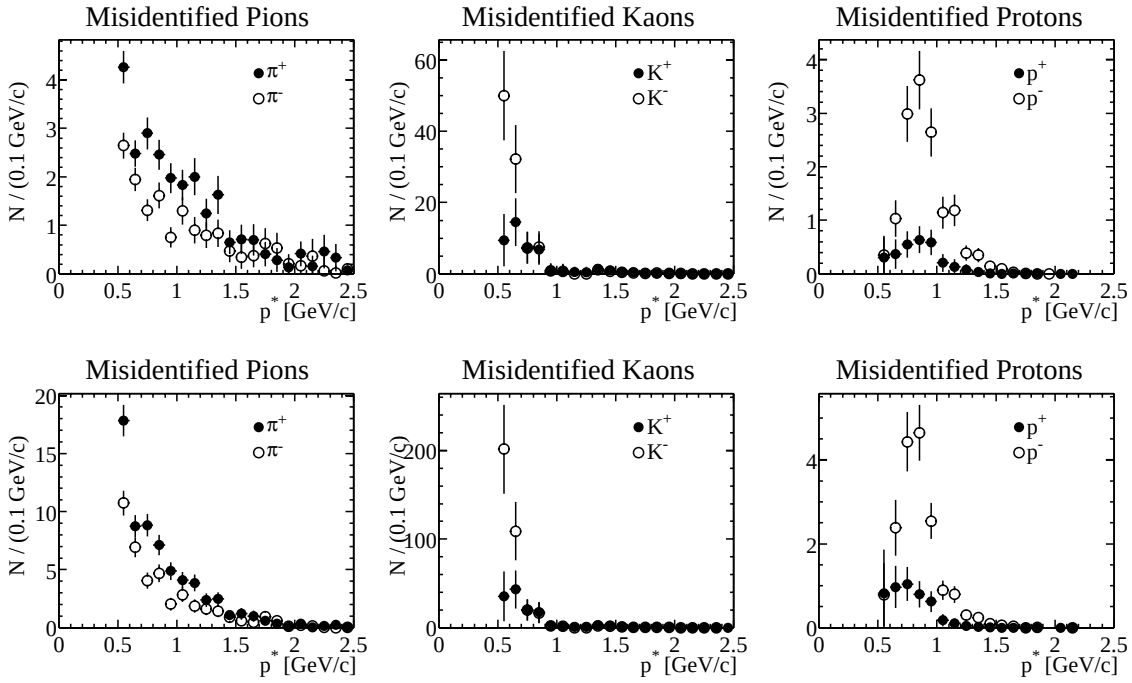

Figure 6.16: Background due to misidentified hadrons in unlike-sign (top) and like-sign (bottom) sample as a function of the CMS momentum.

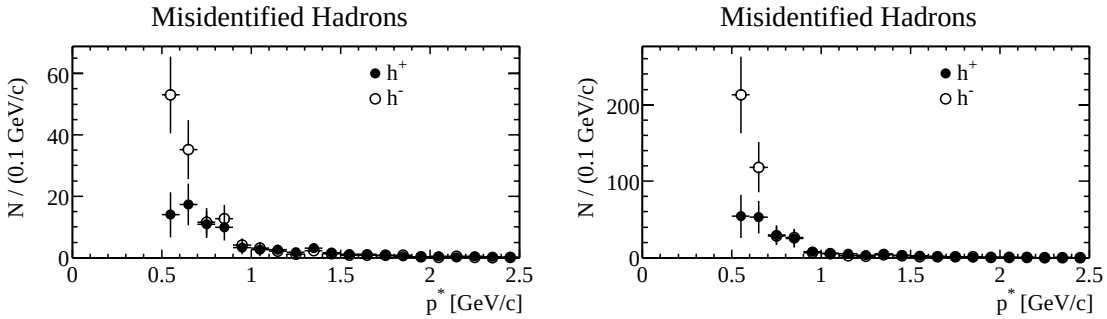

Figure 6.17: Spectra of misidentified hadrons for un-like sign(left) and like-sign (right) samples.

Particle	unlike-sign			like-sign		
π	40.6	$\pm$1.7	$\pm$4.1	105.6	$\pm$3.6	$\pm$11.5
K	145.9	$\pm$21.4	$\pm$30.2	487.4	$\pm$74.8	$\pm$91.7
p	16.9	$\pm$1.3	$\pm$4.1	21.8	$\pm$2.0	$\pm$5.9
total	204	$\pm$21	$\pm$31	615	$\pm$75	$\pm$93

Table 6.10: Summary of misidentified hadrons; the errors are $\pm$ statistical $\pm$ systematic

6.3.3 Secondary Decays from Tagged B

Since the process $B \to X_c\, e^+_{tag}\, \nu,\ X_c \to X\, e^-\, \overline{\nu}$ favors larger angles α between tag- and signal electron, most of these opposite-sign pairs are removed by the cut given in Eq. 6.1. To quantify the background formed by the remaining pairs, the distribution of $\cos\alpha$ is analyzed for the unlike-sign sample, which can be decomposed into three categories:

1. Tracks showing no angular correlation to the tag; since the two B mesons are produced nearly at rest in the CMS , all electrons originating either directly or from cascade decays of the signal B can be assigned to this group. Monte Carlo studies indicate that misidentified hadrons do not show an angular correlation to the tagged lepton either.

2. Electrons from secondary decays of the tagged B

3. Electrons from other background processes showing non-flat $\cos\alpha$ distributions. Monte Carlo studies indicate that the opening angle distribution between tag leptons originating from semileptonic decays and electrons produced by photon conversions or Dalitz decays has this property. This can be explained by the fact that the underlying photon or π^0 can originate from the tagged B, and therefore its momentum direction is not independent from the direction of the tag electron.

Starting with the raw opposite-sign sample without an opening angle cut applied, we use the algorithm described in Sect. 6.3.1 to determine the number of conversion and Dalitz electrons. The contribution of these processes to the total $\cos\alpha$ distribution is then estimated by normalizing the opening angle distribution extracted from Monte Carlo to these numbers. For the process $\gamma \to e^+e^-$, we arrive at an estimate of $1287 \pm 110_{(stat)} \pm 167_{(sys)}$ tracks, and the number of electrons from $\pi^0 \to \gamma\, e^+e^-$ is $302 \pm 80_{(stat)} \pm 57_{(sys)}$. Figure 6.18 shows the $\cos\alpha$ histograms after subtraction of this pair background.

To determine the number of tracks from category #2, a function of the form

$$f(\cos\alpha) = c_0 + c_1 f_{same}(\cos\alpha) \tag{6.17}$$

is fitted to these histograms, where c_0 represents the flat contribution of tracks from category #1, and the shape $f_{same}(\cos\alpha)$ for electrons from cascade decays of the tagged B has been taken from the Monte Carlo simulation. The number $N^{\pm\mp}_{same}$ of such electrons passing the opening angle cut is then computed from the integral of $c_1 f_{same}$ between the minimal allowed value of $\cos\alpha$ (as specified in Eq. 6.1) and 1. This extraction of $N^{\pm\mp}_{same}$ is performed between 0.5 GeV/c and 1.2 GeV/c, in bins of 100 MeV/c. Monte Carlo studies show that above 1.2 GeV/c, the J/ψ - veto applied in the selection of the tag electron (Eq. 6.3) distorts the uniformity of the $\cos\alpha$ distribution below -0.2 for all processes significantly. Therefore, we determine $N^{\pm\mp}_{same}$ for $p^* > 1.2$ GeV/c from the Monte-Carlo simulation. The normalization is determined by fitting the MC prediction of $N^{\pm\mp}_{same}$ to the observed spectrum between 0.5 and 1.2 GeV/c. The final spectrum $dN^{\pm\mp}_{same}/dp^*$ is shown in Fig. 6.19. Integration yields $N^{\pm\mp}_{same} = 508 \pm 11_{(stat)}$.

Since the opening angle distribution of electron pairs originating from the same B meson depends on the decay channel, a systematic error is imposed onto the form of $f_{same}(\cos\alpha)$ due to uncertainties in the involved branching fractions. Table 6.11 gives an

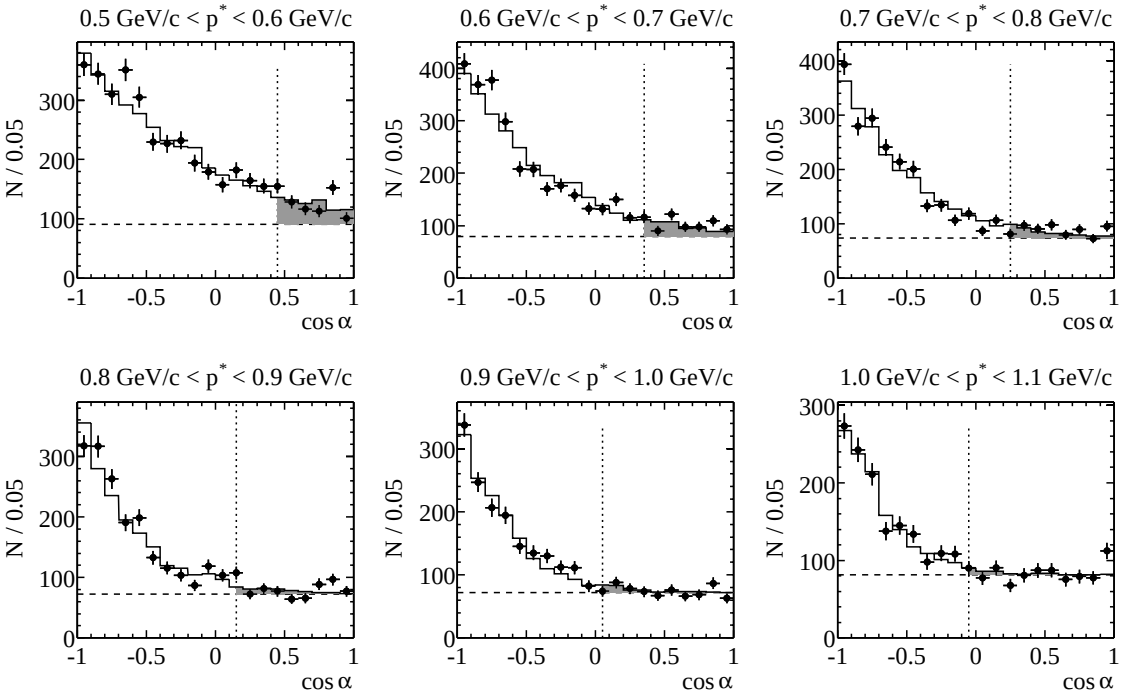

Figure 6.18: Opening angle distribution after subtraction of contributions from electrons originating in photon conversions or Dalitz decays: the solid lines show results of fitting Eq. 6.17 to the data points, with the dashed line indicating the flat contribution c_0. The vertical lines indicate the cuts on $\cos\alpha$, and the grey areas represent tracks from the non-flat background passing these cuts.

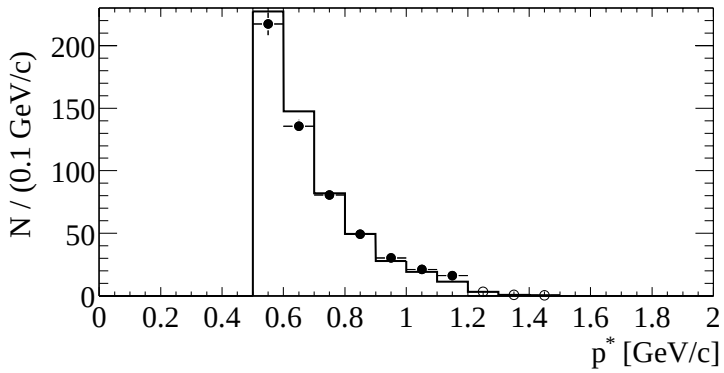

Figure 6.19: Spectrum of secondary electrons from the tagged B (dots); the solid line shows the MC-prediction fitted to the data derived points (solid) between 0.5 and 1.2 GeV/c. The spectrum above 1.2 GeV/c (hollow points) is taken from this fitted MC-prediction.

overview of the considered decay modes and the underlying models used in the Monte Carlo simulation (see also Sect. 2.4). To study the influence on $N_{same}^{\pm\mp}$, the relative fractions of the individual decay modes are varied according to the relative uncertainties of their branching fractions. Each time, we derive a new function $f_{same}(\cos\alpha)$ and determine $N_{same}^{\pm\mp}$ using the fitting procedure from above. From this, we arrive at a systematic error of ± 20 tracks.

Decay Mode	Model	Branching Fraction	Relative uncertainty
$B \to D\, e_{tag}^{+}\, \nu$	ISGW2 [20]	2.1 %	7%
$B \to D^{*}\, e_{tag}^{+}\, \nu$	HQET [22]	5.6 %	8.5%
$B \to D^{**}\, e_{tag}^{+}\, \nu$	ISGW2	1.5 %	25%
$B \to D^{(*)}\pi\, e_{tag}^{+}\, \nu$ (non-resonant)	Goity-Roberts [34]	1.2%	50%

Table 6.11: Decay modes considered for the $\cos\alpha$ distribution of lepton pairs from the same B meson.

Another source of systematic errors is the background in the $\cos\alpha$ distributions originating from photon conversions and Dalitz decays. Varying the normalization factors for the opening angle distributions within the statistical and systematic errors stated above results in an additional uncertainty of 8 tracks. To explore the systematic error due to a possibly poor modeled shape of the $\cos\alpha$ distribution, we determine $N_{same}^{\pm\mp}$ assuming a constant probability function for $\cos\alpha$. As systematic error, we assign 25% of the difference to the result obtained with the MC model. Table 6.12 summarizes all systematic errors.

Source	Systematic Error
Shape of $\cos\alpha$ distribution for lepton pairs from same B	± 20
Number of photon conversion and Dalitz electrons contributing to $\cos\alpha$ distribution	± 8
Shape of $\cos\alpha$ distribution for electrons from photon conversions or Dalitz decays	± 11
Total	± 24

Table 6.12: Systematic errors in determination of $N_{same}^{\pm\mp}$.

6.3.4 Electron Efficiency Correction

The subtraction of secondary decays of the tagged B, pair and hadron fake background from the raw spectrum (Figure 6.20) yields the spectrum of *physics electrons*, which has to be corrected for the electron detection efficiency. This is done in bins of CMS momentum and polar angle. As a first step, we use the efficiencies derived from radiative Bhabha control samples. Then, we derive the same corrections based on efficiency tables based on Monte Carlo generated radiative Bhabha events and $\Upsilon(4S)$ events to

quantify the dependence of the electron identification on the event topology. The ratio of these efficiencies is then used as a correction to the numbers obtained in the first step, assuming a relative uncertainty of 50%. As can be seen from Table 6.13, the average electron identification efficiency for the unlike-sign sample is 89.0% , with an estimated uncertainty of $(\Delta\epsilon/\epsilon)_{sys} = 1.2\%$. Since the spectrum of like-sign electrons is softer, the average efficiency is smaller.

	Yield for Unlike-Sign	Yield for Like-Sign
Raw Physics Electrons	12974	10820
Efficiency Correction(Rad. Bhabhas)	14227 ± 7	11866 ± 7
Correction for event topology	14582 ± 66	12310 ± 43
Difference	355	443
Systematic Error $\Delta\epsilon/\epsilon$	1.2 % $_{(\pm 0.22)}$	1.8 % $_{(\pm 0.17)}$

Table 6.13: Efficiency correction to the number of identified physics electrons; the erros represent the statistical uncertainties in the efficiency tables involved in this study.

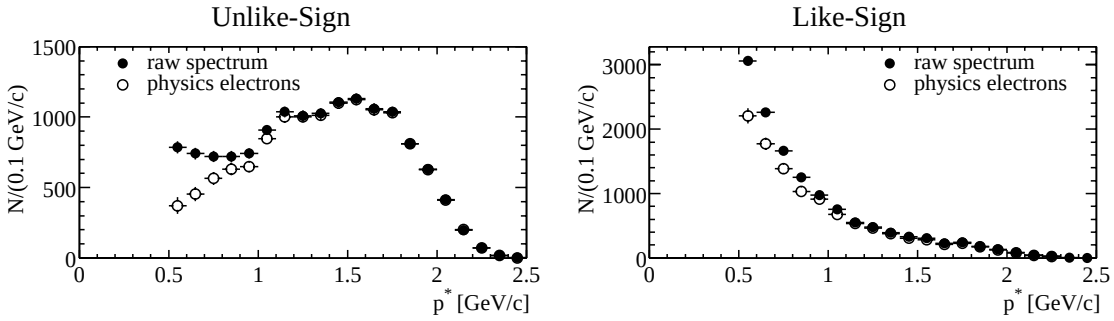

Figure 6.20: Spectra before and after subtraction of secondary decays from tagged B, pair- and misidentified hadrons background

6.3.5 Background Electrons from other Weak Decays

There are several weak decay processes in $B\overline{B}$ events that contribute to tag electrons and electrons in the like-sign and unlike-sign samples of dilepton events. These background contributions are estimated by performing the full analysis on Monte Carlo samples. Systematic errors are dominated in most cases by the uncertainty in the branching ratios, but uncertainties in the dynamics of the decay process also contribute. We have checked the branching ratios used in the $B\overline{B}$ generic Monte Carlo and in some cases rescaled the rates to reflect the latest measurements from LEP and CLEO.

In the following, we list the background processes that have been considered and estimate the systematic uncertainties arising from the limited knowledge of the branching ratios:

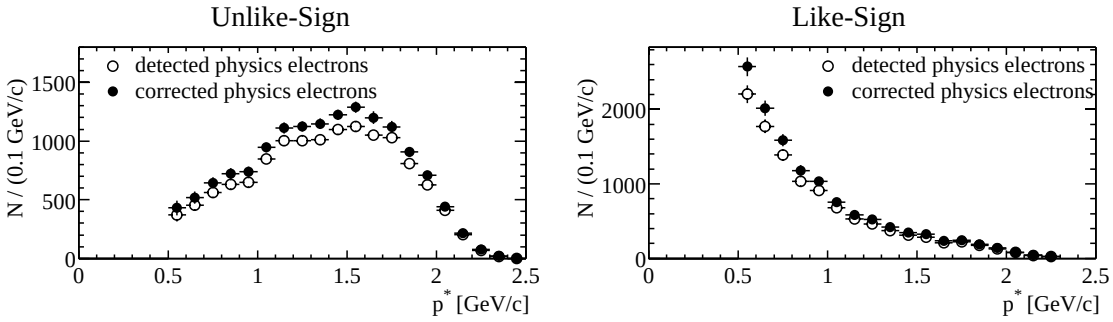

Figure 6.21: Spectra before and after electron identification efficiency correction

- Electrons from wrong-flavor D_s and D decays
  As shown in Figure 6.22, a B meson (containing a $\overline{b}$) can decay to wrong-flavor charm mesons via a W^+ fragmenting into $c\overline{s}$, leading to a $D_s^{(*)+}$ or $D^{(*)}K$ in the final state of the non-tag B. A subsequent semileptonic decay of the $D_s^{(*)+}$ or $D^{(*)}$ contributes an electron to the unlike-sign sample (unless mixing of the B has occurred). Electrons from $D_s \to \tau$ are treated separately.

  1. $B \to D_s^{(*)+} X \to X'\, l\, \nu$
     The branching fraction of "upper vertex" D_s production is assumed to be $\mathcal{B}(B \to D_s^+) = (9.8 \pm 3.7)\%$ [35]. The uncertainty is larger than for the total inclusive rate of D_s production, which is currently measured to be $(10 \pm 2.5)\%$ [33]. Following the argumentation in [2], we derive $\mathcal{B}(D_s \to Xe\nu)$ from $\mathcal{B}(D^{0,\pm} \to Xe\nu)$ and the lifetime ratios $\tau_{D^{0,\pm}}/\tau_{D_s}$, assuming equal semileptonic decay widths. With $\mathcal{B}(D_s \to Xe\nu) = (8.0 \pm 1.9)\%$ this results in a total rate branching fraction of $\mathcal{B}(B \to D_s \to e) = (0.78 \pm 0.35)\%$, thus the total systematic error is 45%.
  2. $B \to D$ decays
     The external diagram for this process is also shown below and semileptonic decays of the D mesons also contribute to the unlike-sign sample. The ALEPH collaboration determined the inclusive branching fraction $\mathcal{B}(B \to D^*\overline{D}^{(*)}K^{0,\pm})$ to be $(7.1 \pm 2.2)\%$ [36]. Combined with the uncertainties in semileptonic D decays

$$\frac{\Delta\mathcal{B}(D^0 \to Xl\nu)}{\mathcal{B}(D^0 \to Xl\nu)} = 4.3\% \quad \text{and} \quad \frac{\Delta\mathcal{B}(D^+ \to Xl\nu)}{\mathcal{B}(D^+ \to Xl\nu)} = 11.5\% \ ,$$

     we arrive at a relative uncertainty of 32% in the estimation of this background.

- J/ψ and $\psi(2S)$ decays
  Electrons from J/ψ and $\psi(2S)$ decays are removed by the opening angle cut. The remaining background is small and consists predominantly of decays in which one of the electrons is not detected. The measured inclusive branching ratios are $\mathcal{B}(B \to J/\psi\,) = (1.15 \pm 0.06)\%$ and $\mathcal{B}(B \to \psi(2S)) = (0.35 \pm 0.05)\%$ [33] resulting in $\mathcal{B}(B \to$

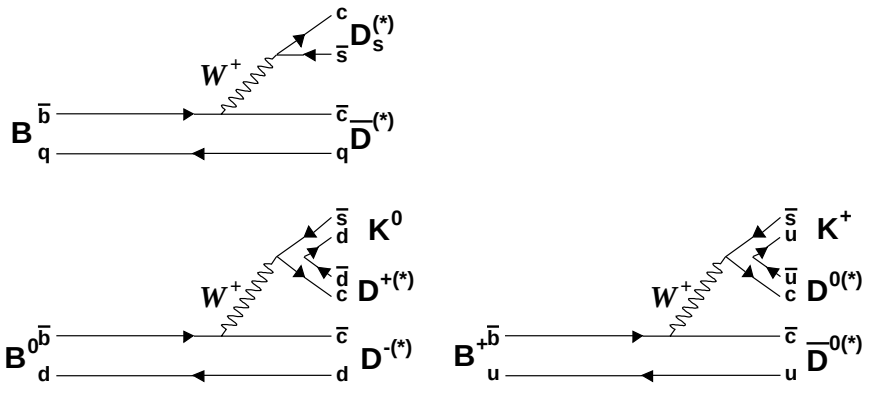

Figure 6.22: Diagrams for D_s and $D\overline{D}K$ production.

$J/\Psi \to e^+e^-) = (6.8 \pm 0.4) \times 10^{-4}$ and $\mathcal{B}(B \to \psi(2S) \to e^+e^-) = (3.1 \pm 0.6) \times 10^{-5}$, i.e. 6% and 20% uncertainties in the production rates.

- Electrons from $\tau^\pm$ decays
  There are two principal sources of $\tau^\pm$ that can contribute electrons. The semileptonic decay $B \to X\tau^+\nu$ with $\tau^+ \to e^+\nu\nu$ represents a background to the unlike-sign sample. The branching fractions are $\mathcal{B}(B \to X\tau\nu) = 2.5 \pm 0.2\%$ and $\mathcal{B}(\tau^+ \to e^+\nu\nu) = 17.83 \pm 0.06\%$, resulting in a combined branching fraction $\mathcal{B}(B \to \tau \to e) = 0.44 \pm 0.4\%$, i.e. a 10% uncertainty.

  $\tau^\pm$ also originate from D_s decays via the cascade $B \to D_s^+ X$, $D_s^+ \to \tau^+\nu$, $\tau^+ \to e^+\nu\nu$, they also contribute to the unlike-sign sample. The branching fractions are $\mathcal{B}(B \to D_s^+ X) = 9.8 \pm 3.7\%)$ and $\mathcal{B}(D_s^+ \to \tau^+\nu) = 7 \pm 4\%$ resulting in a combined value of $\mathcal{B}(B \to D_s^+ \to \tau^+ \to e^+) = 0.12 \pm 0.07\%$.

- Electrons in mis-tagged events
  We call events where the tag lepton candidate is either a misidentified hadron or originates from processes other than

  - $B \to X_c l\nu$,
  - $B \to D_s X, D_s \to l\nu$, or
  - $B \to X\ \tau^+\ \nu, \tau^+ \to l^+\nu\nu$,

  "mis-tagged" events. In case the high momentum lepton is from a secondary decay, the charge correlation between this tag track and the prompt signal electron is inverted. Other backgrounds are photon conversions, J/ψ decays and misidentified hadrons, which show no charge correlation to the tag. Thus we subtract all signal electrons in mistagged dilepton pairs, separately for like and unlike-sign pairs. We estimate this contribution by performing this analysis on Monte Carlo simulated samples and isolating lepton pairs for which the tag candidate is neither a prompt electron nor originating from the cascade decays listed above. We utilize

the technique of "PID-killing" [37] to match the simulated hadron misidentification rate to the one measured on data. The number of signal electrons found in this analysis serves as an estimate for the background in mistagged events. Since the primary source of mistagged events are secondary electrons, for which we estimate a relative systematic uncertainty of 20%, we use the this estimate also as error on this correction.

Using the ratio of tag electron yields obtained from analyzing the data and MC-sample as normalization, the MC - predictions of the various backgrounds are scaled to match the data sample. Figure 6.23 shows the resulting spectra, and the resulting corrections are listed in Table 6.14.

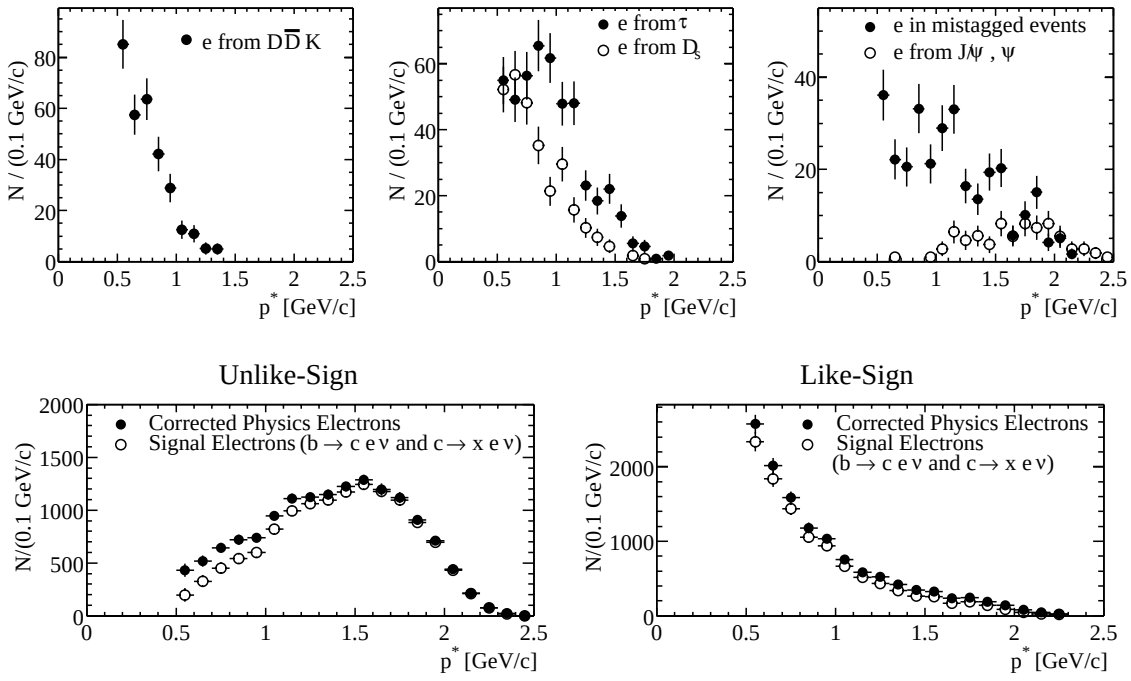

Figure 6.23: Correction to electron spectrum for other weak decay processes: top: background spectra for unlike-sign sample, bottom: subtraction of physics background for unlike-sign and like-sign samples.

Source	$\left(\frac{\Delta N}{N}\right)_{sys}$	Unlike-Sign	Like-Sign
e from τ	10%	$474 \pm 21_{(stat)} \pm 47_{(sys)}$	$136 \pm 11_{(stat)} \pm 14_{(sys)}$
$B \to D\overline{D}K$	32 %	$311 \pm 18_{(stat)} \pm 99_{(sys)}$	$96 \pm 10_{(stat)} \pm 31_{(sys)}$
e from D_s	45%	$284 \pm 16_{(stat)} \pm 128_{(sys)}$	$92 \pm 9_{(stat)} \pm 41_{(sys)}$
e from J/ψ	5%	$71 \pm 8_{(stat)} \pm 4_{(sys)}$	$112 \pm 10_{(stat)} \pm 6_{(sys)}$
e from ψ'	20%	$6 \pm 2_{(stat)} \pm 1_{(sys)}$	$8 \pm 3_{(stat)} \pm 2_{(sys)}$
e in mistagged events	20%	$335 \pm 18_{(stat)} \pm 67_{(sys)}$	$979 \pm 30_{(stat)} \pm 196_{(sys)}$
Total		$1480 \pm 38 \pm 181$	$1424 \pm 36 \pm 203$

Table 6.14: Physics background determined from MC, normalized by $N_{tag,Data}/N_{tag,Mc}$.

6.4 Unfolding Spectra of Primary and Secondary Electrons

Denoting the background corrected unlike- and like-sign spectra obtained in the previous chapter by $\frac{dN^{\pm\mp}}{dp^*}$ and $\frac{dN^{\pm\pm}}{dp^*}$, we use Eq. 5.1 and 5.2 to derive similar equations for the spectra of prompt and secondary electrons:

$$\frac{dN^{\pm\mp}}{dp^*} = \epsilon_{doca}(p^*)\ \epsilon_{oa}(p^*)\left[\frac{dN_{b\to cl\nu}}{dp^*}(1 - f_0\chi_0) + \frac{dN_{c\to yl\nu}}{dp^*}f_0\chi_0\right]$$

$$\frac{dN^{\pm\pm}}{dp^*} = \epsilon_{doca}(p^*)\ \epsilon_{oa}(p^*)\left[\frac{dN_{b\to cl\nu}}{dp^*}f_0\chi_0 + \frac{dN_{c\to yl\nu}}{dp^*}(1 - f_0\chi_0)\right]\ ,$$

where $\epsilon_{oa}(p^*)$ is the efficiency of the opening angle cut as derived in Sect. 6.1.4. Since we corrected for the track finding efficiency at the beginning of this analysis by applying the appropriate weights, $\epsilon_{doca}(p^*)$ represents the efficiency of the additional cut on the impact parameter only (Sect. 6.2). Solving these equations yields

$$\frac{dN_{b\to cl\nu}}{dp^*} = \frac{1}{\epsilon_{doca}(p^*)\ \epsilon_{oa}(p^*)(1-2\chi)}\left((1-\chi)\frac{dN^{\pm\mp}}{dp^*} - \epsilon_{oa}(p^*)\chi\frac{dN^{\pm\pm}}{dp^*}\right), \qquad (6.18)$$

$$\frac{dN_{c\to yl\nu}}{dp^*} = \frac{1}{\epsilon_{doca}(p^*)\ \epsilon_{oa}(p^*)(1-2\chi)}\left(\epsilon_{oa}(p^*)(1-\chi)\frac{dN^{\pm\pm}}{dp^*} - \chi\frac{dN^{\pm\mp}}{dp^*}\right), \qquad (6.19)$$

where $\chi = f_0\chi_0$. Figure 6.24. shows the final spectra of prompt and secondary electrons.

6.5 Correction for Bremsstrahlung

To arrive at the actual $B \to Xe\nu$ spectra, we must correct the distributions from Figure 6.24 for momentum resolution and radiative processes in the detector. We use our Monte Carlo sample to quantify the influence of these effects on the momentum reconstruction. With the following binning

$$p_i^* \in \{0;\ 0.5\ ;\ 0.6\ ;\ 0.7\ ;\ 0.8\ ;...;\ 2.4\ ;\ 2.5\ \} \qquad (6.20)$$

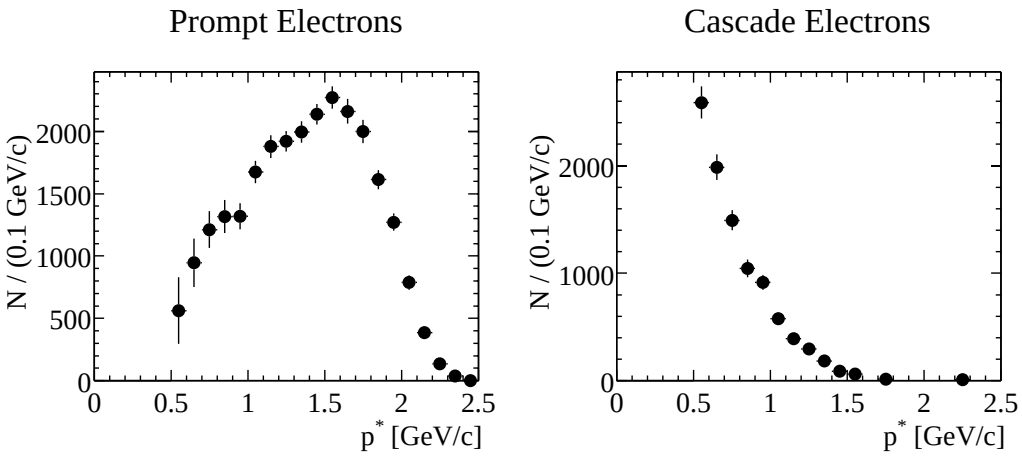

Figure 6.24: Spectra of primary (left) and secondary (right) electrons after all corrections.

we can determine the probability a_{ij} of a track with a true momentum within bin j being reconstructed in bin i ($0 \leq i, j \leq 21$) from the distributions of $p^*_{measured}$ for a given set of tracks within a given bin of p^*_{true}. These probabilities have to be normalized to 1:

a_{ij} = Probabilty of a track with a true momentum within bin j being reconstructed in bin i

$$\sum_i a_{ij} = 1 \qquad 0 \leq j \leq 21 \tag{6.21}$$

With these probabilities, the number of reconstructed tracks $\tilde{N}_i$ within bin i can be expressed by the original spectrum $\{N_0, N_1, N_2, .., N_{21}\}$:

$$\tilde{N}_i = a_{i0}N_0 + a_{i1}N_1 + ... + a_{i;21}N_{21} = \sum_j a_{ij} * N_j \tag{6.22}$$

With A being a matrix formed by the a_{ij}, $\vec{N} = (N_0, N_1, N_2, .., N_{21})$ being the true spectrum and the measured spectrum $\vec{\tilde{N}} = (\tilde{N}_0, \tilde{N}_1, \tilde{N}_2, .., \tilde{N}_{21})$, this can be written as a matrix equation which can be solved:

$$\vec{\tilde{N}} = A\vec{N} \tag{6.23}$$

$$\vec{N} = A^{-1}\vec{\tilde{N}} \tag{6.24}$$

Fig. 6.25 shows the resulting spectrum when applying this correction on the measured spectrum from Fig. 6.24

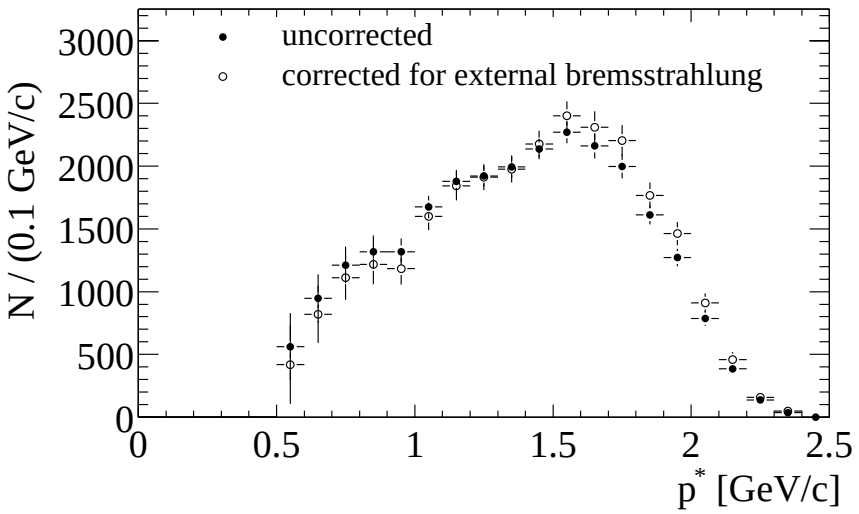

Figure 6.25: Spectrum of prompt electrons before and after correction for external bremsstrahlung.

Chapter 7

Determination of the Branching Fraction and of $|V_{cb}|$

7.1 Visible Branching Fraction

Assuming a systematic uncertainty of 0.5% in the ratio $\xi_{\mathcal{L}}$ of on to off resonance luminosity, and subtracting momentum integrated backgrounds derived in Sections 6.3.1, 6.3.2 and 6.3.3 yields the number of detected physics electrons (Table 7.1):

$$N^{\pm\mp}_{phys,detected} = 12974 \pm 163_{(stat)} \pm 68_{(sys)} \qquad N^{\pm\pm}_{phys,detected} = 10820 \pm 213_{(stat)} \pm 196_{(sys)}$$

Correcting for electron identification probability with relative systematic uncertainties of 1.2% for the unlike-sign and 1.8% for the like-sign sample (Table 6.13), we obtain the corrected number of physics electrons:

$$N^{\pm\mp}_{phys} = 14582 \pm 190_{(stat)} \pm 209_{(sys)} \qquad N^{\pm\pm}_{phys} = 12310 \pm 233_{(stat)} \pm 296_{(sys)}$$

The last correction is the subtraction of the "physics background" (Table 6.14), i.e. all electrons which either do not originate from $b \to xl\nu$ or $c \to xl\nu$ decays of the signal B or are cascades of $c\bar{c}s$ processes.

$$N^{\pm\mp} = 13102 \pm 196_{(stat)} \pm 277_{(sys)} \qquad N^{\pm\pm} = 10888 \pm 235_{(stat)} \pm 359_{(sys)}$$

Correcting the number of unlike-sign pairs by the efficiency of the cascade suppression cut yields

$$\sum_i \frac{N_i^{\pm\mp}}{\epsilon_i} = 24051 \pm 449_{(stat)} \ .$$

Since the values of ϵ_i have been derived from geometrical considerations only, there is no statistical error connected to them. The only source for a systematic error is a possible non-flatness of the opening angle distribution, since the two B mesons are not at rest. To study this difference, we determine the average efficiency on an enlarged MC sample (which includes all generic $B\overline{B}$ events produced at *BABAR* using the full detector simulation) and compare it with the value for a flat opening angle distribution:

$$\epsilon_{flat} = 54.52\% \qquad \epsilon_{MC} = 54.58 \pm 0.2_{(stat)}\%$$

We conclude that the systematic error on ϵ is insignificant. The number of electrons produced in $b \to c\, e\nu$ transitions is then obtained by integration of Eq. 6.18 between 0.5 and 2.5 GeV/c. With $\chi_0 = 0.174 \pm 0.009$ and $f_0 = 0.5 \pm 0.02$ we arrive at

$$N_{b\to xe\nu} = 25633 \pm 506_{(stat)} \ .$$

	Unlike-sign			Like-sign		
	N	$\Delta N_{(stat)}$	$\Delta N_{(sys)}$	N	$\Delta N_{(stat)}$	$\Delta N_{(sys)}$
ON Peak	15679	$\pm$ 127		14179	$\pm$ 121	
OFF Peak	1503	$\pm$ 81	$\pm$ 8	1226	$\pm$ 73	$\pm$ 6
$\gamma \to e^+e^-$	392	$\pm$ 51	$\pm$ 51	1279	$\pm$ 108	$\pm$ 166
$\pi^0 \to \gamma e^+e^-$	98	$\pm$ 28	$\pm$ 19	238	$\pm$ 87	$\pm$ 45
Cascade e from tagged B	508	$\pm$ 11	$\pm$ 24			
Faked Hadrons	204	$\pm$ 21	$\pm$ 31	615	$\pm$ 75	$\pm$ 93
Net e yield	12974	$\pm$ 163	$\pm$ 68	10820	$\pm$ 213	$\pm$ 196

Table 7.1: Extraction of number of physics electrons.

To calculate the visible branching fraction, we must correct this number for the relative selection efficiency ϵ_{evt} of dilepton events compared to single lepton events derived in Sect. 6.1.3:

$$\begin{aligned} \mathcal{B}_{vis}(B \to Xe\nu) &= \frac{1}{\epsilon_{evt}} \frac{N_{b\to xe\nu}}{N_{tag}} \\ &= (8.60 \pm 0.172_{(stat)})\% \ . \end{aligned} \tag{7.1}$$

The systematic error will be determined in Sect. 7.3.

7.2 Fit to Theoretical Models

Using theoretical predictions, the measured electron spectrum is extrapolated to $p^* = 0$. The following models are applied to describe the spectra from the individual decay channels:

- The form factor based ISGW2 model [20] is used for the decays $B \to D\ l\nu$ and $B \to D^{**}\ l\nu$, where D^{**} represents four excited states of the D meson ($D_0^*, D_1, D_1^{'}$ and D_2^*). This model is also used to describe the electron spectrum of $B \to X_u e\nu$.
- The decay $B \to D^* e\nu$ is modeled by a parameterization of HQET derived form factors (Sect. 2.4.4).
- Non resonant decays $B \to D^{(*)}\pi e\nu$ are described by the Goity-Roberts model [34].

For each decay mode, we construct normalized functions $f_D(p)$, $f_{D^*}(p)$, $f_{D^{**}}(p)$, $f_{D^{(*)}\pi}(p)$ and $f_{b\to u}(p)$ describing the shapes of the respective electron momentum spectra. This is achieved using the EvtGen event generator [21], which incorporates the effects of final state radiation via the PHOTOS package [39] and also boosts the generated momenta into the $\Upsilon(4S)$ rest frame. Since the observed spectrum has been corrected for external bremsstrahlung, it can be compared to a linear combination of the generated shapes:

$$f(p) = a[b_0\ f_D(p) + b_1\ f_{D^*}(p) + b_2\ f_{D^{**}}(p) + (1 - b_1 - b_2 - b_3)\ f_{D^{(*)}\pi}(p) + b_3\ f_{b\to u}(p)] \tag{7.2}$$

with

$$b_0 = \frac{\mathcal{B}(B \to De\nu)}{\mathcal{B}(B \to Xe\nu)}\ \ b_1 = \frac{\mathcal{B}(B \to D^*e\nu)}{\mathcal{B}(B \to Xe\nu)}\ \ b_2 = \frac{\mathcal{B}(B \to D^{**}e\nu)}{\mathcal{B}(B \to Xe\nu)}\ \ b_3 = \frac{\mathcal{B}(B \to X_u e\nu)}{\mathcal{B}(B \to Xe\nu)}$$

Because the branching fractions for $B \to D^{**}e\nu$ and non resonant decays are poorly known, we determine b_2 from fitting $f(p)$ to the observed data points, with a as additional parameter. This is done several times with different values of b_0 and b_1 in order to study the impact of the uncertainties in $\mathcal{B}(B \to De\nu)$ and $\mathcal{B}(B \to D^*e\nu)$ on the result. In accordance with the latest LEP measurements [33] of $\mathcal{B}(B \to X_u e\nu)$, the parameter b_3 is fixed to 0.016. Table 7.2 shows the extrapolation factors $1/\epsilon_{mtm}$ with ϵ_{mtm} defined as

$$\epsilon_{mtm} = \frac{\int_{0.5}^{2.5} f(x)dx}{\int_0^{2.5} f(x)dx}$$

when varying b_0 and b_1 within 1 standard deviation of the current PDG values.

Figure 7.1 shows the fitted spectrum for $b_0 = 0.2$ and $b_1 = 0.47$, which shows a good agreement between data and theoretical prediction. From the fit results we conclude that:

Fixed			Fit results			
$\frac{\mathcal{B}(B\to De\nu)}{\mathcal{B}(B\to Xe\nu)}$	$\frac{\mathcal{B}(B\to D^*e\nu)}{\mathcal{B}(B\to Xe\nu)}$	$\frac{\mathcal{B}(B\to X_ue\nu)}{\mathcal{B}(B\to Xe\nu)}$	$\frac{\mathcal{B}(B\to D^{**}e\nu)}{\mathcal{B}(B\to Xe\nu)}$	$\frac{\mathcal{B}(B\to D^{(*)}\pi e\nu)}{\mathcal{B}(B\to Xe\nu)}$	χ^2	$1/\epsilon_{mtm}$
0.185	0.42	0.016	0.38 ($\pm$ 0.007)	0.00 ($\pm$ 0.007)	30.68	1.046
0.2	0.42	0.016	0.36 ($\pm$ 0.007)	0.00 ($\pm$ 0.007)	29.23	1.046
0.215	0.42	0.016	0.35 ($\pm$ 0.007)	0.00 ($\pm$ 0.007)	27.83	1.046
0.185	0.47	0.016	0.33 ($\pm$ 0.009)	0.00 ($\pm$ 0.009)	19.48	1.044
0.2	0.47	0.016	0.31 ($\pm$ 0.010)	0.00 ($\pm$ 0.010)	18.52	1.044
0.215	0.47	0.016	0.30 ($\pm$ 0.010)	0.00 ($\pm$ 0.010)	17.62	1.044
0.185	0.52	0.016	0.28 ($\pm$ 0.015)	0.00 ($\pm$ 0.015)	12.37	1.042
0.2	0.52	0.016	0.26 ($\pm$ 0.015)	0.00 ($\pm$ 0.015)	11.89	1.042
0.215	0.52	0.016	0.25 ($\pm$ 0.016)	0.00 ($\pm$ 0.016)	11.47	1.042

Table 7.2: Extrapolation factors for different values of $\frac{\mathcal{B}(B\to De\nu)}{\mathcal{B}(B\to Xe\nu)}$ and $\frac{\mathcal{B}(B\to D^*e\nu)}{\mathcal{B}(B\to Xe\nu)}$

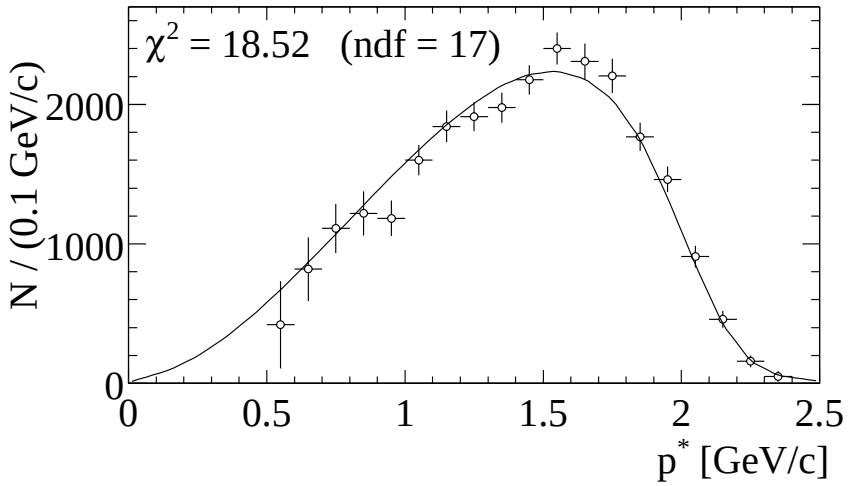

Figure 7.1: Fit of Eq. 7.2 with $b_0 = 0.2$ and $b_1 = 0.47$ to the measured spectrum after corrections for external bremsstrahlung have been applied

- The average extrapolation factor is 1.044 with a systematic error of 0.003, i.e. the estimated fraction of tracks with momenta below 0.5 GeV/c has got a relative systematic error of 7%.
- The fraction of non resonant semileptonic decays is quite small.

The latter item is in contradiction to the most recent measurement performed by the ALEPH collaboration, which determines $\mathcal{B}(B \to D^{(*)}\pi l\nu)$ to $(2.26 \pm 0.4)\%$ [40], leading to an approximate value of 0.2 for $\mathcal{B}(B \to D^{(*)}\pi l\nu)/\mathcal{B}(B \to Xl\nu))$. Setting the parameter b_2 in Eq. 7.2 to the corresponding value results in an extrapolation factor of 1.047. As final estimate, we use $1/\epsilon_{mtm} = 1.046$, which is the average between this and the previously derived value of 1.044. The difference between the extrapolation factors

derived with and without non resonant contributions is taken as additional systematic error. Finally, we repeat the same procedure using the ISGW2 prediction for the electron momentum spectrum from $B \to D^* l\nu$ decays. With a relative difference of less than 0.05%, the resulting extrapolation factors are very similar to the ones using the HQET parameterization. Table 7.3 summarizes all discussed uncertainties, which combine to a total relative systematic error of 0.4% on the extrapolation factor of 1.046, which corresponds to a 9% uncertainty on the estimated number of tracks with momenta below 0.5 GeV/c.

Source	Uncertainty (absolute)
$\mathcal{B}(B \to De\nu), \mathcal{B}(B \to D^* e\nu)$	0.003
Non resonant decays	0.003
Difference between ISGW2 and HQET model for $B \to D^* e\nu$	0.0005
Total	0.004

Table 7.3: Systematic uncertainties for extrapolation factor leading to the final estimate of $1/\epsilon_{mtm} = 1.046 \pm 0.004$

7.3 Total Branching Fraction

To compute the total from the visible branching fraction, three further corrections need to be applied:

- The geometrical acceptance of the angular cut, which is determined to $\epsilon_{geom} = 84.0\%$, using the EvtGen package to account for slightly non-flat distributions of polar and azimuthal angles in the $\Upsilon(4S)$ rest frame due to the movement of the B mesons and a small tilt between beam and detector axis.

- The fraction of prompt electrons with $p^* < 0.5$ GeV/c, which in the previous section has been determined to $1 - \epsilon_{mtm} = (4.6 \pm 0.4)\%$.

- The fraction of electrons which originally pass the momentum cut, but interact with the detector material via bremsstrahlung, resulting in a lower momentum which may fail this cut. This number depends on the amount of material, and is determined for two polar angles (90 degrees and 40 degrees) using the full detector simulation in order to quantify the material dependence. We find that this correction is $\epsilon_{brem} = (98.7 \pm 0.25)\%$.

Table 7.4 summarizes all corrections applied to the prompt and secondary electron spectra. With

$$\mathcal{B}(B \to Xe\nu) = \frac{1}{\epsilon_{geom}} \frac{1}{\epsilon_{mtm}} \frac{1}{\epsilon_{brem}} \mathcal{B}_{vis}(B \to Xe\nu) \tag{7.3}$$

we finally obtain

Quantity / Correction	x	$(\Delta x/x)_{(stat)}(\%)$	$(\Delta x/x)_{(sys)}$ (%)
$1/N_{tag}$	1/304051	0.3	0.64
ϵ_{evt}	0.98	0.15	0.5
ϵ_{geom}	0.84		
ϵ_{doca}	0.992	<0.05	0.3
ϵ_{trk}	(0.965)	<0.05	0.7
ϵ_{mtm}	0.956	<0.05	0.37
ϵ_{brem}	0.987	<0.05	0.25

Table 7.4: Multiplicative factors; $\Delta\epsilon_{doca}$ and $\Delta\epsilon_{trk}$ are added linearly.

$$\begin{aligned} \mathcal{B}(B \to Xe\nu) =& (10.85 \pm 0.22_{(stat)} \pm 0.34_{(sys)})\% \\ & (\Delta\mathcal{B}/\mathcal{B})_{(stat)} = 2.0\% \\ & (\Delta\mathcal{B}/\mathcal{B})_{(sys)} = 3.1\% \end{aligned} \tag{7.4}$$

The systematic error has been obtained by varying the background and multiplicative corrections within one standard deviation and adding the resulting deviations of $\mathcal{B}(B \to Xe\nu)$ in quadrature. Table 7.5 gives an overview of the individual contributions. The systematic error on the visible branching fraction is determined in the same way, leading to

$$\mathcal{B}_{vis}(B \to Xe\nu) = (8.60 \pm 0.17_{(stat)} \pm 0.26_{(sys)})\% \ .$$

Source	$\Delta x/x$ (%)	$\Delta\mathcal{B}(B \to Xe\nu)$ (%)	$\Delta\mathcal{B}_{vis}(B \to Xe\nu)$ (%)
Continuum Subtraction	0.5	0.008	0.007
$\gamma \to e^+e^-$	13	0.061	0.048
$\pi^0 \to \gamma e^+e^-$	19	0.030	0.024
Faked Electrons	15	0.042	0.033
Electron Efficiency	1.3	0.152	0.120
e from same B	5.0	0.034	0.027
e from τ	10	0.057	0.045
e from $D\overline{D}K$	32	0.144	0.114
e from D_s	45	0.173	0.137
e from J/ψ	6.0	0.003	0.003
e from $\psi^{'}$	20	0.001	0.001
e in mistagged events	20	0.067	0.053
$\chi = f_0\chi_0$	6.6	0.045	0.036
Tracking Efficiency	1.00	0.109	0.086
N_{tag}	0.64	0.069	0.055
$\epsilon_{dilep}/\epsilon_{single}$	0.50	0.054	0.043
ϵ_{mtm} (extrapolation to p=0)	0.50	0.054	
ϵ_{brem} (bremsstrahlung)	0.25	0.027	
Total		0.341	0.264

Table 7.5: Summary of systematic errors.

7.4 Extraction of $|V_{cb}|$

As shown in Sect. 2.3.2, the result on $\mathcal{B}(B \to Xe\nu)$ can be used for extracting $|V_{cb}|$ in the following way:

$$|V_{cb}| = \xi_{th} \sqrt{\frac{\mathcal{B}(B \to Xl\nu) - \mathcal{B}(B \to X_u l\nu)}{0.105} \frac{1.6\,\mathrm{ps}}{\tau_B}} \,, \tag{7.5}$$

with ξ_{th} as given in Eq. 2.9:

$$\xi_{th} = 0.0400\ \eta_{QED}\ (1 \pm 0.030 \pm 0.024 \pm 0.025 \pm 0.012) \,,$$

where $\eta_{QED} = 1.007$. As an estimate for $\mathcal{B}(B \to X_u\, l\nu)$, we use the current PDG value of $(1.67 \pm 0.55) \times 10^{-3}$ [33], and $\tau_B = 0.5\ (\tau_{B^+} + \tau_{B^0}) = (1.604 \pm 0.024)\,\mathrm{ps}$ as average between current PDG value and *BABAR* measurement [41].

Inserting these values into Eq. 7.5 and adding the errors in quadrature yields

$$|V_{cb}| = 0.0406 \pm 0.0009 \pm 0.0019 \,,$$

where the first error is given by the quadratic sum of statistical and systematic error of this measurement of $\mathcal{B}(B \to Xe\nu)$ and the second error originates from the theoretical uncertainties of ξ_{th}. A decomposition of these errors is shown in Table 7.6.

Source	$\Delta\|V_{cb}\|/10^{-2}$	$\Delta\|V_{cb}\|/\|V_{cb}\|[\%]$
$\Delta\mathcal{B}(B \to Xl\nu)_{stat}$	0.04	1.0
$\Delta\mathcal{B}(B \to Xl\nu)_{sys}$	0.07	1.7
$\Delta\mathcal{B}(B \to X_u l\nu)$	0.01	0.3
$\Delta\tau_B$	0.03	0.7
Perturb. corrections	0.12	3.0
$\Delta(m_b - m_c)$	0.10	2.4
Δm_b	0.10	2.5
$\mathcal{O}((1/m_b)^3)$ corrections	0.05	1.2
Total experimental error	0.09	2.1
Total theoretical error	0.19	4.7
Total	0.21	5.2

Table 7.6: Decomposition of $\Delta|V_{cb}|$.

Chapter 8

Summary

We developed an algorithm for electron identification which allows for several selection criteria. It has been successfully implemented into the *BABAR* software framework and is available for the whole *BABAR* collaboration. Determined from measurements based on data, the electron selection efficiency is $> 90\%$ for laboratory momenta above 0.5 GeV/c, while the per-track misidentification probability for pions is less than 0.05%. The average systematic error in the efficiency has been estimated to be $\approx 1.8\%$ when applied to spectra dominated by secondary electrons, and $\approx 1.2\%$ for spectra containing mostly high momentum tracks.

Using this algorithm, we selected dilepton events in order to determine $\mathcal{B}(B \to Xe\nu)$. The result is

$$\mathcal{B}(B \to Xe\nu) = (10.85 \pm 0.22_{(stat)} \pm 0.34_{(sys)})\%$$

where the systematic error is dominated by uncertainties in the electron identification efficiency and branching fractions of $c\bar{c}s$ processes. The first contribution is expected to be lowered by further detector studies, and in the near future analyses within the *BABAR* collaboration will also measure branching fractions for various decay channels involving $c\bar{c}s$ processes and therefore reduce our dominating systematic error.

Our value of $\mathcal{B}(B \to Xe\nu)$ is larger than older measurements on the $\Upsilon(4S)$ resonance, but still below most LEP measurements (Table 1.1). Another recent measurement performed by the BELLE collaboration yields the comparable result $\mathcal{B}(B \to Xe\nu) = (10.86 \pm 0.14_{(stat)} \pm 0.47_{(sys)})\%$ [43].

Comparing the statistical and systematic errors of our result with other measurements of $\mathcal{B}(B \to Xe\nu)$ (Table 8.1) shows that our statistical error is relatively large. Performing the analysis on the dataset available by now (i.e. the end of November 2001) could reduce this error by a factor of 2, and we expect it to become almost negligible as time goes on. Looking at the systematic errors, we find that our measurement is among the most precise ones, although it should be stressed that LEP measurements of $\mathcal{B}(B \to Xl\nu)$ using both electrons and muons achieve a comparable systematic error.

Finally, we determine $|V_{cb}|$ from the measured semileptonic branching fraction to be

$$|V_{cb}| = 0.0406 \pm 0.0009 \pm 0.0019 \ ,$$

where the errors represent experimental (statistical and systematic) and theoretical uncertainties, respectively.

Experiment	Year	$\mathcal{B}(B \to Xe\nu)[\%]$
CUSB [1]	1991	$10.0 \pm 0.4 \pm 0.3$
ARGUS [2]	1993	$9.7 \pm 0.5 \pm 0.4$
CLEO2 [3]	1996	$10.49 \pm 0.17 \pm 0.43$
OPAL (Z-resonance) [7]	2000	$10.78 \pm 0.08^{+0.50}_{-.46}$
L3 (Z-resonance) [5]	1996	$10.89 \pm 0.2 \pm 0.51$
DELPHI (Z-resonance) [42]	1993	$10.7 \pm 1.5 \pm 0.7$
BELLE [43]	2001	$10.86 \pm 0.14 \pm 0.47$
BABAR (this measurement)	**2001**	$\mathbf{10.85 \pm 0.22 \pm 0.34}$

Table 8.1: Measurements of the inclusive semileptonic branching fraction using electrons only. In contrast to Table 1.1, the values obtained on the Z resonance are not rescaled, but are averaged over B_u,B_d,B_s and b - baryon decays. Since the most recent LEP-measurements shown in Table 1.1 do not state separate results for electrons, they are not listed in this table.

Bibliography

[1] C. Yanagisawa *et al.* [CUSB Collaboration], B semileptonic decays at the $\Upsilon(4S)$ and the $\Upsilon(5S)$, Phys. Rev. Lett. **66** (1991) 2436.

[2] H. Albrecht *et al.* [ARGUS Collaboration], A Model independent determination of the inclusive semileptonic decay fraction of B mesons, Phys. Lett. B **318** (1993) 397.

[3] B. Barish *et al.* [CLEO Collaboration], Measurement of the B Semileptonic Branching Fraction with Lepton Tags, Phys. Rev. Lett. **76** (1996) 1570.

[4] P. Abreu *et al.* [DELPHI Collaboration], Measurement of $\Gamma_{b\bar{b}}/\Gamma_{had}$ using impact parameter measurements and lepton identification, Z. Phys. C **66** (1995) 379.

[5] M. Acciari *et al.* [L3 Collaboration], Measurement of the branching ratios $b \to e\,\nu\,X$, $\mu\,\nu\,X$, $\tau\,\nu\,X$ and $\nu\,X$, Z. Phys. C **71** (1996) 379.

[6] M. Acciari *et al.* [L3 Collaboration], Measurement of $R_{\rm b}$ and Br(b $\to \ell\nu$X) at LEP using double-tag methods, Eur. Phys. J. C **13** (2000) 47.

[7] G. Abbiendi *et al.* [OPAL Collaboration], Measurements of inclusive semileptonic branching fractions of b hadrons in Z^0 decays, Eur. Phys. J. C **13** (2000) 225.

[8] The ALEPH Collaboration, Inclusive semileptonic branching ratios of b hadrons produced in Z decays, CERN-EP/2001-57 (submitted to European Physics Journal C).

[9] B. Aubert *et al.* [*BABAR* Collaboration], Observation of CP violation in the B^0 meson system, Phys. Rev. Lett. **87**, 091801 (2001).

[10] K. Abe *et al.* [Belle Collaboration], Observation of large CP violation in the neutral B meson system, Phys. Rev. Lett. **87**, 091802 (2001).

[11] J.L. Cortez, X.Y.Pham and A.Tounsi, Mass effects in weak decays of heavy particles, Phys. Rev. **D25** (1982) 188.

[12] J. Richman and P. Burchat, Leptonic and Semileptonic Decays of Charm and Bottom Hadrons, Stanford-HEP-95-01 .

[13] G. Altarelli and S. Petrarca, Inclusive beauty decays and the spectator model, Phys. Lett. **B 261** (1991) 303.

[14] E. Bagan, P. Ball, V.M. Braun, and P.Gosdzinsky, Theoretical update of the semileptonic branching ratio of B mesons, Phys. Lett. **B 342** (1995) 362.

[15] M. Shifman, N. Uraltsev and A.Vainstain, Operator product expansion sum rules for heavy flavor transitions and the determination of $|V_{cb}|$, Phys. Rev. **D51** (1995) 2217.

[16] P.F. Harrison and H.R. Quinn (Editors), The *BABAR* Physics Book, SLAC-R-504 (1998).

[17] I. Bigi, M. Shifman and N. Uraltsev, Ann. Rev.Nucl.Part.Sci. **47** (1997) 591.

[18] M. Altarelli *et al.*, Nucl. Phys. B **208** (1982) 365.

[19] D. Scora and N. Wise, Semileptonic B and D decays in the quark model, Phys. Rev. D **9** (1989) 799.

[20] D. Scora and N. Wise, Semileptonic meson decay in the quark model: An update, Phys. Rev. D **52** (1995) 2783.

[21] A. Ryd *et al.*, EvtGen, A Monte Carlo generator for B-physics, available at the *BABAR* software repository.

[22] J.E. Dubosq. *et al.* [CLEO Collaboration], Measurement of Form Factors for $\overline{B}^0 \to D^{*+} l^- \bar{\nu}$, Phys. Rev. Lett. **76** (1996) 3898.

[23] V. Re *et al.,* The *BABAR* Silicon Vertex Tracker, preprint submitted to Elsevier Science.

[24] F. Martinez-Vidal *et al.,* The *BABAR* Vertexing, *BABAR* Analysis Document #102 (2001).

[25] B. Aubert *et al.* [*BABAR* Collaboration], The *BABAR* Detector, submitted to Nucl. Instrum. and Methods (2001).

[26] A. Höcker *et al.*, A Maximum Likelihood Method For DIRC Particle Identification, *BABAR* Analysis Document #23 (2000).

[27] Giampiero Mancinelli : Control Samples of Pions and Kaons and Kaon ID (September 1999).
http://www.slac.stanford.edu/BFROOT/www/Physics/Tools/Pid/Meetings/Padova/mancinelli.ps

[28] M.Carroll, F.Galeazzi, M.Serra, C.Touramanis: Pion Sample from tau tau 3-1 events (September 1999).
http://www.slac.stanford.edu/BFROOT/www/Physics/Tools/Pid/Control/PiK/taus/taupid.html

[29] G. Hamel de Monchenault, private communication; see also
http://online04.lbl.gov/ gautier/reco/reco.html#Ring Dictionary (June 16, 1998)

[30] A. Höcker, private communication.

[31] E. Varnes, Measurement of the GoodTrackLoose efficiency using SVT tracks, *BABAR* Analysis Document # 150 (2001).

[32] H. Albrecht *et al.* [ARGUS Collaboration], Inclusive production of charged pions, kaons and protons in $\Upsilon(4S)$ decays, Z. Phys. C **58** (1993) 191.

[33] The European Physics Journal C, Volume 15, Number 1-4 (2000).

[34] J.L. Goity and W. Roberts, Soft pion emission in semileptonic B-meson decays, Phys. Rev. D **51** (1995) 3459

[35] European Organization for Nuclear Research, Combined results on b-hadron production rates and decay properties, CERN-EP/2001-50 .

[36] R. Barate *et al.* [ALEPH Collaboration], Observation of doubly-charmed B decays at LEP, Eur. Phys. J. C **4** (1998) 387.

[37] The *BABAR* PID group (August 2001).
http://www.slac.stanford.edu/BFROOT/www/Physics/Tools/BetaTools/MicroKilling.html

[38] U. Langenegger, Cut-based Electron Identification, *BABAR* Analysis Document #90 (2000).

[39] E. Richter-Was, QED bremsstrahlung in semileptonic B and leptonic τ decays, Phys. Lett. B **303** (1993) 163.

[40] D. Buskulic *et al.* [ALEPH Collaboration], Production of orbitally excited charm mesons in semileptonic B decays, Z. Phys. C **73** (1997) 601.

[41] J.Stark, Measurements of the charged and neutral B meson lifetimes using fully reconstructed B decays, *BABAR* Analysis Document #144 (2001).

[42] P. Abreu *et al.* [DELPHI Collaboration], A study of B^0- $\overline{B}^0$ mixing using semileptonic decays of B hadrons from Z^0, Phys.Lett. B **301** (1993) 145.

[43] H.Kim *et al.* [BELLE Collaboration], Presentation on 9th international symposium on heavy flavor physics (2001).

Acknowledgements

I would like to thank my thesis advisor Prof. Dr. K.R. Schubert from the *Institut für Kern- und Teilchenphysik*(IKTP) of the Technical University of Dresden for giving me the opportunity to work on this thesis within an international collaboration. I am grateful for the constant support and the opportunities to stay at the Stanford Linear Accelerator Center for extended periods of time.

I would also like to thank Prof. Dr. B. Spaan for the constant support and helpful discussions on many physics related issues. I am grateful to Priv. Doz. Dr. R.Waldi for introducing me into the world of high energy physics and for patiently answering all my questions connected to physics and statistics.

I am especially grateful to Vera Lüth for the excellent conditions provided by the *BABAR* analysis working group on inclusive semileptonic decays, and for the many helpful and interesting discussions which provided many new ideas and insights for this analysis. I would also like to thank Helmut Marsiske for introducing me into *BABAR* during my first months at SLAC. For both electron identification and physics analysis, Urs Langenegger was always available for questions and discussions, for which I am very thankful. I also gratefully acknowledge Aaron Roodman for the excellent organization of the *BABAR* working group on particle identification. I would like to thank in particular Giampiero Mancinelli, who contributed to my understanding of selecting pure kaon and pion samples.

Further, I would like to thank Rainer Schwierz for his excellent work at the IKTP, resulting in a 100% stable computing infrastructure and therefore supplying the best working conditions. For the support in problems involving technical or software questions, I would like to thank Jens Brose, Ralph Müller–Pfefferkorn, Martin Kocian and Leif Wilden. The same applies to Tilmann Colberg, Martin Dickopp and Rolf Dubitzky, who together with Bruno Serfass read through this work and provided many improvements, for which I am particularly grateful. I also would like to thank all other colleagues at the IKTP for providing a relaxed working atmosphere.

During my visits to SLAC, which altogether lasted more than a year, I was always welcome to stay at the house of Colin and Carol Tam. I gratefully acknowledge their hospitality.

I also would like to thank my parents for their support, especially during my undergraduate studies, which enabled me to start this thesis in the first place.

Finally, I would like to thank the *Bundesministerium für Bildung und Forchung* (BMBF) for the financial support provided for this work.

HSSS AdminTools (c) 2001, last visited: Fri Apr 26 11:51:04 GMT+02:00 2002